ADVANCED ENERGY MATERIALS
www.advenergymat.de

Photo/Electrochemical Applications of Metal Sulfide/TiO_2 Heterostructures

Lingxia Zheng, Feng Teng, Xiaoying Ye, Huajun Zheng, and Xiaosheng Fang**

Developing efficient and affordable catalysts is of great significance for energy and environmental sustainability. Heterostructure photocatalysts exhibit a better performance than either of the parent phases as it changes the band bending at the interfaces and provides a driving force for carrier separation, thus mitigating the effects of carrier recombination and back-reaction. Herein, the photo/electrochemical applications of a variety of metal sulfides (MS_x) (MoS_2, CdS, CuS, PbS, SnS_2, ZnS, Ag_2S, Bi_2S_3, and In_2S_3)/TiO_2 heterojunctions are summarized, including organic degradation, water splitting, and CO_2 reduction conversion. First, a general introduction on each MS_x material (especially bandgap structures) will be given. Then the photo/electrochemical applications based on MS_x/TiO_2 heterostructures are reviewed from the perspective of light harvesting ability, charge carrier separation and transportation, and surface chemical reactions. Special focus is given to CdS/TiO_2 and PbS/TiO_2-based quantum dot sensitized solar cells. Ternary composites by taking advantages of positive synergetic effects are also well summarized. Finally, conclusions are made regarding approaches for structure design, and the authors' perspective on future architectural design and electrode construction is given. This work will make up the gap for TiO_2 nanocomposites and shed light on the fabrication of more efficient MS_x-metal oxide junctions in photo/electrochemical applications.

1. Introduction

1.1. Scope of This Review

Sustainable development of human society has aroused serious environmental pollution problems and the depletion of fossil fuel resources. Thus, it is imperative to develop green and efficient technologies to control and reduce pollution growth, in combination with the exploration of renewable sources of clean energy. Solar energy is one of the most abundant green energy resources, which can be utilized by semiconductor materials to degrade toxic chemicals to environmentally friendly compounds, generate fuel (water splitting, reduce CO_2 into renewable hydrocarbon fuels), and convert sunlight to electricity (solar cells). Since a pioneering work on photoelectrochemical (PEC) water splitting on a TiO_2 electrode in 1972,[1] titanium dioxide (TiO_2) has been investigated in a large variety of environment, energy, and health-related applications owing to the commonly mentioned advantages including nontoxicity, abundant availability, good chemical/physical stability, ease of fabrication, and suitable potential for proton reduction.[2] As a versatile material, TiO_2 has been regarded as a well-known photocatalyst to initiate or accelerate specific reduction and oxidation processes on the surface upon irradiation. Potential applications are mainly focused on three aspects: (1) photocatalytic degradation of organic pollutants, (2) water splitting for hydrogen or oxygen production, and (3) photocatalytic CO_2 reduction. The key factors determining the PEC performances involve light absorption, photogenerated charge separation and transportation, and carrier-induced surface reactions. However, single and pristine TiO_2 material hardly achieve harmonious. With a wide bandgap (anatase of ≈3.2 eV, rutile of ≈3.0 eV), TiO_2 can solely absorb UV light, accounting for less than 5% over the full solar resource, which is the biggest drawback of TiO_2 material. The single phase and nanoscale features also induce fast recombination of the photogenerated electron–hole (e–h) pairs in TiO_2, thus leading to a low quantum efficiency and poor PEC activity.

In recent years, there are several published reviews concerning on TiO_2-based composites applied in PEC fields as constructing "junctions with built-in electric fields or chemical potential differences" is one of the most effective strategies.

Dr. L. X. Zheng, X. Y. Ye, Prof. H. J. Zheng
State Key Laboratory Breeding Base of Green Chemistry Synthesis Technology
Zhejiang University of Technology
Hangzhou 310032, P. R. China
E-mail: zhenghj@zjut.edu.cn

Dr. L. X. Zheng, X. Y. Ye, Prof. H. J. Zheng
Department of Applied Chemistry
Zhejiang University of Technology
Hangzhou 310032, P. R. China

Dr. L. X. Zheng, Dr. F. Teng, Prof. X. S. Fang
Department of Materials Science
Fudan University
Shanghai 200433, P. R. China
E-mail: xshfang@fudan.edu.cn

Dr. F. Teng
School of Physics
Northwest University
Xi'an 710127, P. R. China

The ORCID identification number(s) for the author(s) of this article can be found under https://doi.org/10.1002/aenm.201902355.

DOI: 10.1002/aenm.201902355

 © 2019 WILEY-VCH Verlag GmbH & Co. KGaA, Weinheim

However, they mainly focus on the combination with metals/nonmetal elements, oxides, and carbon-based materials (graphene, carbon nanotubes),[3] metal sulfide (MS_x) is rarely well-introduced except that Ma et al.[2e] reviewed the fundamental mechanism and the emerging strategies for activity improvement of TiO_2-based nanomaterials with emphasis on CdS, Dahl et al.[3b] reviewed the composite TiO_2 nanomaterials and emphasized on CdS/CdSe-TiO_2 and PbS/PbSe-TiO_2, Wang et al.[3c] reviewed the advanced progress of TiO_2 nanotube array-based composites with emphasis on CdS. In particular, transition-metal dichalcogenides (TMDs) have attached many attentions recently due to their layered structures and some related unique photoelectronic properties, especially narrow bandgaps, high carrier mobility, and large surface areas, which are excellent candidates to enhance the PEC performance of TiO_2 composites. In this regard, we propose this review relying on metal sulfide/TiO_2 (MS_x/TiO_2) heterostructures based photoelectrodes in the applications of photodegradation, water splitting for H_2 production, and photocatalytic CO_2 reduction. The MS_x materials discussed here are MoS_2, CdS, CuS, PbS, Sn_2S, ZnS, Ag_2S, Bi_2S_3, and In_2S_3, and their bandgap positions are displayed in **Scheme 1** for reference, which will be varied upon different fabrication strategies and testing conditions. Moreover, ternary composites by taking advantages of positive synergetic effects between MS_x and a secondary material are well summarized to achieve a further improvement, including strategies of metal decoration, nanocarbon material modification, a secondary material cosensitization, which further help suppress charge recombination, facilitate interfacial charge transfer, and offer extra active sites. In addition, special focus has been given to the quantum dot sensitized solar cells (QDSCs) based on CdS/TiO_2 and PbS/TiO_2 electrodes. At last, we make conclusions from the structure steering point of view and provide our outlook on future material design and electrode construction. This work will make up the gap of TiO_2-based composites in photocatalysts and solar energy conversion.

1.2. General Mechanism of PEC Application

PEC process initiates from light absorption, so the first restriction originates from the number and energy of photons absorbed by the materials. First, when the photons are absorbed, electrons in the valance band (VB) of a semiconductor would excite into conduction band (CB), leaving holes in the VB. The photogeneration of e–h pairs is the fundamental process. The amount of e–h pairs is determined by the amount of absorbed photons. Then, the photogenerated e–h would recombine immediately in most direct bandgap semiconductors, and release the corresponding energy, which is undesirable for the PEC reaction. As a result, the second dominant process is the separation and transfer of photogenerated e–h. When the electron and hole arrive at the surface of a semiconductor, they would combine and react with some special molecules or groups, such as hydroxyl, oxygen molecule, carbon dioxide, heavy metal ions, etc., which would be divided into different application fields, including degradation of organics, hydrogen generation, CO_2 reduction, heavy metal ion reduction, and so on. The effective use of these separated e–h to initiate or accelerate specific reduction and oxidation processes on the surface is another important process.

Lingxia Zheng is currently an associate professor at College of Chemical Engineering, Zhejiang University of Technology (ZJUT). She received her Ph.D. degree from Department of Physics and Materials Science, City University of Hong Kong in 2013. Then she worked as a postdoctoral fellow in Fudan University for 2.5 years before joining in ZJUT. Her research interests focus on the design, development, and exploration of functional nanomaterials for optoelectronic devices, photoelectrochemical application, and electrochemical energy storage application.

Huajun Zheng is professor at College of Chemical Engineering, Zhejiang University of Technology (ZJUT), China. He received his Ph.D. degree from ZJUT in 2005. As senior visiting scholar, he worked at ARC Centre of Excellence for Functional Nanomaterials, The University of Queensland (Australia), for one year in 2008. Zheng's research interests include the design and development of functional nanomaterials for renewable energy conversion and storage applications including electrocatalysis, photocatalysis, and electrochemical energy storage devices.

Xiaosheng Fang is currently a professor in the Department of Materials Science, Fudan University, China. He received his Ph.D. degree from the Institute of Solid State Physics (ISSP), Chinese Academy of Sciences in 2006. After then, he was a JSPS postdoctoral fellow at the National Institute for Materials Science, Japan, as well as a research scientist at the International Center for Young Scientists (ICYS). He was a visiting scholar at MIT and Harvard University. His current research involves photodetectors and materials for energy harvesting and conversion.

© 2019 WILEY-VCH Verlag GmbH & Co. KGaA, Weinheim

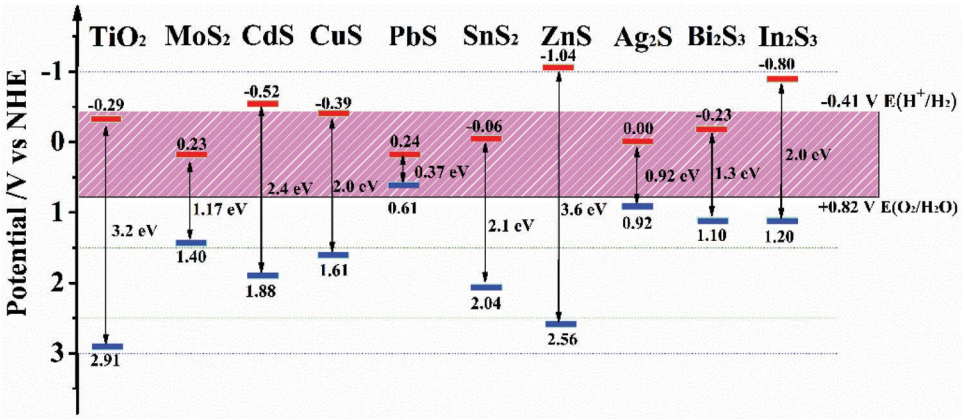

Scheme 1. Bandgap values and band edge positions of TiO_2 and MS_x discussed in the study. All the energy levels are referenced to normal hydrogen electrode (NHE) scale. Noted that the uncertainty in the edge positions can be amount to a few tenths of eV for MS_x considering the preparation strategies and testing conditions.

In order to enhance the PEC performance (photodegradation, water splitting for H_2 production, and CO_2 reduction) of MS_x/TiO_2 heterostructures, three aspects could be considered:

i) *Light harvesting ability*: With a narrow bandgap, MS_x (except ZnS in this review) can facilitate light absorbance across the visible and even infrared ranges, thus covering a significant range of low energy bandwidth in the solar spectrum, improving the overall efficiency of the MS_x/TiO_2 heterostructures.

ii) *Charge separation and transportation*: Surface sensitization with MS_x is rather appealing, as the presence of heterojunction changes the band bending at the interface and provides a driving force for carrier separation in order to mitigate the effects of carrier recombination and back-reaction, which in turn increases photo/electrochemical reactivity.[4] As an important II–VI semiconductor with a wide bandgap, ZnS can also be associated with TiO_2 to increase the photoactivity because of its high potentials of conduction band e^- and valence band h^+,[5] which can effectively separate the interfacial carriers, preventing carrier recombination.

iii) *Carrier-induced surface chemical reactions*: Thanks to a favorable band offset of MS_x/TiO_2 heterostructure, photogenerated electrons would migrate to TiO_2, while holes are trapped in MS_x. Redox reactions are free to occur at the separate surfaces since the possibility of charge recombination has been diminished. A large specific surface area and abundant active reaction sites are critical to afford a full contact with electrolyte and improve reaction efficiency in PEC processes. Ultrafine/few-layered MS_x nanosheets, especially MoS_2, SnS_2, Bi_2S_3, and In_2S_3 that endow intrinsic layered structures, are favored to provide more exposed active edge sites for surface chemical reactions.

Thus, considering that metal sulfides display unique properties and advantages, MS_x/TiO_2 composites exhibit great potential in the PEC applications. Detailed mechanism will be introduced case by case for each metal sulfide.

1.3. Basic Principle of QDSCs and Properties of MS_x QDs

QDSCs have become one of the most popular research topics for the next generation of solar cells, because quantum dots (QDs) offer impressive ability to harvest sunlight, advantageous features of photostability, high molar extinction coefficients, size-dependent optical properties, ease of fabrication, and low cost. Compared with organic dye molecules and lead halide perovskites, QDs are more stable and controllable in the practical applications of solar cells. Derived from dye-sensitized solar cell (DSC), QDSC employs QDs as the light harvesting material to generate charge carriers instead of organic dye molecules.[6] The structure of a QDSC generally composes of a QD-sensitized photoanode, an electrolyte, and a counter electrode (CE). Upon light illumination, the QDs absorb solar energy and generate e–h pairs. Then, the excited electrons in the CB of the QDs are quickly injected into the CB of a metal oxide (generally TiO_2) electron-transporting/acceptor material (ETM) under the driving force arising from the CB energetic difference between the QDs and metal oxide, thereby achieving a charge separation process. The electrons transfer through the metal oxide film to the transparent conductive oxide substrate and then to the CE through an external circuit. Meanwhile, the oxidized QDs are regenerated by reduced species of the redox couple in the electrolyte, while the oxidized species of the redox couple are reduced by the electrons from the external circuit under the catalysis of CE.[7]

Two fundamental preparation methods are used for QD sensitizers: in situ and ex situ fabrication.[7b] The former includes chemical bath deposition (CBD) and successive ionic layer adsorption and reaction (SILAR). The latter involves the attachment of presynthesized colloidal QDs either by using molecular links with functional groups or by direct adsorption without linkers. The in situ one usually performs better than the ex situ technique when assembling QDSC and both are applicable in large-scale production. However, the precise control of the particle size distribution becomes a big challenge.

TiO_2-based electrodes sensitization with CdS QDs or PbS QDs are promising for enhanced power conversion efficiency

© 2019 WILEY-VCH Verlag GmbH & Co. KGaA, Weinheim

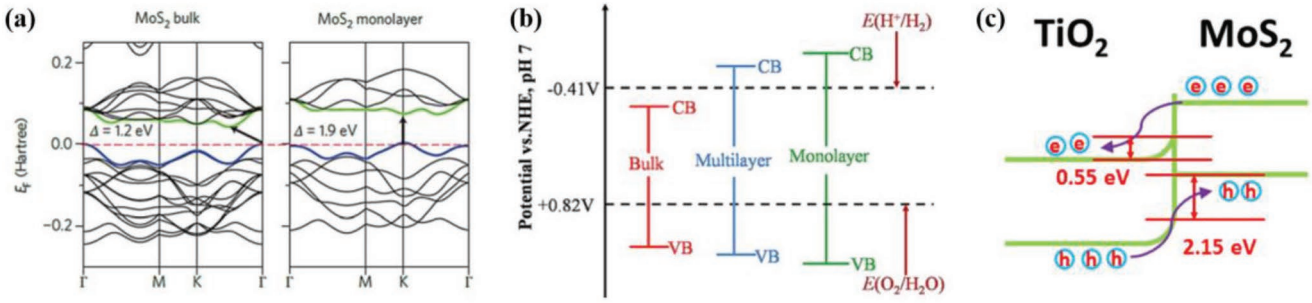

Figure 1. a) Band structures calculated from first-principles density functional theory (DFT) for bulk and monolayer MoS_2. Reproduced with permission.[10] Copyright 2012, Nature Publishing Group. b) Energy diagrams of conduction band and valence band edge potentials in different sized MoS_2. Reproduced with permission.[6] Copyright 2015, Wiley-VCH. c) Illustration of band bending and charge separation mechanism for 2D MoS_2/TiO_2 hetero-thin film. Reproduced with permission.[13d] Copyright 2015, AIP Publishing.

(PCE) in QDSCs owing to the size-dependent optical absorbance (driven mainly by quantization effects), improved light-to-electrical energy conversion (boosted by multiple-exciton generation), and enhanced interfacial carrier separation. As the core component, ideal QD sensitizers endow the following characteristics: (1) a narrow bandgap to absorb sunlight over the solar spectrum and a high absorption coefficient to harvest more light; (2) hot carrier injection from higher excited state to the CB of TiO_2 through light irradiation; (3) good stability toward light, heat, and electrolyte; (4) simple preparation and low toxicity.[7a] The key issue lies in the difficulty to balance the light-harvesting efficiency and electron-injection efficiency. For CdS QDs, their CB edge is suitable for effective charge separation, however the light harvesting range is narrow due to a relatively wide bandgap. On the contrary, PbS QDs possess a narrower bandgap, but their CB edge is lower and thus their electron-injection efficiency is compromised. The detailed QDSC performance regarding these two QDs will be discussed case by case.

2. MoS_2/TiO_2 Heterostructures

2.1. Basic Properties of MoS_2

MoS_2 is a recently well-reported member of TMDs due to its graphite analogous structure and corresponding graphene-like properties, inherently beneficial for catalysis and water splitting applications.[8] The bulk MoS_2 comprises layers of S-Mo-S coupled with weak van der Waals interactions. Each layer is built up of an intermediate plane of Mo atoms sandwiched between two S atoms with strong covalent bonds. The highly anisotropic structure allows top-down exfoliation to obtain ultrathin flakes by mechanical/chemical processes, and bottom-up synthesis of thin films, nanoplates, nanoribbons, etc.[9]

The interest in MoS_2 for photo/electrochemical applications stems from its narrow bandgap that closely matches the solar spectrum and from its stability against photocorrosion.[10] When its dimension being reduced to atomically thin layers, monolayer/few-layer MoS_2 possesses a direct optical bandgap of ≈1.9 eV,[11] which crosses over to an indirect one of ≈1.2 eV for bulk counterpart (**Figure 1**a).[12] Unfortunately, the CB energy level of bulk MoS_2 is less negative than that of TiO_2, thus electrons would not transfer from MoS_2 to TiO_2. While few-layered MoS_2 exhibits quantum confinement effects, which leads to an increased bandgap and a change in the redox potentials. It endows a more positive CB edge potential than TiO_2 but more negative than H^+/H_2 redox couple, indicating the cocatalyst role in the enhanced photocatalytic H_2 production of TiO_2. Interestingly, the CB edge potential of monolayer MoS_2 is more negative than that of TiO_2, making easily electron transfer from MoS_2 to TiO_2 (Figure 1b).[13] Tao et al.[13d] presented clear experimental evidence for type II band alignment and upward band bending (0.55 eV) at the interface of monolayer MoS_2/TiO_2 composites. The unique interface band positions introduced a strong built-in electric field for efficient e–h separation (Figure 1c). Nevertheless, in semiconductor terminology, its bandgap value is different from the optical one which depends on the dielectric environment and at least 0.3 eV larger than the optical bandgap.[14]

2.2. Photodegradation of Organic Pollutants

2.2.1. Band Engineering for Visible-Light Photodegradation

Extensive studies have been reported to realize visible light induced photodegradation based on MoS_2/TiO_2 heterostructures (**Table 1**). The role of MoS_2 was reported to be an effective photosensitizer in analogy to quantum dot sensitization, which led to enhanced degradation of organic molecules.[15] The UV–vis absorption spectra of pure TiO_2 nanostructures commonly revealed a significant absorption edge at wavelength shorter than 400 nm owing to the intrinsic bandgap absorption.[23] After forming a heterostructure with MoS_2, the absorption edge redshifted with enhanced absorption in visible light region (e.g., ≈450 nm) due to the chemical bonding between TiO_2 and MoS_2.[24]

In order to further enhance the visible-light-responsive photoactivity and take advantage of dual functional materials, a secondary narrow bandgap material, such as CdS (≈2.4 eV),[25] g-C_3N_4 (≈2.7–2.8 eV),[26] or Ag_3PO_4 (≈2.45 eV),[27] was used to form a ternary composite with MoS_2/TiO_2. These ternary photocatalysts exhibited enlarged spectral response to visible light region and improved photocatalytic performance due to the synergetic effect of two narrow bandgap materials, which further facilitated the separation of e–h pairs.

© 2019 WILEY-VCH Verlag GmbH & Co. KGaA, Weinheim

Table 1. Summary of MoS_2/TiO_2-based heterostructures applied in photodegradation of organic pollutants.

Photocatalysts	Loading methods	Light source	Surface area [$m^2 g^{-1}$]	Catalyst amount	Pollutant	Degradation %	Ref.
MoS_2 nanosheets@TiO_2 nanotube array	Hydrothermal	230 W Hg lamp, $\lambda = 365$ nm	–	≈1 mg; 1.766 cm^2	RhB (5 mL, 10 mg L^{-1})	85.3%, 120 min	[33]
MoS_2 nanodots/TiO_2 NPs	Liquid exfoliation	High pressure Hg lamp	–	20 mg	RhB or MB (40 mL, 10 mg L^{-1})	100%, 20 min	[15c]
MoS_2 nanosheets/TiO_2 NPs	Liquid exfoliation	XG500 Xe lamp	–	50 mg	MB (250 mL, 20 mg L^{-1})	91.4%, 60 min	[16]
TiO_2 nanorods@MoS_2 nanosheets	Hydrothermal	20 W tungsten halogen lamp	–	0.01 g	MB (100 mL, 10 mg L^{-1})	90% within 100 min	[31]
MoS_2 nanoflowers@TiO_2 NPs			–			<90% within 100 min	
TiO_2 NPs/MoS_2 NPs	Solvothermal	Two Hg lamps	118	100 mg	MB (300 mL of 5 ppm)	65%, 120 min	[15b]
MoS_2 nanosheets/TiO_2 nanobelts	Hydrothermal	300 W mercury lamp with $\lambda_{max} = 365$ nm	72.2	20 mg	MO (20 mL, 20 mg L^{-1})	100%, 15 min	[4b]
MoS_2 nanocluster/TiO_2 NPs	Deposition-calcination	30 W daylight lamp	91.5	0.1 g	MO (150 mL, 20 mg L^{-1})	≈89%, 120 min	[17]
MoS_2 NPs/TiO_2 NPs	Hydrothermal	400 W Xe lamp	–	–	Phenol (40 mL, 20 ppm)	100%, 240 min	[18]
		125 W Hg lamp	–	–	Phenol (40 mL, 60 ppm)	100%, 70 min	
MoS_2 nanosheets/TiO_2 nanosheets	Hydrothermal	250 W Hg lamp	98	20 mg	MB (100 mL, 4×10^{-5} M)	≈90%, 60 min	[40]
MoS_2 nanosheets/TiO_2 nanodrums	Hydrothermal	250 W Hg lamp	84	20 mg	MB (100 mL, 4×10^{-5} M)	≈70%, 60 min	[19]
MoS_2 nanosheets/TiO_2 hollow spheres	Hydrothermal	300 W Xe lamp, $\lambda \geq 420$ nm		0.01 g	Phenol (60 mL, 10 mg L^{-1})	78%, 150 min	[20]
MoS_2 nanoflower/TiO_2 nanotube arrays	Hydrothermal	500 W Xe lamp, $\lambda > 420$ nm	–	10 mg	MB or levofloxacin (50 mL, 10 mg L^{-1})	100%; 150 min for MB; 180 min for levofloxacin	[21]
MoS_2 nanosheets/TiO_2 nanofibers	Hydrothermal	50 W Hg lamp, $\lambda = 313$ nm	37.37	0.01 g	RhB or MO (100 mL, 10 mg L^{-1})	98.2% for RhB; 97% for MO in 30 min	[22]
N-TiO_2 NPs/MoS_2 nanosheets	Hydrothermal	300 W Xe lamp, $\lambda > 400$ nm	–	50 mg	MB (50 mL, 10 mg L^{-1})	98.5%, 120 min	[29]
N-TiO_{2-x} nanospheres@MoS_2 nanosheets	Hydrothermal	300 W Xe lamp, $\lambda > 420$ nm	–	50 mg	MO (50 mL, 10 mg L^{-1})	91.8%, 120 min	[30]
MoS_2 NPs/CdS NPs/ TiO_2 NPs	Solvothermal	500 W Xe lamp, $\lambda > 420$ nm	–	7.5 mg	MB (15 mL, 5 mg L^{-1})	72%, 160 min	[25]
TiO_2 NPs/g-C_3N_4 nanosheets/ MoS_2 nanosheets	Ultrasonic exfoliation Solvothermal	XG500 Xe lamp	192.2	100 mg	MO (250 mL, 20 mg L^{-1})	>90%, 60 min	[26]
Ag_3PO_4 NPs/TiO_2 nanofibers@MoS_2 sheets	Hydrothermal	800 W Xe lamp		0.25 g	MO or MB (500 mL, 2.5 mg L^{-1})	>92%; 12 min for MO, 5 min for MB	[27]
MoS_2 nanosheets/P25/ graphene aerogel	Hydrothermal	300 W Hg lamp, $\lambda_{main} = 365$ nm	–	25 mg	MO (100 mL, 20 mg L^{-1})	100%, 15 min	[42]
TiO_2-RGO NPs/MoS_2 nanosheets	Hydrothermal	Sunlight irradiation	–	50 mg	MB (100 mL, 10 mg L^{-1})	100%, 100 min	[43]
MoS_2 QDs/TiO_2 NPs/ graphene	Hydrothermal	A solar simulator with 150 W Xe lamp	67.8	40 mg	RhB (80 mL, 10 mg L^{-1})	>80%, 80 min	[44]
TiO_2 nanobelts@MoS_2 nanosheets	Hydrothermal	300 W Xe lamp, $\lambda = 280$–700 nm	44.9	1 mg	RhB (10 mL, 15 mg L^{-1})	100%, 20 min	[15a]
TiO_2 nanobelts/MoS_2 NPs	Hydrothermal	500 W Xe lamp		70 mg	RhB (70 mL, 10 mg L^{-1})	100%, 90 min	[32c]
MoS_2 nanobelts/TiO_2 nanotube arrays	Photo-assisted electrodeposition	500 W Xe lamp, $\lambda \geq 410$ nm		–	MB (20 mg L^{-1}); Sulfadiazinmu (10 mg L^{-1})	>60% for MB, 64% for SD in 240 min	[24]

© 2019 WILEY-VCH Verlag GmbH & Co. KGaA, Weinheim

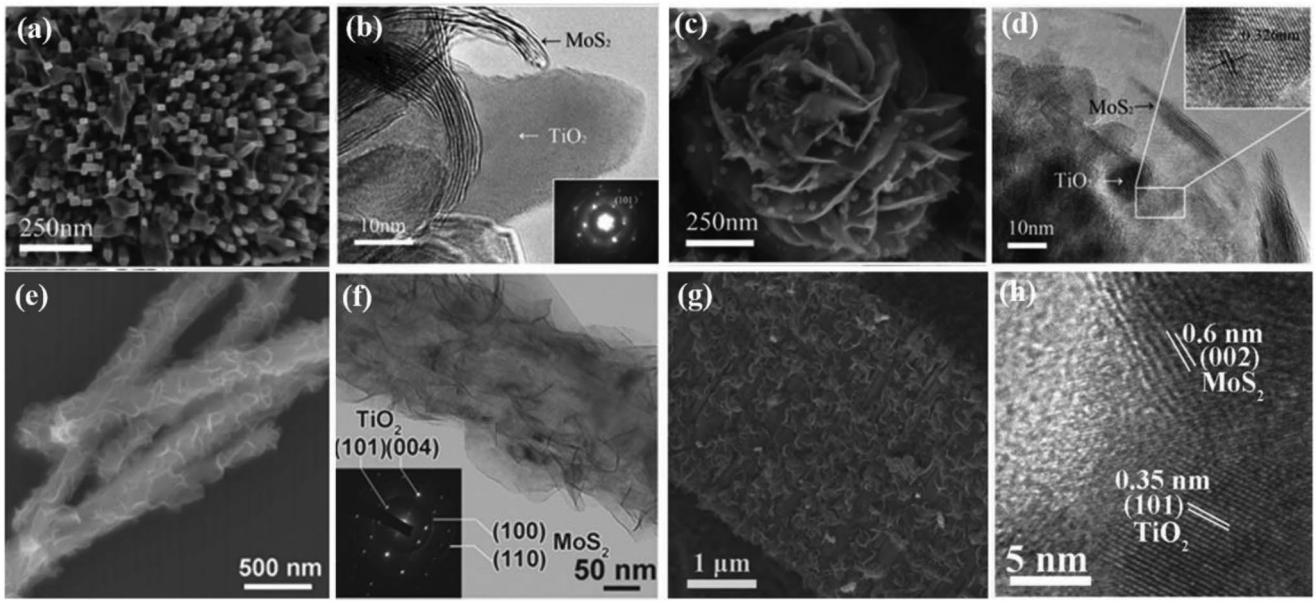

Figure 2. SEM and TEM images of a,b) TiO_2 rods@MoS_2 nanosheets composite, and c,d) MoS_2 nanoflowers@TiO_2 nanoparticles composite. Reproduced with permission.[31] Copyright 2015 Royal Society of Chemistry. e,f) TiO_2 nanobelts@MoS_2 nanosheets composite (50 wt% of MoS_2). Reproduced with permission.[15a] Copyright 2013 Wiley-VCH. g,h) TiO_2 nanotubes@MoS_2 nanosheets composite. Reproduced with permission.[33] Copyright 2016, Wiley-VCH.

The other intelligent strategy is doping with nonmetal impurities. For instance, considering comparable atomic size with oxygen, small ionization energy, metastable center formation, and good stability, nitrogen has been widely investigated to dope with TiO_2 in wastewater treatment application under visible light irradiation.[2a,28] Doping with N contributes to narrowed bandgap through embedding N atom into the lattice of TiO_2, which creates the overlap of O 2p states and N 2p states on the top of VB of TiO_2 at substitutional lattice sites or intergap states, thereby enhancing the visible light absorption. Tang et al.[29] found that the cooperative effect of N doping and MoS_2 nanosheets decoration helped greatly enhance the visible photocatalytic degradation of methyl blue (MB). Liu et al.[30] designed an efficient 3D flower-like core–shell structure photocatalyst (N-TiO_{2-x}@MoS_2) with codoped N and Ti^{3+} and coupled with MoS_2 nanosheets. Similarly, Ti^{3+} self-doping induced local states formed at the bottom of CB of TiO_2 by introducing Ti^{3+} or oxygen vacancies into the lattice, beneficial for visible light absorption.

2.2.2. Morphology Engineering and Dye Adsorption Capability

The morphological difference of MoS_2/TiO_2 heterojunctions generated from different synthetic routes exerts a huge impact on the photocatalytic activities. Yu group reported two types of MoS_2 titania heterojunctions via two facile hydrothermal processes.[31] One was a 3D TiO_2-based composite with wave-like MoS_2, defined as TiO_2@MoS_2 (**Figure 2**a,b), where single MoS_2 sheets consisting of 5–9 MoS_2 layers ran through the gaps between TiO_2 nanorods. Owing to large percentage of highly reactive (001) planes of TiO_2 nanorods as well as the increased number of gaps on the surface, the TiO_2@MoS_2 composites showed a better photocatalytic performance and adsorption ability. The other is a MoS_2 nanoflower based composite with TiO_2 nanoparticles (NPs) with a diameter of 10 nm, defined as MoS_2@TiO_2 (Figure 2c,d). The MoS_2@TiO_2 composites exhibited better field emission performance because of the vast distribution of TiO_2 NPs serving as sharp edges for emitting.

On the other hand, the layered MoS_2 nanosheets with a large surface area were reported to be excellent toward dye adsorption and the dye adsorption capability obviously matters in the subsequent catalytic process.[32] Zhou et al.[15a] reported a 3D hierarchical core–shell TiO_2@MoS_2 configuration via a hydrothermal route using TiO_2 nanobelts as template to inhibit the growth of MoS_2 crystals along *c*-axis, resulting in surface coating by few-layer (thickness of ≈5 nm, <7 layers) MoS_2 nanosheets (Figure 2e,f). The TiO_2@MoS_2 (50% wt MoS_2) heterostructures showed a strong adsorption toward Rhodamine B (RhB) with the adsorption value of 103.24 mg g^{-1} in dark owing to the large specific surface area (44.8 m^2 g^{-1}). In contrast, the synthesized MoS_2 NP-coated counterpart showed lower adsorption ability toward RhB with a value of 33.7 mg g^{-1}. They claimed that both the surface area and unique morphology of MoS_2 contributed to the strong dye adsorption ability, thus resulted in superior photocatalytic efficiency by completely degrading RhB in 20 min under visible light irradiation. Similarly, Li et al.[4b] demonstrated the fabrication of MoS_2/TiO_2 hybrid comprising few-layer MoS_2 nanosheets and ultrafine TiO_2 nanobelts with a high specific surface area (72.2 m^2 g^{-1}), which greatly enhanced the adsorption of dye molecules and separation ability of photo-induced carriers, endowing a high photocatalytic efficiency in both UV and visible light regions.

Besides TiO_2 nanobelts, TiO_2 nanotube arrays were used as substrates to load MoS_2 nanosheets that grew evenly over both the tube top surface and the intertubular voids with a large

© 2019 WILEY-VCH Verlag GmbH & Co. KGaA, Weinheim

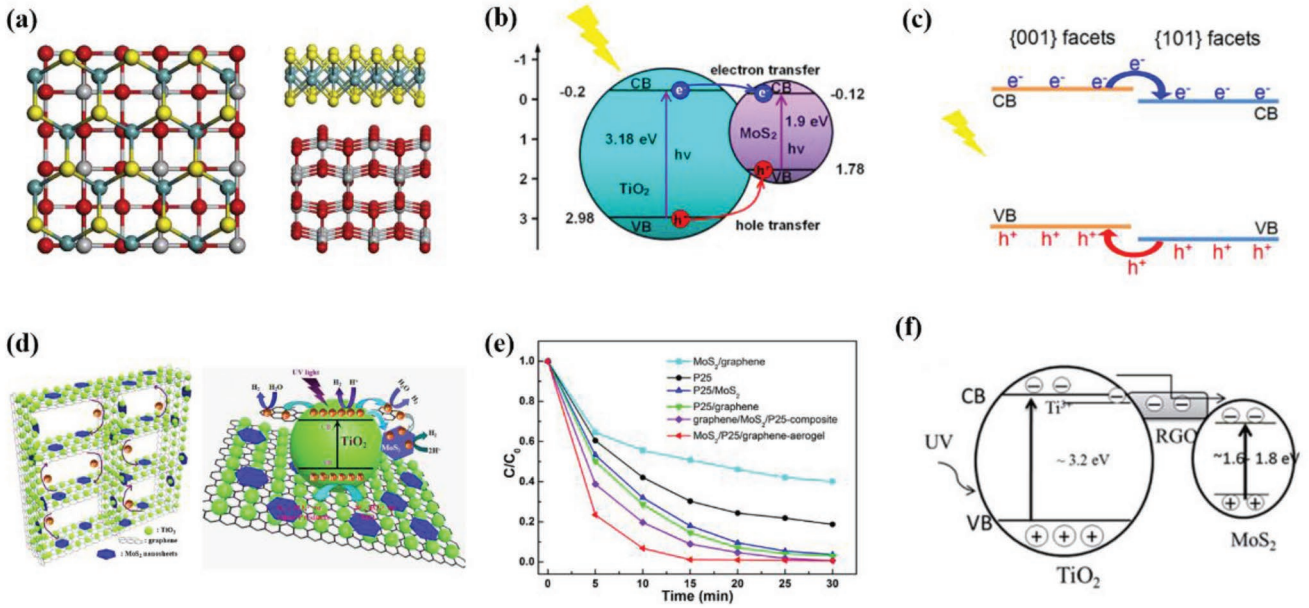

Figure 3. a) Structure model for the interface between MoS_2 and TiO_2(001) surface: (Left) top view and (Right) side view. Red, light gray, yellow, and blue-green balls represent O, Ti, S, and Mo, respectively. b) A schematic diagram of carrier exchange in the heterostructure, and c) photoinduced electrons and holes separated by (101) and (001) facets of anatase TiO_2. Reproduced with permission.[40] Copyright 2016 Elsevier. d) Schematic structure and proposed reaction mechanism of 3D MoS_2/P25/graphene-aerogel networks, and e) their catalytic performance for MO degradation. Reproduced with permission.[42] Copyright 2014 Elsevier. Copyright 2019 Elsevier. f) The charge carriers transfer process in TiO_2-RGO/MoS_2 hybrid composite under UV light irradiation. Reproduced with permission.[43] Copyright 2016 The Royal Society of Chemistry.

scale (Figure 2g,h).[33] The efficiency toward RhB degradation of TiO_2@MoS_2 composite was ≈1.8 times higher than that of commercially available P25. Moreover, in order to overcome the drawbacks of suspension catalytic systems of MoS_2/TiO_2 powdery composites, activated carbon fibers with high specific surface area[34] and porous zeolite[35] were reported to use as the carrier for MoS_2/TiO_2 catalyst to pursue the synergism of adsorption and catalysis.

2.2.3. Effect of Exposed Crystal Facets in TiO_2

In addition to surface area, morphology of composites, and loading amounts of MoS_2, the exposed crystal facets of TiO_2 are critical in determining the photocatalytic efficiency. There are three different exposed facets: (001), (100), and (101) for TiO_2, and their average surface energies follow the order: 0.90 J m^{-2} for (001) > 0.53 J m^{-2} for (100) > 0.44 J m^{-2} for (101).[36] Most anatase TiO_2 crystals were dominated by the thermodynamically stable (101) facets instead of (001) with higher surface energy.[37] Many experimental and theoretical results have revealed that the (001) facets show higher photocatalytic activity than (101) due to the presence of more undercoordinated atoms.[36,38] While for MoS_2/TiO_2 (001) composite system, the first systematically theoretical study on electronic and optical absorption properties was reported by Cao's group using density functional theory (DFT) in 2014.[39] The layer-structured MoS_2 combination effects on energy gap, interfacial charge transfer, and visible light response of the composite were systematically investigated. Then Zhang et al.[40] demonstrated that 2D MoS_2 grown on (001) facets of TiO_2 nanosheets displayed a face-to-face contact, which was an ideal transmission channel to effectively separate the photocarriers with less scattering (**Figure 3**a–c). The CB and VB of (001) facets of TiO_2 are little higher than those of (101) facets, so photoinduced electrons would transfer to (101) surface while photoinduced holes would transfer to (001) surface, and then be extracted by MoS_2 for photodegradation.

2.2.4. Effect of Electrical Conductivity

The poor electrical conductivity of MoS_2 highly restricts its cocatalytic activity, thus the photoelectrons can be derived from photocatalysts, and the recombination of e–h pairs is impeded. Other conducting materials (graphene,[41] graphene aerogel,[42] and reduced graphene oxide[43]) are introduced to improve the electrical conductivity and activity. Graphene exhibits high specific surface area, excellent electronic behavior, and superior electron mobility, and it has been recognized as an efficient cocatalyst for photocatalytic reactions. Gao et al.[41] reported a facile one-pot solvothermal method to fabricate MoS_2 QDs-graphene-TiO_2 composite where graphene played a key role during the formation of MoS_2 QDs instead of layered nanosheets. However, the large accessible surface area in the composite system was unfortunately sacrificed given that graphene sheets were prone to aggregate with each other, hindering the electrolyte ion infiltration and resulting in a great loss of electroactive sites. Then 3D graphene macrostructures (hydrogels and aerogels) have been developed to form ternary composites,[42] and the improved photoactivity was attributed to the porous framework, good electrical conductivity, and the maximization of

© 2019 WILEY-VCH Verlag GmbH & Co. KGaA, Weinheim

accessible sites, and the positive synergetic effect among the three components in the hybrid (Figure 3d,e). Interestingly, the graphene oxide can be (partly) reduced to graphene-like sheet by removing the surface attached oxygen-containing functional groups to restore the sp^2-hybridized network. The reduced graphene oxide (RGO) sheets are usually considered as one kind of chemically derived graphene and they were reported[44] to show better properties than GO. Ke's group[43] reported anatase TiO_2 NPs coupled with a RGO/MoS_2 hybrid junction (TiO_2-RGO/MoS_2) where RGO behaved like a conductor. It accepted only electrons and transported them to the active sites of MoS_2 cocatalyst surface under UV light irradiation (Figure 3f). The electron paramagnetic resonance (EPR) spectra revealed that the interfacial charge transferred from TiO_2 to MoS_2 surface via the RGO nanosheets.

2.3. Solar Hydrogen Production

Typically, the photocatalytic H_2 production activity of TiO_2 is strongly dependent on the type and amount of cocatalyst considering the poor activity of bare TiO_2.[45] When coupling MoS_2 with TiO_2, both experimental results[15a,46] and theoretical calculations[39] have revealed an obvious redshift in the optical absorption edge and an enhanced absorption ability in the visible and UV light region compared with bare TiO_2, as a result of feasible charge separation and transfer, and improved visible light response. Many recent reports indicated that layered MoS_2 could function as an effective electron-cocatalyst in photocatalytic hydrogen evolution reaction (HER) and even become a promising alternative to noble-metal catalysts.[47]

The principal catalytic mechanism for layered MoS_2 is that the unsaturated S atoms on the crystalline MoS_2 edges can work as the efficient active sites to rapidly capture protons from solution, and then promote the direct reduction of H^+ to H_2 by photogenerated electrons[8,48] whereas the basal planes are catalytically inert, limiting the overall performance. By reducing the dimension along the in-plane direction, the edges of 2D MoS_2 are extensively exposed, and the electronic and catalytic properties are effectively enhanced. These edge sites have been demonstrated to possess metallic electronic states.[49] Therefore, tuning the architecture of MoS_2 to preferentially edge-exposed sites as much as possible is promising in the improved solar hydrogen production performance.[9b] Besides, the electrical conductivity, efficient interfacial charge separation efficiency and crystal phases of MoS_2 also play significant roles in the hydrogen production performance. In most cases, several factors exert a synergistic effect. **Table 2** lists the water splitting performance of MoS_2/TiO_2-based photoelectrodes.

2.3.1. Morphology Control

To date, various MoS_2 morphologies in the TiO_2-based heterojunction have been developed to expose abundant active edge sites, including 0D NPs,[46b,d,51] 2D few-layer nanosheets,[15a,46a,c,52] and 3D nanoflowers.[53] The 2D nanosheets would be more active than MoS_2 NPs owing to a larger amount of exposed edge sites. The commonly loading strategy is a facile hydrothermal method which usually involves sodium molybdate and thioacetamide/sodium sulfide as precursors for the Mo and S sources, respectively. After reaction in the Teflon-lined stainless-steel autoclave for a certain period, few-layered MoS_2 nanosheets with abundant active sites can be obtained. For instance, Yuan et al.[46c] reported a novel 2D-2D MoS_2/TiO_2 composite where ≈6–9 layers of MoS_2 nanosheets were loaded on the surface of anatase TiO_2 with exposed (001) facets, presenting superior H_2 evolution performance (2145 μmol h^{-1} g^{-1}), even better than Pt/TiO_2 photocatalysts with a 0D-2D structure (1368 μmol h^{-1} g^{-1}), indicating that MoS_2 nanosheets could act as a more efficient cocatalyst than Pt for photocatalytic H_2 production (**Figure 4**a–c). The reason was most probably due to the greatly increased interfacial contact and larger specific surface area for cocatalyst dispersion as well as a great number of active sites. Moreover, in the presence of a dye photosensitizer (Eosin Y), few-layer MoS_2 nanosheet–porous TiO_2 nanowire (shell–core) hybrid exhibited higher visible-light photoactivity with hydrogen generation rate of 16.7 mmol h^{-1} g^{-1} using triethanolamine (TEOA) as sacrificial agent.[52]

Interestingly, in contrast to hydrothermal method that required high energy or time-consuming, Zeng et al.[54] reported a self-sustained photo-driven microbial fuel cell (PMFC) reactor for in situ preparation of MoS_2 nanosheets with more edge sites and constructed MoS_2/polydopamine(PDA)/TiO_2 electrode for H_2 generation online (Figure 4d–f). The biosynthesis route also provided special dual-electrons mode to dramatically hinder the recombination of photogenerated e–h pairs, leaving more opportunities for photoelectrons to take part in HER under bioelectric field. The ternary composite exhibited high electrocatalytic and photoelectrocatalytic activities.

2.3.2. Defect Engineering

The design of MoS_2 nanostructures with preferential exposure of active edge sites is dominant for enhanced PEC performance. For MoS_2, the preferentially exposed basal planes of the nanosheets are the thermodynamically stable (002) planes rather than the active edge planes.[55] In this regard, defect engineering may benefit the structural design to expose active edge sites by forming cracks on the surfaces of the nanosheets, and thereby dramatically improving the performance. Xie's group[56] proposed a scalable pathway to realize defect-rich MoS_2 ultrathin nanosheets by using excess amount of thiourea, because the absorbed CN_2H_4S molecules on the surface of primary MoS_2 nanocrystallites can partially hinder the oriented crystal growth and form a defect-rich quasiperiodic structure. Since then, many studies employed this strategy to produce defect-rich MoS_2 nanosheets and widely applied in electrochemical energy storage fields.[57] In the PEC processes, defects also play a vital role by providing extra active sites for surface reaction and serving as recombination centers for electrons and holes.[58] To take full advantage of narrow bandgap of MoS_2, Guo's group[59] proposed a combined physical vapor deposition (PVD) and chemical vapor deposition (CVD) strategy to prepare MoS_2@TiO_2 laminate heterostructures with nearly full-solar-spectrum absorption. Both experimental results and

© 2019 WILEY-VCH Verlag GmbH & Co. KGaA, Weinheim

Table 2. Hydrogen generation performance of MoS_2/TiO_2 composite based photocatalysts.

Photoelectrodes	Loading method	Light source	Sacrificial reagent	Surface area	Amount	Performance (H_2 yield, J_0,[a] $\eta_{(10)}$,[b] J_{ph},[c] and Tafel slope; AQY,[d] AQE,[e] ABPE[f])	Ref.
TiO_2 nanobelts@MoS_2 nanosheets	Hydrothermal	300 W Xe lamp, $\lambda = 280–700$ nm	0.35 M Na_2S + 0.25 M Na_2SO_3	44.9 $m^2\ g^{-1}$	1.6 mg	1600 μmol $h^{-1}\ g^{-1}$	[15a]
MoS_2 nanosheets/TiO_2 nanosheets	Hydrothermal	300 W Xe lamp	10 v% CH_3OH-H_2O	–	100 mg	2145 μmol $h^{-1}\ g^{-1}$; AQY(360 nm) = 6.4%	[46c]
TiO_2 nanofiber @MoS_2 nanosheets	Hydrothermal	300 W Xe lamp, $\lambda = 320–780$ nm	0.35 M Na_2S + 0.25 M Na_2SO_3	27 $m^2\ g^{-1}$	4 mg	1.68 mmol $h^{-1}\ g^{-1}$ ($\lambda > 320$ nm); 0.49 mmol $h^{-1}\ g^{-1}$ ($\lambda > 420$ nm)	[46a]
MoS_2 NPs/TiO_2 NPs	Ball-milling	300 W Xe lamp, $\lambda > 380$ nm	15% CH_3OH-H_2O	–	200 mg	753.5 μmol $h^{-1}\ g^{-1}$	[46d]
MoS_2 NPs/TiO_2 NPs	Photodeposition-calcination	300 W Xe lamp ($\lambda > 300$ nm)	5% HCOOH	–	30 mg	73.3 μmol $h^{-1}\ g^{-1}$	[50]
TiO_2 nanofibers@MoS_2 nanosheets	Hydrothermal	300 W Xe lamp, $\lambda > 420$ nm	5 v% TEOA + Eosin Y dye	66 $m^2\ g^{-1}$	1.0 mg	16.7 mmol $h^{-1}\ g^{-1}$	[51]
MoS_2 nanosheets/ TiO_2 NPs	Solvothermal	AM 1.5G (300 W Xe lamp)	20 v% CH_3OH		50 mg	119.5 μmol $h^{-1}\ g^{-1}$	[50]
MoS_2 nanosheets/TiO_2 nanobelts	Hydrothermal	Solar simulator (300 W Xe lamp)	20 v% CH_3OH-H_2O		100 mg	75 μmol $h^{-1}\ g^{-1}$	[4b]
MoS_2 nanosheets/PDA/ TiO_2 nanotube arrays	Bioelectrochemical synthesis	Xe lamp, 33 mW cm^{-2}; $\lambda > 420$ nm		–	–	4.32 $m^3\ m^{-3}\ d^{-1}$; $\eta_{(10)}$ = 36 mV (SHE), 53 mV dec^{-1}	[53]
MoS_2 nanosheets/CdS NPs/porous TiO_2	Hydrothermal	300 W Xe lamp, $\lambda > 400$ nm	0.35 M Na_2S + 0.25 M Na_2SO_3	63.39 $m^2\ g^{-1}$	50 mg	4146 μmol $h^{-1}\ g^{-1}$	[63b]
TiO_2 nanofibers@MoS_2 nanosheets@CdS NPs	Hydrothermal	300 W Xe lamp, $\lambda = 320–780$ nm	0.35 M Na_2S + 0.25 M Na_2SO_3	97 $m^2\ g^{-1}$	20 mg	12.3 mmol $h^{-1}\ g^{-1}$ (solar light) or 6.2 mmol $h^{-1}\ g^{-1}$ (visible light); AQE(365 nm) = 70.5%, AQE(420 nm) = 57.6%	[63a]
TiO_2 NPs/MoS_2 nanosheets/graphene	Hydrothermal	Four UV LED (3 W, 365 nm)	25% CH_3CH_2OH-H_2O	171 $m^2\ g^{-1}$	80 mg	≈2066 μmol $h^{-1}\ g^{-1}$; AQE(365 nm) = 9.7%	[66]
g-C_3N_4 flower-like sphere/MoS_2/TiO_2 NPs	Hydrothermal	300 W Xe lamp, $\lambda > 400$ nm	1:3 CH_3OH:H_2O	92.9 $m^2\ g^{-1}$	100 mg	1250 μmol $h^{-1}\ g^{-1}$	[51c]
Au nanodots/MoS_2 nanosheets/TiO_2 nanotube arrays	CVD	UV light	0.5 M H_2SO_4		–	J_0 = 71.6 μA cm^{-2}; $\eta_{(10)}$ = 166 mV(Ag/AgCl) and 72 mV dec^{-1}	[68a]
Ag NPs/MoS_2 nanosheets/TiO_{2-x} nanobelts	Hydrothermal	300 W Xe lamp, $\lambda \geq 420$ nm	20 v% CH_3OH-H_2O	–	50 mg	≈1.98 mmol $h^{-1}\ g^{-1}$	[68b]
MoS_2 nanoflakes/TiO_2 film/Ti	Commercially available	AM 1.5 G solar simulator (300 mW cm^{-2})	0.5 M H_2SO_4	–	–	$\eta_{(10)}$ = 114 mV(RHE), 99 mV dec^{-1}	[69]
MoS_2 NPs/Pt NPs/ TiO_2 NPs	Hydrothermal	300 W Xe lamp, $\lambda > 400$ nm	0.35 M Na_2S + 0.25 M Na_2SO_3		20 mg, 1 cm^2	4.18 mmol $h^{-1}\ g^{-1}$, AQE (420 nm) = 12.54%	[67a]
Pt NPs@MoS_2 nanosheets/TiO_2(B) nanobelts	Hydrothermal	250 W Xe lamp, $\lambda \approx 370–730$ nm	0.5 M H_2SO_4		≈0.34 mg cm^{-2}	J_0 = 0.296 mA cm^{-2}; $\eta_{(10)}$ = 74 mV(Ag/AgCl) and 30 mV dec^{-1}	[51a]
TiO_2 nanorod array/ 1T-MoS_2 nanosheets	Lithium intercalation Drop casting	AM 1.5 G solar simulator (100 mW cm^{-2})	0.5 M Na_2SO_4		≈1 cm^2	J_{ph} ≈ 2.4 mA cm^{-2}; ABPE = 0.81%@0.51 V (Ag/AgCl)	[70]
Porous TiO_2/CdS QDs/1T-MoS_2 nanosheets	Chemical exfoliation method	Solar simulator, $\lambda > 400$ nm	0.25 M Na_2S + 0.35 M Na_2SO_3	–	–	1.47 mL $h^{-1}\ cm^{-2}$@ 1 V(RHE)	[71e]

© 2019 WILEY-VCH Verlag GmbH & Co. KGaA, Weinheim

Table 2. Continued.

Photoelectrodes	Loading method	Light source	Sacrificial reagent	Surface area	Amount	Performance (H_2 yield, J_0,[a] $\eta_{(10)}$,[b] J_{ph},[c] and Tafel slope; AQY,[d] AQE,[e] ABPE[f])	Ref.
MoS_2 nanosheets@ TiO_2 nanorod arrays	Hydrothermal	Solar simulator (300 W Xe lamp)	0.35 M Na_2S + 0.25 M Na_2SO_3		≈9 cm^2	8.43 μmol cm^{-2} h^{-1}	[71a]
N-TiO_{2-x} nanospheres@MoS_2 nanosheets	Hydrothermal	300 W Xe lamp, $\lambda > 420$ nm	1 M KOH		50 mg	1.882 mmol h^{-1} g^{-1}	[30]
Ti_3C_2 MXene@TiO_2 nanosheets@MoS_2 nanosheets	Hydrothermal	AM 1.5G solar simulator (300 W Xe lamp)	Acetone + TEOA	20.065 m^2 g^{-1}	10 mg	≈6.4 mmol h^{-1} g^{-1}	[63c]

[a]J_0: exchange current density; [b]$\eta_{(10)}$: overpotential at 10 mA cm^{-2}; [c]J_{ph}: photocurrent density; [d]AQY: apparent quantum yield; [e]AQE: apparent quantum efficiency; [f]ABPE: applied bias to PEC hydrogen generation efficiency.

calculations confirmed that local surface plasmonic resonance (LSPR) of this nonmetal plasmonic heterostructure substantially contributed to superior photocatalytic activity for H_2 evolution. It is worth noticing that S-vacancy and nonstoichiometric features of MoS_2 nanoflakes were where free electrons and plasmonic resonance processes originated.

Apart from S-vacancy in MoS_2,[60] numerous studies are emerged regarding the defect engineering of MoS_2, including oxygen vacancy,[61] metal defects,[62] n-doped,[53a] and p-type doped MoS_2.[63]

2.3.3. Facilitating the Interfacial Charge Transfer

A Secondary Semiconductor Cosensitization: To further facilitate the separation of photogenerated e–h pairs in MoS_2/TiO_2 heterojunction, a secondary semiconductor was developed to form ternary composites.[64] Li et al.[64c] constructed a 2D-2D-2D heterojunction with dual cocatalysts in which 2D Ti_3C_2 MXene and MoS_2 nanosheets were acted as the electron mediator and reduction cocatalysts, respectively, on the (101) facets of TiO_2 with mainly exposed high-active (001) facets (Figure 4g). In this structure, electrons and holes are photogenerated on the (001) surfaces of TiO_2, and then they can be transferred onto (101) and (001) facets of TiO_2 due to the presence of surface heterojunction,[65] respectively. While the MoS_2 can capture photogenerated electrons of (101) facets and behaved as reduction active sites. Moreover, the highly electron conductive Ti_3C_2 acted as a source of titanium and a pathway to transfer photogenerated electrons. Thus, the synergetic effect of the ternary composite could effectively enhance the charge separation efficiency, leading to improved photocatalytic H_2 production.

Nanocarbon Modification: Graphene with an appropriate redox potential that is less negative than the CB of TiO_2 and more negative than the H^+/H_2 potential[66] was found to be an attractive supporting material for HER. The first study on the synergetic effect of MoS_2 and graphene as cocatalysts of TiO_2 with superior photocatalytic H_2 production activity was reported by Xiang et al., which reached a high H_2 production rate of 165.3 μmol h^{-1} (≈2066 μmol h^{-1} g^{-1}) with a quantum efficiency of 9.7% at 365 nm.[67] The photogenerated electrons on the CB of TiO_2 could easily transport to MoS_2 nanosheets through graphene, which acted as a conductive electron transport "highway," and then reacted with the adsorbed H^+ ions at the edges of MoS_2 to produce H_2. Then Yang et al.[53c] reported a ternary g-$C_3N_4/MoS_2/TiO_2$ composite for H_2 evolution due to the positive synergetic effect between MoS_2 and g-C_3N_4 components, which served as an electron collector and a source of active adsorption sites, respectively.

Metal Decoration: Pt-group noble metals activated ternary composites have been explored to be the most efficient conventional electrocatalysts due to their low onset overpotential and high electrocatalytic activity, but the high cost and rarity in nature largely limit their industrial-scale utilization.[53a,68] Li et al.[68a] prepared a ternary MoS_2/Pt-TiO_2 photocatalyst in which Pt NPs were distributed on the surface of TiO_2-MoS_2 and between their junctions uniformly. The ternary structure exhibited an apparent quantum yield (AQY) value of 12.54% at 420 nm, outperforming both the binary MoS_2-TiO_2 and Pt-TiO_2 systems owing to the efficient electron transport path and e–h separation mechanism. Pt NPs played two roles of storing CB electrons of TiO_2 and acting as cocatalyst for reduction of protons to H_2. Based on it, Paul et al.[53a] reduced Pt consumption without compromising the HER activity. Interestingly, S was doped in the TiO_2 layer causing a high density of electrons in TiO_2 that migrated to the MoS_2 layer inducing n-type doping and thus TiO_2 acted as an efficient photocathode.

Besides, other metal decoration such as Au and Ag was adopted to ameliorate the low conductivity of TiO_2-MoS_2 heterojunction and boost the charge transport efficiency.[69] Tao et al.[69a] developed a ternary composite Au/MoS_2/TiO_2 where the coverage and dimension of Au nanodots were well controlled by varying deposition time. The charge transfer resistance (R_{ct}) values from Nyquist plot confirmed that the Au/MoS_2/TiO_2 hybrid (128 Ω) exhibited more facile electrode kinetics toward HER compared with MoS_2/TiO_2 heterostructure (671 Ω).

Controlling the Crystal Phases: The introduction of TiO_2 homojunction[70] with MoS_2/TiO_2 heterojunctions exerted a positive effect on the HER performance by effectively regulating the charge separation and transfer pathways. More complex situation was found on the introduction of different crystal phases of MoS_2. Generally, there are two main coordination configurations for Mo atoms: the octahedral (1T phase)

© 2019 WILEY-VCH Verlag GmbH & Co. KGaA, Weinheim

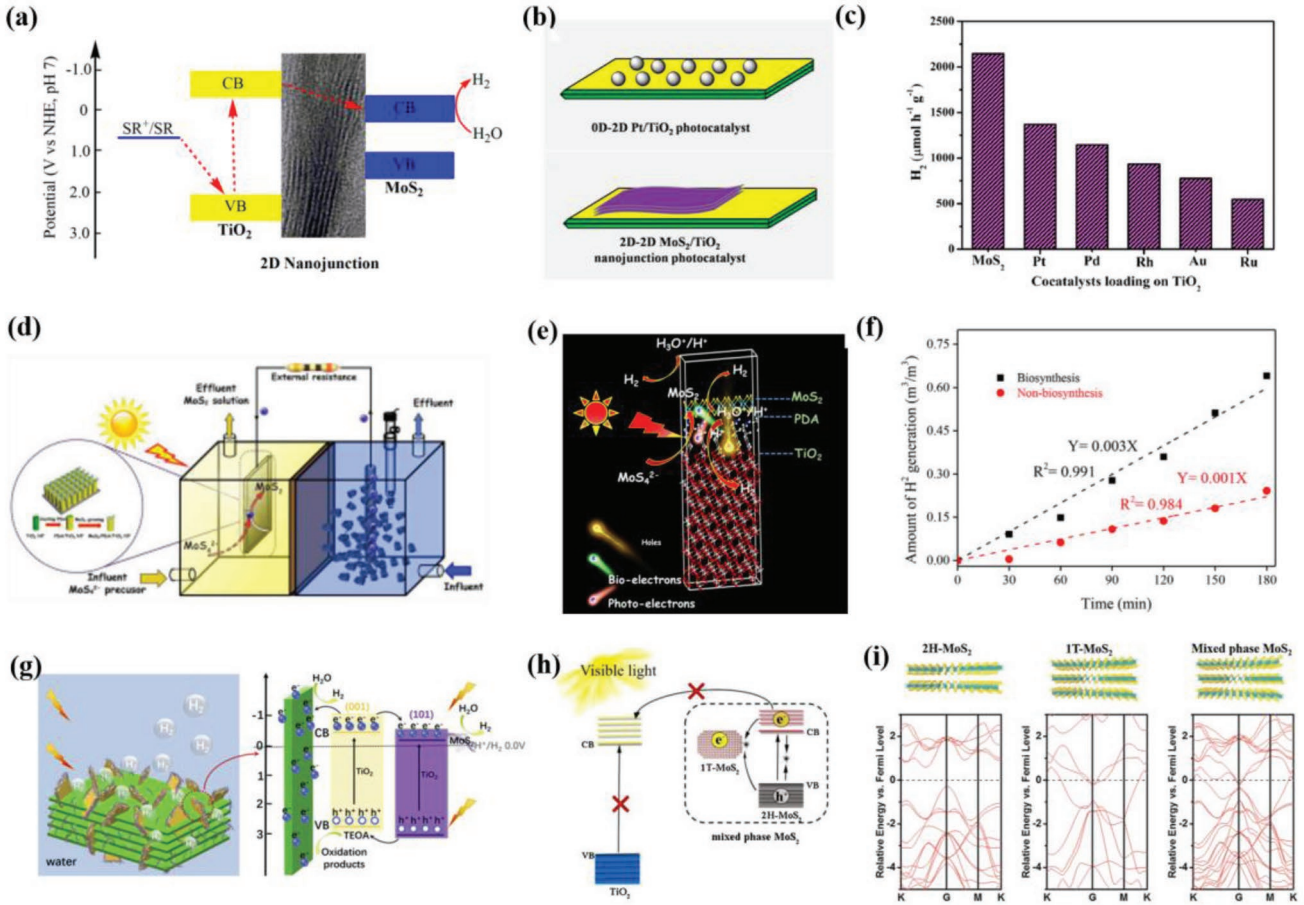

Figure 4. a) Energy diagram of charge transfer and photocatalytic H_2 production processes in 2D-2D MoS_2/TiO_2 photocatalyst, b) Schematic diagrams showing that the 2D-2D MoS_2/TiO_2 photocatalyst exhibits much larger contact interface between the light-harvesting semiconductor and cocatalyst in comparison to the 0D-2D Pt/TiO_2 composite. c) Rate of H_2 production on TiO_2 loaded with 0.50 wt% of different cocatalysts under irradiation from a 300 W Xe lamp in 100 mL of 10 vol% aqueous methanol solution. Reproduced with permission.[46c] Copyright 2015 American Chemical Society. d) Schematic illustration of fabrication MoS_2 in the photo-driven microbial fuel cell system, e) possible catalytic mechanism, and f) catalytic performance of MoS_2/polydopamine/TiO_2 for H_2 generation. Reproduced with permission.[54] Copyright 2019 Elsevier. g) Schematic photocatalytic reaction mechanism for Ti_3C_2@TiO_2@MoS_2 composites under solar light irradiation. Reproduced with permission.[64c] Copyright 2019 Elsevier. h) Charge transfer process of MoS_2@TiO_2 under visible light and i) Perdew–Burke–Enzerhof (PBE) calculated band structures of 2H-MoS_2, 1T- MoS_2, and mixed phase MoS_2. Reproduced with permission.[72a] Copyright 2018 Elsevier.

and trigonal prismatic (2H and 3R phases). 2H semiconducting phase is dominant and more stable in nature, which has two layers per unit cell stacked in the hexagonal symmetry. The unstable 3R type has three layers per cell in rhombohedral symmetry, and can be easily transformed to 2H phase upon heating. While the shift of one of sulfur layers leads to the generation of 1T crystal phase corresponding to octahedral coordination of metal atoms. The 2H semiconducting phase can form composites with other semiconductors, while the 1T metallic phase only works as a cocatalyst like metal Pt. Thus, it is of great interest to probe the influence of these phases on the PEC performance.

Previous studies have suggested that 1T-MoS_2 has higher catalytic activity than 2H-MoS_2 due to superior electron conductivity (3500 S m^{-1} for 1T MoS_2; 1.43 S m^{-1} for 2H-MoS_2)[71] and more active edge sites for H_2 evolution.[71,72] Early in 2015, Raja et al.[72e] found that the biphasic crystalline structure (2H and 1T) with clear grain boundaries existed in a single layer of chemically exfoliated MoS_2 with lattice fringes estimated to be 0.30 and 0.26 nm, respectively, in consistent with the literature.[73] The mixed phase MoS_2 coupled with TiO_2 based heterojunction has a more complex situation for H_2 evolution considering the different catalytic mechanism of 2H semiconducting phase and 1T metallic phase. Very recently, Liu et al.[72a] for the first time have clearly verified the photogenerated electron transfer process and photocatalytic mechanism between the mixed phase MoS_2 and TiO_2. When 2H-MoS_2 layer was intercalated into the lattice of 1T-MoS_2, the newly introduced energy band located in the vicinity of the pristine gap, leading to a continuous band across the Fermi level (Figure 4h,i). This result indicated that the mixed phase few-layer MoS_2 nanosheets apparently showed the characteristic of 1T-MoS_2 like Pt rather than as a semiconductor, which was favorable for accepting the photogenerated electrons from TiO_2 to produce hydrogen. And the designed mixed phase MoS_2@TiO_2 exhibited two times higher activity than Pt@TiO_2 for photocatalytic H_2 evolution.

© 2019 WILEY-VCH Verlag GmbH & Co. KGaA, Weinheim

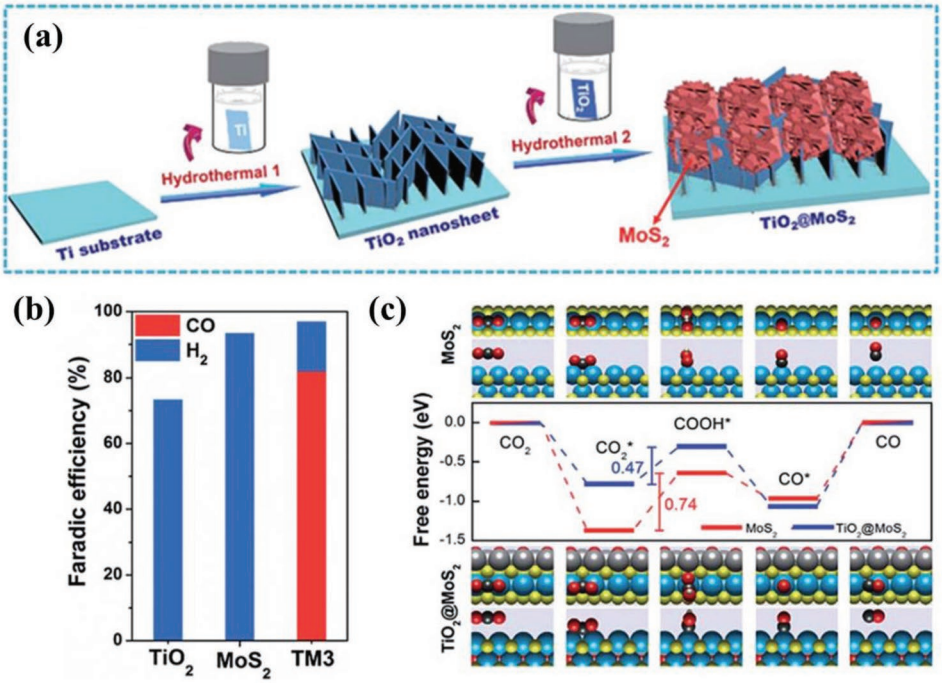

Figure 5. a) Schematic illustration of the formation of TiO_2@MoS_2 architectures. b) Faradaic efficiency of CO and H_2 at –0.70 V for TiO_2, MoS_2, and TM_3 (TiO_2@MoS_2). c) DFT calculated zero potential free energy diagrams for the CO_2RR to CO on the Mo exposed edges of monolayer MoS_2 and TiO_2@MoS_2 (H_2O and H are omitted for clarity). (O: red, S: yellow, C: black, H: white, Ti: gray, and Mo: light blue.) Reproduced with permission.[75d] Copyright 2018, Royal Society of Chemistry.

2.4. Photocatalytic CO_2 Reduction

Photocatalytic CO_2 reduction into hydrocarbon energy fuels has attracted many attentions in recent years. Since the discovery of CO_2 photoreduction by semiconductor by Inoue's group,[74] tremendous endeavor has been done to realize CO_2 conversion more economically. There are a few reports on MoS_2/TiO_2 heterojunctions acting as a catalyst for CO_2 reduction reaction (CO_2RR).[75] As reported, the conduction band minimum (CBM) of TiO_2 (–0.29 eV) and MoS_2 (–0.15 eV) are both more positive than the reduction potential of CO_2/CH_4 (–0.24 V), CO_2/CH_3OH (–0.38 V), CO_2/HCHO (–0.48 V), CO_2/CO (–0.53 V), CO_2/HCO_2H (–0.61 V).[15b,76] It indicates that no matter how to couple TiO_2 with MoS_2 the hybrid nanostructured material fail to have enough reductive ability for photocatalytic reduction of CO_2. Li et al.[75a] found that the yield was very low with gradually reduced Faraday efficiency when the composite electrode was used as cathode for electrocatalytic (EC) reducing CO_2 to methanol due to the unmatched CBM. Thus, they designed a new photoenhanced electrocatalytic (PEEC) way and obvious improvement on the faradaic efficiency (from 42.2% for EC to 1111.58% for PEEC and methanol yield (from 6.32 to 14.49 mmol L^{-1}) after applying illumination were achieved.

As discussed before, the unsaturated S atoms on the exposed edges of layered MoS_2 are favorable for HER, while Mo atoms on the exposed edges avail the CO_2RR as reported by Asadi in 2014.[77] Hence, fewer unsaturated S and more Mo atoms on the exposed edges of MoS_2 may favor the CO_2RR, which is a big challenge to synthesize this kind of MoS_2. Yu et al.[75d] proposed a smart strategy to prepare integrated 3D TiO_2@MoS_2 architectures in which TiO_2 nanosheet arrays worked as a scaffold to sustain the upper MoS_2 spheres to be spatially divergent against aggregation, providing a large open space for CO_2 adsorption and allowing a full contact with the electrolyte (**Figure 5**a–c). The unique structure also helped avoid the mismatch at the interface. The prepared TiO_2@MoS_2 composite (TM3) showed a high activity toward CO_2RR with a CO selectivity of ≈85% at –0.70 V. The formation of Ti—S bonds revealed by DFT calculations changed the electric properties of MoS_2 layer and the adsorption characteristics of Mo exposed edges. The modulated MoS_2 was robust for CO_2 reduction due to the decrease of both binding energy of CO_2 and energy barriers of CO_2RR pathways (0.74 eV for MoS_2 decreased to 0.47 eV over TiO_2@MoS_2), which was further verified by the experimental electrochemical performance.

2.5. Other Applications

The MoS_2/TiO_2 heterojunctions are also reported to be applied in other energy storage applications, such as lithium-ion storage,[78] supercapacitors,[79] and dye-sensitized photovoltaic devices.[80] Dai et al.[105] reported a strategy to prepare lattice mismatched TiO_2@MoS_2 composites with core/multishell nano-onion heterostructure, initiating from atomically thin TiO_2 nanosheets followed by hydrothermal growth of MoS_2 shell with conformal surface coating. The composite exhibited superior electrochemical energy storage performance, especially at high current densities owing to the unique architecture.

© 2019 WILEY-VCH Verlag GmbH & Co. KGaA, Weinheim

2.6. Drawbacks of MoS_2/TiO_2

MoS_2 nanostructures tend to form irregular aggregates or stacked layers which greatly shelters the catalytically active sites owing to overlapping. Many studies reported the successful realization of visible absorption based on MoS_2/TiO_2 heterostructure, however, it is still crucial to grow monolayer MoS_2 to take advantage of the type II band alignment and achieve effective separation of e–h pairs. In addition, the different phases of MoS_2 (2H, 1T) affect its conductivity and exposed active sites as well as play different role in the PEC processes, and how to precisely control the proper phase in the MoS_2/TiO_2 composite is still a big challenge. Most importantly, intentionally tuning the structure of MoS_2 to preferentially edge-exposed sites needs more attention.

3. CdS/TiO_2 Heterostructures

The second well-reported metal sulfide is CdS with a direct bandgap of ≈2.4 eV, which broadens the photocatalytic performance to visible light region. The small bandgap of CdS allows the absorption of low energy photons from the visible light region up to 520 nm and its CB is more negative than that of TiO_2 which should be beneficial to enhance the charge separation (Scheme 1). Therefore, sensitization of TiO_2 with CdS nanostructures would make the photo-(electro-)chemical performance superior by increasing the ability to harvest visible light as well as improving interfacial charge separation. However, low photocatalytic efficiency and severe photocorrosion were reported for CdS without the presence of sacrificial reagents.

3.1. Photodegradation of Pollutants

The type II TiO_2/CdS heterojunction can effectively separate e–h pairs, and result in superior performance in the photodegradation of organic pollutants in the waste water.[81] The accumulated electrons in the CB of TiO_2 can be transferred to oxygen to form H_2O_2, which could be further reduced to hydroxyl radicals. The formed hydroxyl radicals could further degrade or mineralize organic dye to end products (H_2O and CO_2). Furthermore, holes accumulated in the VB of CdS could be consumed by participating in reaction with dye molecules directly to form intermediates or mineralized products.[82] Generally, the structure morphology and specific surface area of the heterostructure, exposed active facets of TiO_2, and the effective contact between CdS and TiO_2 obviously affect the photocatalytic performance. Here, we simply reviewed from TiO_2 morphological nanostructures point of view.

3.1.1. 0D TiO_2

It was highly desirable to prepare porous CdS/TiO_2 photocatalysts with a large surface area to enrich the amount of active sites, which was beneficial to the reactant molecules diffusion and light absorbing ability.[83] In addition, a direct contact between CdS and TiO_2 also played a vital role for efficient charge injection[84] which could not be achieved by ex situ methods in which presynthesized CdS NPs were deposited on the surface of TiO_2. Yang et al.[84a] proposed an in situ hydrothermal method to prepare TiO_2-CdS heterostructures which realized over 90% degradation ratio for RhB in 15 min under UV–vis light irradiation. Mani et al.[84b] developed a one-pot synthesis method through combustion technique to grow CdS/TiO_2, which induced proper connectivity between the constituent materials and facilitated faster electron transfer rate at the heterojunction. Ternary composites were further developed to increase the photocatalytic performance. For instance, modifying with carbon materials helped increase the electrical conductivity and enlarge the surface area.[85] Adding another narrow bandgap material such as MoS_2[86] proved to be a good choice for improving the utilization of visible light by taking advantages of the synergetic effect of MoS_2 and CdS.

3.1.2. 1D TiO_2

In contrast, 1D TiO_2 exhibited superior electron transportation capability due to the excellent vectorial path for efficient interfacial charge transfer. Thus, CdS-modified TiO_2 nanotube array,[87] nanofibers,[88] nanobelts,[89] and nanorod arrays[90] exhibited excellent photodegradation performance.

3.1.3. 2D TiO_2

Two different electron transfer processes were formed by selectively depositing CdS NPs on h^+-rich (001) or e^--rich (101) facets of TiO_2 nanosheets, which greatly affected the photocatalytic efficiency and anticorrosion of CdS. Specifically, a typical type II alignment and direct Z-scheme system were formed in (001) TiO_2/CdS/CDots and (101) TiO_2/CdS/CDots, respectively, the inner electric field generated by the p-n heterojunction would drive away the e–h pairs spatially, resulting in the oxidation and reduction reactions separately occurred in two different regions. Unfortunately, this type II charge transfer process would seriously weaken the redox ability of CdS/TiO_2 and lead to severe photocorrosion of CdS. While the direct Z-scheme system would realize the spatial separation of e–h pairs and ensure strong redox ability as well as preventing corrosion of CdS.

3.2. Water Splitting and H_2 Generation

A brief review on CdS/TiO_2 composites applied in photocatalytic H_2 generation has been published by Zhao et al. in 2015.[91] Here we only review the latest progress on CdS/TiO_2 in PEC within the five years and the results are shown in **Table 3**.

3.2.1. CdS/TiO_2 Electrodes

The type II alignment of CdS/TiO_2 was reported to effectively separate the e–h pairs and resulted in enhanced PEC

© 2019 WILEY-VCH Verlag GmbH & Co. KGaA, Weinheim

Table 3. PEC performance of CdS/TiO_2-based heterostructures.

Photocatalysts	Loading method	Light source	Surface area	Amount	Sacrificial reagent	Performance (H_2 yield; J_{ph};[a]; AQE;[b] IPCE;[c] EQE[d])	Ref.
CdS NPs/TiO_2 NPs	One-pot combustion technique	Visible light (800–900 W m^{-2})	152 m^2 g^{-1}	100 mg	1 M Na_2S + 1 M Na_2SO_3	11.8 mmol h^{-1} g^{-1}	[84b]
CdS QDs/Ti^{3+}-TiO_2 nanobelts	CBD	300 W Xe lamp, $\lambda \geq 420$ nm	–	100 mg	20%CH_3OH-H_2OH + 0.5 wt% H_2PtCl_6	4800 µmol h^{-1} g^{-1}	[89b]
CdS NPs/TiO_2 nanosheets	SILAR	350 W Xe lamp	84 m^2 g^{-1}	0.05 g	25%CH_3OH-H_2O	1024 µmol h^{-1} g^{-1}	[92c]
CdS/TiO_2 porous hollow microspheres	Salt-assisted aerosol decomposition	Visible light	72.4 m^2 g^{-1}	50 mg + 1.5% Ru	0.35 M Na_2S + 0.25 M K_2SO_3	19.920 mmol h^{-1} g^{-1}	[92a]
CdS NPs/porous TiO_2 monolith	Template sol-gel and hydrothermal methods	300 W Xe lamp	65.96 m^2 g^{-1}	50 mg	0.35 M Na_2S + 0.25 M Na_2SO_3	1048.7 µmol h^{-1} g^{-1}	[92b]
CdS nanowires@TiO_2 ultrathin layer	Hydrothermal	150 W Xe lamp, AM1.5G filter	–	1.0 × 1.0 cm^2	0.5 M Na_2S + 0.5 M Na_2SO_3	J_{ph} = 1.8 mA cm^{-2} at 0 V vs RHE; 47.5 mmol h^{-1} g^{-1}	[92e]
CdS NPs@TiO_2 NPs	Hydrothermal	White light (100 mW cm^{-2})	–	–	0.25 M Na_2S + 0.35 M Na_2SO_3	$IPCE_{450\ nm}$ = 2.4%	[92d]
CdS QDs/TiO_2 hybrid nanostructures	SILAR	Simulated sunlight (AM1.5, 100 mW cm^{-2})	–	–	0.25 M Na_2S + 0.35 M Na_2SO_3 + 0.1 M KCl	J_{ph} = 2.31 mA cm^{-2} at 0 V vs Ag/AgCl; IPCE = 25%	[94a]
CdS thin layer/TiO_2 nanotube arrays	ALD	300–650 nm	52 cm^2 cm^{-2}	–	0.1 M Na_2SO_4	$IPCE_{450\ nm}$ > 60%	[94b]
TiO_2 nanorod film/ CdS NPs	Phase transformation	150 W Xe lamp ($\lambda \geq 400$ nm)	–	1.0 × 1.0 cm^2	0.25 M Na_2S + 0.35 M Na_2SO_3	J_{ph} = 9.65 mA cm^{-2} at 0.8 V vs RHE; 93.8 µmol h^{-1} cm^{-2}	[94c]
CdS nanoflower/TiO_2 nanotube arrays	Hydrothermal	Solar simulator (100 mW cm^{-2})	–		0.1 M Na_2S + 0.02 M Na_2SO_3 (pH = 12.7)	≈80 µmol h^{-1} cm^{-2}	[94d]
CdS nanoflower/TiO_2 nanorod arrays	Hydrothermal	Solar simulator (100 mW cm^{-2})	–	1 cm^2	0.1 M Na_2S + 0.02 M Na_2SO_3 (pH = 11.5)	≈336 µmol h^{-1} cm^{-2}	[94f]
3DOM TiO_2/Au NPs/ CdS NPs	CBD	Visible light (420–780 nm); UV–vis light (250–780 nm)	66 m^2 g^{-1}	0.1 g	0.1 M Na_2S + 0.1 M Na_2SO_3	1.81 mmol h^{-1} g^{-1} (visible); 2.28 mmol h^{-1} g^{-1} (UV–vis)	[96a]
3DOM TiO_2/Au NPs/ CdS NPs	CBD	Visible light ($\lambda \geq 420$ nm, 158 mW cm^{-2})	28 m^2 g^{-1}	0.1 g	0.1 M Na_2S + 0.1 M Na_2SO_3	3.50 mmol h^{-1} g^{-1}	[96c]
CdS nanowire/Ag NPs/ TiO_2 NPs	Hydrothermal	300 W Xe lamp	–	100 mg	10 mL of TEOA + 5 mg of $(NH_4)_2PtCl_6$ in 90 mL DI water.	1.91 mmol h^{-1} g^{-1}	[100]
MoS_2 NPs/CdS NPs/TiO_2 nanofibers	Photodeposition	300 W Xe lamp, $\lambda \geq 420$ nm	46.27 m^2 g^{-1}	10 mg	10 v% lactic acid	28 mmol h^{-1} g^{-1}, AQE (420 nm) = 19.3%	[106b]
$Ti_3C_2(TiO_2)$ NPs@CdS NPs/MoS_2 NPs	Hydrothermal	300 W Xe lamp, $\lambda > 420$ nm	–	10 mg	0.5 M Na_2SO_4	8.47 mmol h^{-1} g^{-1}	[106a]
TiO_2 nanorod arrays/CdS QDs/Cu_2S QDs	SILAR	300 W Xe lamp (100 mW cm^{-2})	–	≈1 cm^2	0.35 M Na_2S + 0.25 M Na_2SO_3	J_{ph} = 13.65 mA cm^{-2} at 0 V vs Ag/AgCl	[108]
TiO_2 nanorod arrays/ CdS QDs	CBD	Simulated sunlight, 300 W Xe lamp	–	0.8–1.0 cm^2	0.25 M Na_2S + 0.35 M Na_2SO_3	J_{ph} = 6.8 mA cm^{-2} at 1.0 V vs RHE; 39.2 µmol h^{-1} cm^{-2}	[95]
g-C_3N_4 nanosheets@TiO_2-CdS QDs	Hydrothermal	4 LED lamps (3 W, 420 nm)	73.2 m^2 g^{-1}	50 mg	0.5 M Na_2S + 0.5 M Na_2SO_3	1504 µmol h^{-1} g^{-1}; EQE (420 nm) = 11.9%	[109b]
TiO_2 nanorods/GQD/ CdS QDs	SILAR	500 W Xe lamp (≈90 mW cm^{-2})	–	–	0.1 M Na_2S	J_{ph} = 2.8 mA cm^{-2} at 0 V vs Ag/AgCl	[112]
CdS QDs/SiO_2 NPs/ TiO_2 NPs	SILAR	300 W Xe lamp (100 mW cm^{-2})	–	1 × 1 cm^2	0.5 M KOH	J_{ph} = 4.6 mA cm^{-2} at 0 V vs Ag/AgCl;	[104]

© 2019 WILEY-VCH Verlag GmbH & Co. KGaA, Weinheim

Table 3. Continued.

Photocatalysts	Loading method	Light source	Surface area	Amount	Sacrificial reagent	Performance (H_2 yield; J_{ph};[a]; AQE;[b] IPCE;[c] EQE[d])	Ref.
SnO_2 nanosheet arrays/TiO_2 layer/CdS QDs	SILAR	300 W Xe lamp (100 mW cm^{-2})	–	1.5×4 cm^2	0.25 M Na_2S + 0.35 M Na_2SO_3	J_{ph} = 4.7 mA cm^{-2} at 0.9 V vs RHE; 7.6 μmol mA^{-1} h^{-1}	[103a]
CdS QDs/ZnO nanorods/TiO_2 nanosheets	SILAR	500 W Xe lamp (100 mW cm^{-2})	–	–	0.25 M Na_2S + 0.35 M Na_2SO_3	J_{ph} = 12.1 mA cm^{-2} at 0 V vs RHE	[105]
NiS NPs/CdS NPs/TiO_2 nanosheets	One-step sulfurization	300 W Xe lamp, $\lambda > 420$ nm	–	50 mg	0.25 M Na_2S + 0.35 M Na_2SO_3	2149.15 μmol h^{-1} g^{-1}	[107]
TiO_2 nanotube arrays/PbS QDs/CdS QDs	Sonication-assisted SILAR	White light (λ_{main} = 553 nm, 5.9 mW cm^{-2})	–	–	0.1 M Na_2S + 0.2 M Na_2SO_3	J_{ph} = 0.87 mA cm^{-2} at 0 V vs SCE	[94e]
TiO_2 nanorod arrays@CdS/CdSe shell layer	CBD	150 W Xe lamp (100 mW cm^{-2})		0.25 cm^2	0.3 M Na_2S + 0.2 M Na_2SO_3	J_{ph} > 35 mA cm^{-2} at 0.3 V vs SCE	[111a]
Hollow sphere CdS@/TiO_2 layer/Ni_2P NPs	Template CBD	Xe lamp with AM1.5G filter	46.5 m^2 g^{-1}	10 mg	0.1 M Na_2S + 0.1 M Na_2SO_3	13.912 mmol h^{-1} g^{-1}	[110]

[a]J_{ph}: photocurrent density; [b]AQE: apparent quantum efficiency; [c]IPCE: incident photon to current conversion efficiency; [d]EQE: external quantum efficiency.

performance.[84b,92] In the H_2 generation process, due to the reduction of S^{2-}, sulfide sacrificial reagents are needed to reduce the photocorrosion of CdS, which implies that no oxygen generated for the CdS photoanode. Thus, considering the photocorrosion of CdS under light irradiation, some unique structural morphology should be considered. For example, Han et al. fabricated a novel core–shell CdS/TiO_2 nanostructure, and demonstrated that the thickness of TiO_2 shell played an important role in the charge transfer process (**Figure 6**a,b).[92d] However, it was difficult to recycle the powdery photocatalyst, which greatly limited the further application in H_2 generation. Liu et al.[92e] constructed a novel PEC H_2 fuel cell by using a transparent core–shell CdS@TiO_2 nanotextile on FTO substrate as the photoanode (Figure 6c). The coating of an ultrathin amorphous TiO_2 layer (3.5 nm) not only effectively suppressed the active photocorrosion of CdS but also created a tunneling barrier for photogenerated holes to be trapped by sacrificial reagent to promote efficient charge transfer. The results demonstrated that under continuous illumination at 0 V versus RHE, an amount of 4.45 mL of H_2 gas was generated, consistent with the expected amount of 4.46 mL, corresponding to a Faradaic efficiency close to 100% (Figure 6d). Surprisingly, the photocurrent showed only 9% decay after 9 h, suggesting its profoundly enhanced PEC stability.

CdS QDs[89b,93] have been commonly used as photosensitizers to form composites with TiO_2 due to their high absorption cross-section and size-dependent optical properties.[168,173–175] 1D TiO_2 nanostructures in the form of nanotube arrays, nanorods, and nanobelts are also commonly used as substrates to construct CdS/TiO_2 photoanodes.[89b,93c,94] Interestingly, Chen et al.[95] intentionally added an anatase seed layer into the interface between rutile TiO_2 nanorods and FTO substrate to form anatase/rutile homojunction, and found that 34% enhancement in H_2 generation efficiency was achieved accompanied by improved chemical stability. The reason was possibly because the band alignment of the anatase/rutile junction increased the energy difference (ΔG) between the defect states of CdS and CB of TiO_2, which provided an enhanced driving force of interfacial electron transfer, promoting more efficient electron collection efficiency.

3.2.2. Metal Decorated Ternary Composites

To further broaden the light absorption ability, plasmonic metal nanostructures (Au[96] or Pt[97]) are thoroughly investigated to decorate the CdS/TiO_2 for enhanced PEC performance. For TiO_2-Au-CdS ternary composite, there are two different internal charge transfer processes upon visible and UV–vis light irradiation (**Figure 7**a).[96a] Under visible light irradiation, only CdS can be excited to generate e–h pairs, the electrons of CdS will be transferred to the CB of TiO_2 via Au NPs, while holes accumulate at the VB of CdS to keep the electrons and holes spatially separated. H^+ is reduced on the surface of TiO_2 and oxidation reaction occurs on the surface of CdS. The internal electron transfer process could be highly accelerated in the presence of Au NPs, leading to a higher H_2 generation rate than the Au-CdS sample.[96c] While upon UV–vis light irradiation, both TiO_2 and CdS supply the e–h pairs, and the photogenerated electrons of TiO_2 would move to the VB of CdS through an Au core, and then recombine with holes of the CdS, which departs the electrons and holes spatially, forming the typical electron-transfer pathway of Z-scheme photocatalyst.[92c,98] The reduction and oxidation reactions would proceed on the CB of CdS and VB of TiO_2, respectively. Referring to Z-scheme type photocatalysts, Fan group designed several CdS/Au/TiO_2 ternary heterostructures using biomass templates (wood, butterfly wing, leaf) to grow hierarchical porous architectures ranging from macro-, micro-, to nanoscales,[99] which enhanced the overall light harvesting and offered abundant absorption and reaction sites for the catalytic reactions. The incorporated photocatalytic modules—CdS(shell)/Au(core)/TiO_2

© 2019 WILEY-VCH Verlag GmbH & Co. KGaA, Weinheim

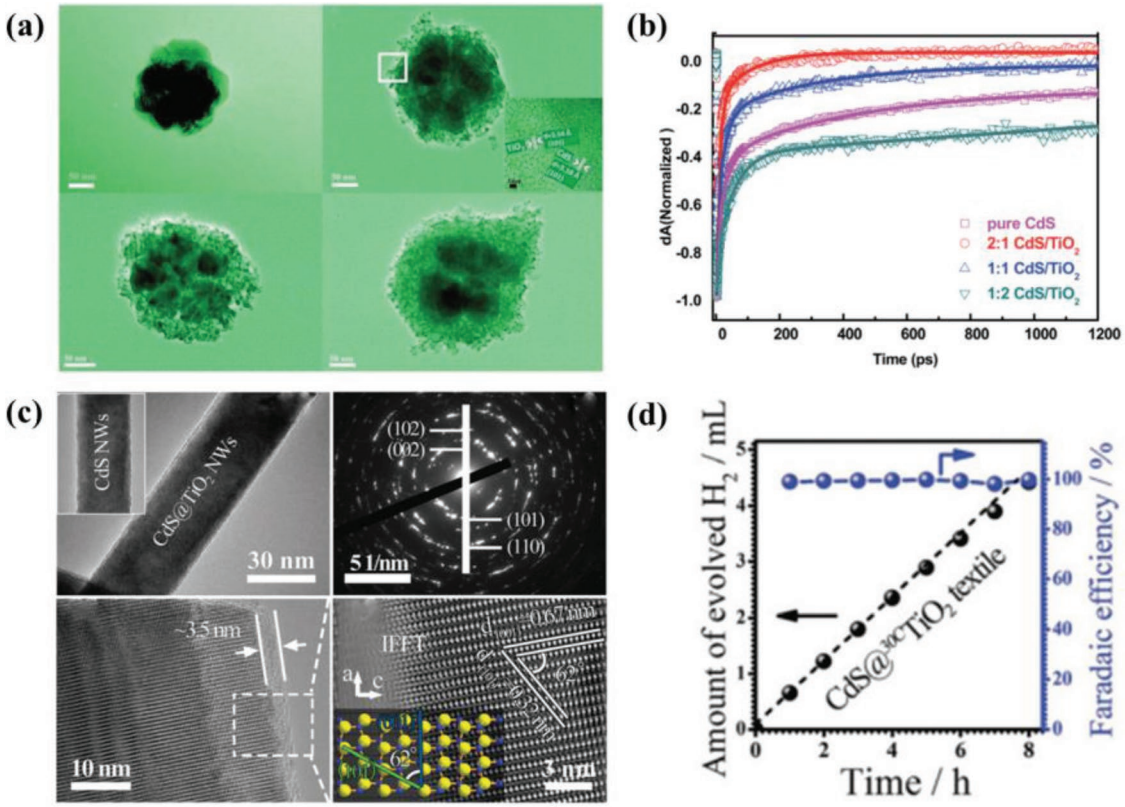

Figure 6. a) TEM images of samples: pure CdS, 2:1 CdS/TiO_2, 1:1 CdS/TiO_2, and 1:2 CdS/TiO_2 and b) their transient bleach kinetics (λ_{pump} = 400 nm). The shorter photoexcited electron lifetime means better electron transfer from CdS to TiO_2. Reproduced with permission.[92d] Copyright 2015, Royal Society of Chemistry. c) Structural morphology, and d) the Faradaic efficiencies and trace H_2 amounts from the CdS@TiO_2 textile electrodes. The black dashed lines and spheres are the theoretical and measured amounts of evolved H_2, respectively. Reproduced with permission.[92e] Copyright 2017, Royal Society of Chemistry.

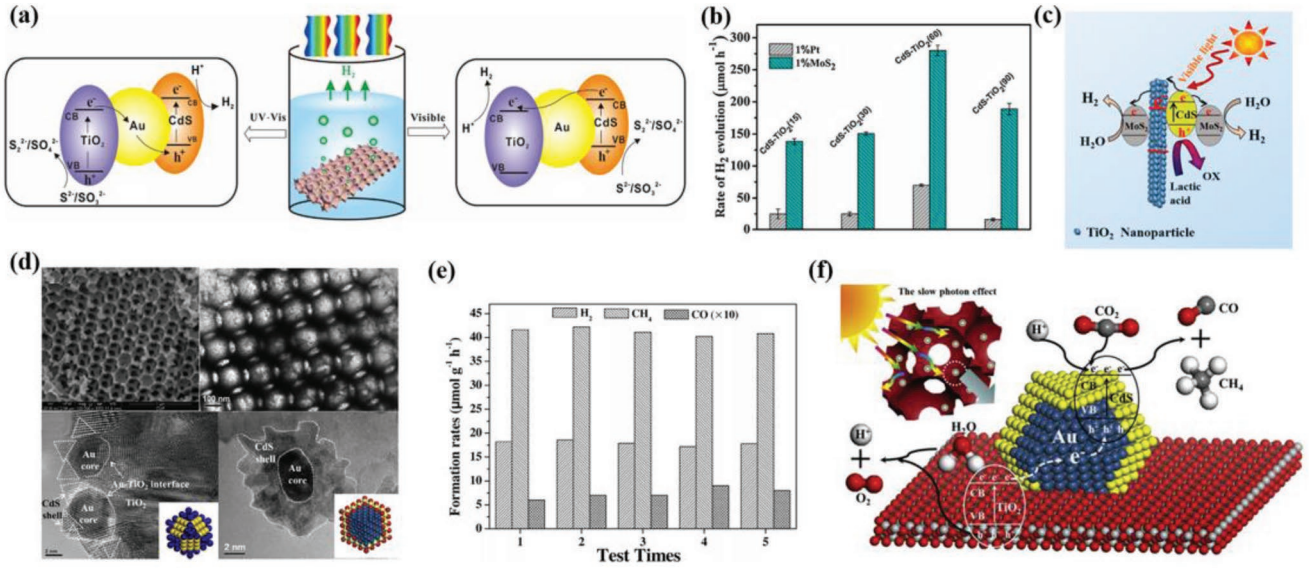

Figure 7. a) Transfer routes of photogenerated electrons and holes in the TiO_2-Au-CdS ternary composites under UV–vis (Z-scheme type) and visible light irradiation (Type II heterojunction). Reproduced with permission.[96a] Copyright 2016, Elsevier. b) Photocatalytic H_2 evolution rate over CdS-TiO_2 nanofibers loaded with 1% MoS_2 or 1% Pt under visible light illumination, and c) the working mechanism for MoS_2/CdS-TiO_2 nanocomposites. Reproduced with permission.[106b] Copyright 2017, Elsevier. d) SEM, TEM, and HRTEM images of Au@CdS/TiO_2 catalysts. e) Stability study on the formation rate of H_2, CH_4, and CO over Au@CdS/TiO_2 catalyst for five test cycles. The values are magnified to ten times for CO formation rate. f) Mechanism for the photoreduction of CO_2 with H_2O over Au@CdS/TiO_2 catalysts. Reproduced with permission.[115b] Copyright 2015, Elsevier.

© 2019 WILEY-VCH Verlag GmbH & Co. KGaA, Weinheim

heterostructures—demonstrated increased visible light catalytic performance and extended electron–hole lifetimes by mimicking Z scheme reactions in photosynthesis. Similar results could be found in the Z-scheme CdS-Ag-TiO_2 ternary photocatalyst reported by Zhao et al.[100]

In contrast to Au-decorated CdS/TiO_2 composites, platinized CdS/TiO_2 hybrids exhibited different electron transfer path upon visible light irradiation. The photogenerated electrons in the CB of CdS transfer to that of TiO_2, and then migrate to Pt NPs to reduce H^+, finally to produce H_2. The Pt NPs on TiO_2 nanostructures produce a Schottky barrier to facilitate the electron capture.[101] Meanwhile, the holes accumulated at the VB of CdS are responsible for the oxidative decomposition of sacrificial agents. Moreover, in order to reduce the waste of photogenerated electrons, Ma et al.[102] prepared a Z-scheme photocatalytic system based on Pt@CdS nanorods and TiO_2 assisted by DNA and benzoquinone, which showed a significant improvement in H_2 production compared to either single photocatalyst or unassembled, dispersed catalyst mixtures.

3.2.3. Other CdS/TiO_2-Based Ternary Composites

Ternary composites, such as metal oxide (SnO_2,[103] SiO_2,[104] ZnO[105]), metal sulfides (MoS_2,[64b,106] NiS,[107] Cu_2S,[108] PbS,[94e]), carbon nitride,[109] and others (Ni_2P,[110] CdSe,[111]) are also explored to further enhance the e–h separation efficiency. Qin et al.[106b] proposed a ternary MoS_2/CdS-TiO_2 photocatalyst by using TiO_2 nanofibers with high surface area as support to photodeposit both MoS_2 and CdS NPs. The prepared 1%MoS_2/CdS-TiO_2 photocatalysts exhibited much higher H_2 generation activity in lactic acid solution (28 mmol h^{-1} g^{-1}) compared with 1%MoS_2/CdS-P25 composites and 1%Pt/CdS-TiO_2 nanofibers under visible light illumination ($\lambda \geq 420$ nm) (Figure 7b). Upon illumination, the photogenerated holes from CdS were consumed by sacrificial regents and net photogenerated electrons were produced. The photogenerated electrons could not only directly transfer to the HER active sites on MoS_2 due to the intimate interfacial contacts but also indirectly migrated to MoS_2 via TiO_2 as the bridge because of the type II energy band structures, leading to more efficient charge separation and therefore improved the catalytic activity (Figure 7c). Pathak et al.[112] systematically examined the influence of various carbon allotropes including graphene quantum dots (GQDs), reduced graphene oxides (RGO), carbon nanotubes, and fullerene as an interfacial layer between CdS and TiO_2 on the PEC performance, and found that all the carbon allotropes showed an increased response, while the presence of GQDs resulted in the highest improvement.

Besides, the optical and electronic properties of CdS can be adjusted by defect engineering. For example, Ma et al.[113] found that suitable Zn doping can improve the electrical conductivity of CdS film, which exhibited great potential in the application of optoelectronic devices. Liu et al.[94c] reported that CdS layer with fewer grain boundaries showed higher visible-light PEC activity than that with numerous grain boundaries. Gong et al.[114] fixed surface defects of CdS by a TiO_2 layer to reduce surface carrier's recombination. The TiO_2 layer also acted as a hole-blocking layer to reflect photogenerated holes to improve charge separation and a protective layer to avoid the corrosion of CdS.

3.3. Photocatalytic CO_2 Conversion

CdS/TiO_2 composite has also been used in the field of photocatalytic CO_2 reduction.[115] In CdS/TiO_2, the holes at the VB of CdS can react with water molecules to generate hydrogen ions, while the electrons at the CB of TiO_2 can reduce CO_2 into energy fuels such as CH_4, CO, CH_3OH, etc. For instance, Wei et al.[115b] synthesized a unique ternary composite (Au@CdS/TiO_2 catalysts) with core–shell structured Au@CdS NPs well dispersed on inverse opal TiO_2 by the gas bubbling-assisted membrane reduction precipitation method (Figure 7d–f). The obtained photocatalyst showed a high formation rate of CH_4 (41.6 μmol g^{-1} h^{-1}) with good stability, and its selectivity to CH_4 production by CO_2 reduction was 98.6%. The slow photon effect of inverse opal structure with moderate macropore sizes can enhance the light harvesting efficiency. And the all-solid-state Z-scheme system with CdS(shell)-Au(core)-TiO_2(support) nanojunction was favorable for the separation of photogenerated e–h due to the vectorial electron transfer of $TiO_2 \rightarrow Au \rightarrow CdS$. Li et al.[115a] prepared CdS-modified TiO_2 nanotubes and obtained high formation rate of methanol (≈30 μmol g^{-1} h^{-1}), which was less than that of Bi_2S_3-modified TiO_2 nanotubes.

3.4. QDSCs

There are various reports on solar cells based on TiO_2 electrodes sensitizing with CdS QDs in the past years.[116] In order to efficiently control the size and thickness of CdS QDs, Chen et al.[117] developed a polymer-assisted layer-by-layer adsorption and reaction method, and the CdS/TiO_2-based solar cell exhibited a PCE up to 2.944% (7 cycles), higher than that prepared with 14 cycles of traditional SILAR deposition method. Further experiments[118] demonstrated that the maximum cell efficiency can reach to 4.15% using the TiO_2 nanotubular arrays as the matrix structure of QDSC, which was higher than that of TiO_2 nanorod arrays electrode (3.57%).[119] In order to harvest more visible light, CdSe and PbS QDs were used as the cosensitizers to enhance the cell performance (6%).[116d] Recently, passivation layer was introduced between CdS QDS and TiO_2 to reduce the recombination rate from TiO_2 to the electrolyte, resulting in increased charge collection efficiency.[120]

3.5. Drawbacks of CdS/TiO_2

Cadmium is a well-known toxic heavy metal, which is harmful to human body and environment, thus making the utilization of CdS-based catalysts less promising. Besides, severe photocorrosion of CdS is also a big drawback for PEC-related applications.

4. CuS/TiO_2 Heterostructures

4.1. Basic Properties

Environmentally friendly, p-type semiconducting copper sulfide (Cu_xS) with Cu vacancies within the lattice are attractive. There

© 2019 WILEY-VCH Verlag GmbH & Co. KGaA, Weinheim

Table 4. Photodegradation and hydrogen evolution performance of CuS/TiO_2-based composites.

Photocatalysts	Loading method	Light source	Surface area	Amount	Organic dyes/ sacrificial reagent	Performance (Degradation ratio%; H_2 yield; AQY[a])	Ref.
CuS QDs/TiO_2 nanotubes	Stepwise chemical method	450 W Hg lamp ($\lambda > 600$ nm)	–	25 mg	MG (100 mL, 0.3×10^{-3} M)	≈80%, 120 min	[121c]
CuS NPs/TiO_2 nanofibers	Hydrothermal	25 W wideband lamp ($\lambda_{main} = 365$ nm)	36.85 $m^2 g^{-1}$	100 mg	MB (100 mL, 10 mg L^{-1})	≈79%, 180 min	[123b]
CuS-graphene oxide/TiO_2 NPs	Sol-gel reaction	Visible light (8 W)	13.29 $m^2 g^{-1}$		MB (100 mL, 50 mg L^{-1})	≈45%, 120 min	[127c]
CuS-CdS NPs/TiO_2 NPs	Hydrothermal	400 W halogen lamp	74 $m^2 g^{-1}$	0.1 g	AO 7 (100 mL, 5 mg L^{-1})	100%, 40 min	[127a]
CuS nanoflowers/TiO_2 NPs	Element-direct-reaction route	125 W Hg lamp ($\lambda = 365$ nm)	–	–	MB or 4-CP (60 mL, 20 mg L^{-1})	MB: >60%, 90 min 4-CP: 87%, 150 min	[123a]
CuS NPs/TiO_2:Fe nanotubes	SILAR	Sunlight irradiation (≈900 W m^{-2})	1100 $m^2 g^{-1}$	50 mg	MG or naphthol green B (50 mL, 5×10^{-6} M)	Malachite green: >70% in 2.5 h at pH = 5 and 7; naphthol green B: 100% at pH = 7; >90% at pH = 9 in 2.5 h	[127b]
TiO_2 microsphere@CuS NPs	Bifunctional linker-assisted assembly	300 W Xe lamp ($\lambda > 420$ nm)	–	100 mg	MB (250 mL, 10 mg L^{-1})	≈90%, 180 min	[126]
CuS NPs/TiO_2 NPs	Hydrothermal	500 W Xe lamp	–	50 mg	50%CH_3OH-H_2O	11.4 mmol $h^{-1} g^{-1}$	[128a]
CuS nanoflakes/TiO_2 nanospindles	Chemical precipitation	300 W Xe lamp ($\lambda > 420$ nm)	35 $m^2 g^{-1}$	50 mg	0.35 M Na_2S + 0.25 M Na_2SO_3	1262 μmol $h^{-1} g^{-1}$	[128c]
CuS NPs@TiO_2 NPs	Hydrothermal	Three UV-lamp: 6 W cm^{-2}, 356 nm	17.88 $m^2 g^{-1}$	500 mg	50%CH_3OH-H_2O	380 μmol $h^{-1} g^{-1}$ at pH = 7; 1.6 mmol $h^{-1} g^{-1}$ at pH = 11	[128b]
CuS NPs/NiS NPs/TiO_2 NPs	Hydrothermal	500 W Xe lamp	48.86 $m^2 g^{-1}$	50 mg	50%CH_3OH-H_2O	16 mmol $h^{-1} g^{-1}$	[129]
CuS nanoflowers/TiO_2 NPs/Pt NPs	Hydrothermal	400 W Xe lamp ($\lambda > 395$ nm)	15.87 $m^2 g^{-1}$	20 mg	0.1 M Na_2S + 0.1 M Na_2SO_3	746 μmol $h^{-1} g^{-1}$, AQY = 1.55%	[130]

[a]AQY: apparent quantum yield.

are five stable phases of Cu_xS ($1 \leq x \leq 2$): analite ($Cu_{1.75}S$), digenite ($Cu_{1.8}S$), djurleite ($Cu_{1.95}S$), chalcocite (Cu_2S) (Cu-rich), and covellite (CuS) (copper deficient).[121] The energy bandgaps of Cu_xS are 1.2, 1.5, and 2.0 eV for $x = 2$, 1.8, and 1, respectively, depending on the average oxidation states of copper.[121b] These phases of $Cu_{2-x}S$ have been regarded as ideal candidates for solar cells, gas sensors, catalysts, lithium ion batteries, etc.[73,122] Among them, owing to its long-term stability, excellent conductivity, environmental benignity, and suitable energy levels, the covellite phase of CuS becomes one of the desirable candidates for optoelectronic devices. The energy bandgap of CuS (E_g = 2.0 eV) matches well with the visible light region of solar spectrum and offers a potential platform to tailor the light absorption in CuS/TiO_2 heterojunctions. The integration of CuS nanostructure also leads to a type-II alignment of TiO_2/CuS (Scheme 1), which helps harvest more light and enhances the charge separation. **Table 4** summarizes the photocatalytic degradation and hydrogen evolution performance of CuS/TiO_2 composites.

4.2. Photodegradation of Organic Pollutants

4.2.1. CuS/TiO_2 Heterostructures

The type-II CuS/TiO_2 heterostructure shows excellent photocatalytic degradation performance,[123] and the proposed operative mechanism is very similar to that of CdS/TiO_2 photocatalysts discussed in Section 3.1.

CuS NPs: Ratanatawanate et al.[121c] reported a stepwise chemical method to functionalize TiO_2 nanotubes with CuS QDs (3–4 nm in diameter) using cysteine linkers owing to three reactive centers: a thiol group (−SH), an amine ($-NH_2$), and a carboxylic acid (−COOH),[123d] which was also applicable to grow other QDs materials such as PbS QDs, by using thiolactic acid as a linker.[124] The prepared CuS/TiO_2 photocatalyst degraded malachite green (MG) effectively under visible light illumination. Li et al.[125] proposed an ultrasonic-assisted hydrothermal method to provide a uniform dispersion of CuS NPs on TiO_2 nanotubes with increased CuS amount, which was promising for the construction of a good p-n heterojunction to make easier separation of photogenerated e–h pairs.

CuS Nanofilms: In contrast to coupling with CuS NPs, Khanchandani et al.[123c] found that the visible light photocatalytic efficiency of TiO_2/CuS core/shell nanostructure (≈90%) was much higher than that of TiO_2/CuS composite (≈58%) due to the specific design of core–shell geometry maximizing the interfacial contact between TiO_2 and CuS and enabling effective charge separation by confining electrons mainly in one component (core) and holes in the other (shell) (**Figure 8**a,b). The similar results were found by Ma et al. recently.[126] They developed a bifunctional linker-assisted assembly method to

© 2019 WILEY-VCH Verlag GmbH & Co. KGaA, Weinheim

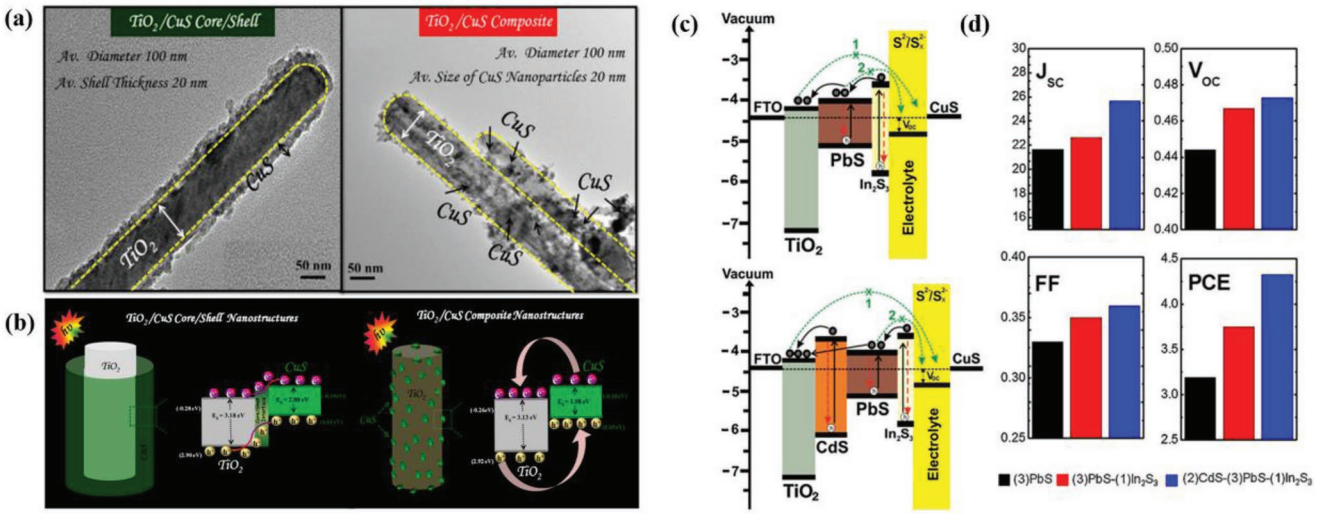

Figure 8. a) TEM images and b) photogenerated charge transfer processes under visible light irradiation of TiO_2/CuS core/shell and TiO_2/CuS composite nanostructures. Reproduced with permission.[123c] Copyright 2016, American Chemical Society. c) Electronic band structures of In_2S_3/PbS/TiO_2 and In_2S_3/PbS/CdS/TiO_2 photoanodes, and d) the photovoltaic performance. Reproduced with permission.[139] Copyright 2016, Elsevier.

prepare core–shell TiO_2@CuS, which allowed CuS NPs to be anchored tightly on TiO_2 surface with small size, narrow size distribution, and conformal coverage. The core–shell photocatalyst exhibited superior synergistic effect and catalytic activity to the commonly prepared TiO_2/CuS composite counterparts.

4.2.2. Ternary Composites

In order to further enhance the photocatalytic activity, CuS/TiO_2 ternary composites[127] are developed to narrow the optical bandgap, enlarge specific surface area, and facilitate the effective charge separation. Yeon et al.[127c] prepared a CuS-graphene oxide/TiO_2 composite for photocatalytic reaction in which graphene oxide was acted as a photosensitizer to generate electrons as well as capture and transfer electrons generated by CuS and TiO_2 under irradiation, retarding the charge recombination. Interestingly, He et al.[127b] reported that the Fe-doped TiO_2 with an actual Fe content (≈2.93 at%) exhibited a smaller optical bandgap of ≈3.0 eV, which was further narrowed to ≈2.5 eV after the coupling with CuS NPs. The CuS/TiO_2:Fe composite exhibited different degradation activities at different initial pH values of the dye solutions. Due to the Fe doping, the addition of H_2O_2 obviously accelerated the photodegradation process (one magnitude order higher than that in the absence of H_2O_2) following a photo-Fenton-like reaction.

4.3. Photocatalytic Hydrogen Evolution Reactions (HER)

4.3.1. Effect of Loading Amount of CuS

Generally, CuS is investigated as a cocatalyst to effectively promote the charge separation, as it not only offers low activation potentials for H_2 evolution but also serves as active sites. The amount of CuS cocatalyst in the CuS/TiO_2 heterostructure affected the catalytic performance to a large extent.[123a,128] The excessive CuS nanostructures on the surface of TiO_2 would exert a shielding effect on the active sites and decrease the light absorption as well as introducing more recombination centers. While insufficient quantity fails to realize the optimal catalytic activity. Chandra et al.[128c] reported the preparation of CuS/TiO_2 with varying percentage of TiO_2 contents via a simple hydrothermal and solution-based process. Controlling the optimal ratio of CuS/TiO_2 led to the highest photocatalytic H_2 production rate of 1262 μmol h^{-1} g^{-1}, which is 9.7 and 9.3 times higher than that of pristine TiO_2 and CuS nanoflakes under irradiation, respectively.

4.3.2. Effect of pH Values

Im et al.[128b] reported a CuS@TiO_2 core@shell catalyst in which anatase TiO_2 NPs with a high concentration were coated on the surface of rectangular-shaped CuS NPs with 100 nm in length and 60 nm in width. 1.9 mmol of H_2 gas was produced after 10 h (380 μmol h^{-1} g^{-1}) at pH = 7. This value was increased to more than fourfold (8.0 mmol) at pH = 11. In alkali solution, the subsequent reaction occurs: OH^- + hole → •OH in the valence band, thus a large number of OH radicals were generated, resulting in an increase in HER. While in an acidic solution, the amount of H_2 production was decreased due to the formation of SO_4^{2-} ions after reaction. Then the sulfate ions combined with the hydrogen ions generated during the methanol/water photosplitting process, which occurred during the formation of H_2SO_4. Moreover, the pH also affected the zeta potentials and it was found that the surface charges changed from a positive value in an acidic solution to a larger negative value in an alkali solution. The highest absolute values of surface charges at pH = 11 suggested that the colloidal samples were stable with high mobility, which was closely related to the reaction sites over the photocatalyst surface.

© 2019 WILEY-VCH Verlag GmbH & Co. KGaA, Weinheim

4.3.3. Coupling with a Secondary Material

Wang et al.[129] demonstrated that the addition of dual cocatalysts CuS and NiS greatly enhanced the photocatalytic activity because they had lower CBs than TiO_2 and acted as electron acceptors and active sites for H_2 production. Manjunath et al.[130] investigated the photocatalytic hydrogen production using CuS-TiO_2/Pt composite where Pt acted as a sandwich metal between CuS and TiO_2, which was beneficial for effective charge separation. The hydrogen production recorded was 458 μmol h^{-1} g^{-1} for CuS-TiO_2 and 746 μmol h^{-1} g^{-1} for CuS-TiO_2/Pt. The corresponding AQY values were 1.01% and 1.55%.

4.4. Other Applications

CuS/TiO_2-based heterostructures have also been used in the field of biosensors,[131] solar cells,[132] and lithium batteries.[122a] As a clinical indicator of diabetes, the fast and sensitive determination of glucose level in human blood and urine is important. Wang et al.[131] reported a novel and highly sensitive PEC biosensor for glucose detection based on ternary composite Au/CuS/TiO_2. Owing to the remarkable photocatalytic capabilities of TiO_2 and CuS, and the surface plasmonic resonance effect of Au NPs, the ternary composite exhibited excellent catalytic activity, favorable selectivity, good reproducibility, and long-term stability for glucose detection.

Copper sulfide ($Cu_{2-x}S$) with Cu vacancies within the lattice is attractive in the fields of QDSCs and lithium ion batteries. Quan et al.[133] reported a novel $Cu_{1.8}S$/CuS nanoplates structure used as CE to construct high-performance QDSCs. Compared to the Cu_2S electrode, defects in $Cu_{1.8}S$ material increased the electric conductivity and the number of active sites, reduced the charge-transfer resistance at the electrode/electrolyte interface, and resulted in higher PCE performance.

Because of a high theoretical capacity (≈560 mAh g^{-1}), good electrical conductivity (10^{-3} S cm^{-1}), and favorable electrochemical properties with voltage plateaus like Ti-based materials, CuS is attractive in lithium ion batteries. However, the volume expansion and lattice distortion as well as the loss of electroactive species due to the dissolution of sulfide species negatively affect the cyclability. Wang et al.[122a] proposed a self-templating thermolysis strategy, different from traditional wet processing methods, to fabricate $Cu_{2-x}S$ hollow spheres coated with different shells (carbon, TiO_2, MoS_2), by exploiting the thermal decomposition properties of the core (CuS) and the protection provided by the shell. The hollow spheres were then assembled as electrodes and tested in lithium batteries, showing excellent cycling stability.

4.5. Drawbacks of CuS/TiO_2

Owing to the mismatched lattice structures between CuS and TiO_2, it remains a critical challenge to form well-defined CuS/TiO_2 heterojunction as CuS tend to aggregate or randomly reside on bare TiO_2.

5. PbS/TiO_2 Heterostructures

5.1. General Properties

Energetically favorable band alignment is highly desirable between QDs and metal oxides in order to promote efficient interfacial charge transfer and chemical stability. Lead sulfide (PbS) is well known for its small bandgap (E_g = 0.37 eV) and large exciton Bohr radius (20 nm) that leads to extensive quantum effects.[134] Similarly to that of CdS QDs discussed in Section 3, PbS QDs material is another good candidate to efficiently improve photo/electrochemical activity of TiO_2 owing to multiple exciton generation and efficient spatial charge separation to prevent e–h recombination.[135] The photo/electrochemical performance of PbS/TiO_2 composites is shown in **Table 5**.

5.2. QDSCs

PbS QDs are extensively studied as sensitizers in QDSCs due to the fascinating characteristics such as energy-gap tunability, carrier multiplication, and high absorption coefficients. The preparation procedure of PbS QDs and the structure of the corresponding solar cells have a strong influence on the cell performance. By using typical oleic-acid method, Zhong et al.[136] fabricated core–shell PbS/CdS QDs cosensitized mesoporous TiO_2 thin film (9 μm thick) as the photoanode and achieved a PCE of 7.19%. While Zhang et al.[137] prepared CdSe/CdS/PbS using SILAR cosensitized double-layered TiO_2 thin film (18 μm thick) based cells and obtained a PCE of 5.11%. TiO_2 microspheres film was used as the light-blocking layer. Similarly, a SiO_2 microspheres film was added and then removed by chemical etching and left many macropores in the top TiO_2 layer, which served as light scattering centers to improve the light absorption, as well as increasing the loading amount of QDs with good uniformity by SILAR.[138] Consequently, the short-circuit current density (J_{sc}) was improved by 17% (14.9 mA cm^{-2}) and its PCE was enhanced by 19% (3.02%). In order to avoid the electron back-transfer and carrier recombination, In_2S_3 layer was prepared to restrict the carriers recombination at TiO_2/electrolyte and PbS QDs/electrolyte interfaces, whose electronic band structure was displayed in Figure 8c.[139] The In_2S_3 passivation layer also helped reduce the direct contact with the corrosive polysulfide to attain a better photostability. However, the performance improvement was hindered when increasing the In_2S_3 deposition amount which was attributed to the difficulty in hole transfer at QDs/electrolyte interface because the VB edge of In_2S_3 was located at a lower position than that of PbS. The increase in J_{sc} was marginal due to the low absorbance of In_2S_3. Furthermore, CdS was added and the CdS/PbS/In_2S_3/TiO_2 multilayered photoanode with an optimum CdS deposition prior to PbS confirmed an improved PCE value of 4.3% (36% higher than that of PbS standard QDSC), which was credited to the increase in J_{sc} from 21.6 to 25.7 mA cm^{-2} in addition to the increase in open-circuit voltage (V_{OC}) by In_2S_3 layer (Figure 8d).

Dissanayake et al.[140] adjusted the performance of traditional PbS/mesoporous TiO_2 QDSCs through changing the number of TiO_2 layers, and found that TiO_2 triple layer nanostructure based QDSC showed a significantly higher PCE of 4.72%, while

© 2019 WILEY-VCH Verlag GmbH & Co. KGaA, Weinheim

Table 5. Photo/electrochemical performance of PbS/TiO_2, SnS_2/TiO_2, ZnS/TiO_2, Ag_2S/TiO_2, and In_2S_3/TiO_2 based composites.

Photocatalysts	Loading method	Light source	Surface area	Amount	Sacrificial reagent	Performance (H_2 yield; η_{10};[a] Tafel slope, J_0;[b] J_{ph}[c])	Ref.
PbS QDs/Mn-CdS QDs/ TiO_2 NPs	SILAR	AM 1.5G solar simulator	–	≈0.25 cm^2	0.25 M Na_2S + 0.35 M Na_2SO_3	J_{ph} = 22.1 mA cm^{-2} (at 0.6 V vs RHE)	[148]
PbS QDs/Au NPs/ H-TiO_2 nanotube array	Dip-coating	Xe lamp (≈5 A, 100 mW m^{-2})	–	–	0.5 M Na_2SO_4	J_{ph} = 1.149 mA cm^{-2} (at 0.6 V vs RHE)	[149]
PbTe-PbS NPs/TiO_2 nanotube arrays	Electrochemical	–	–	–	0.5 M Na_2S + 0.5 M Na_2SO_3	6.1 mL cm^{-2} h^{-1} at 70 °C and 1.0 V; 95 mV dec^{-1}, $J_0 = 5.07 \times 10^{-2}$ mA cm^{-2}	[150]
PbS QDs/inverse opal TiO_2 architecture	SILAR	White light (420–800 nm, 100 mW cm^{-2})	–	–	1 M KCl	$J_{ph} = 160 \pm 36$ mA cm^{-2} (O_2 evolution)	[151a]
Mesoporous TiO_2 structure/PbS QDs/ CdS QDs	SILAR	450 W Xe lamp (100 mW cm^{-2})	–	–	0.5 M Na_2S + 0.5 M Na_2SO_3	2.5 mL cm^{-2} h^{-1}; J_0 = 6 mA cm^{-2} (at 0.4 V vs RHE)	[151b]
Au-TiO_2 film/PbS QDs/CdS QDs	SILAR	AM 1.5 filter solar simulator	–	–	0.25 M Na_2S + 0.35 M Na_2SO_3	12 ± 0.5 mL h^{-1} cm^{-2}; J_{ph} = 4.3 mA cm^{-2} (at 0 V vs Ag/AgCl)	[151c]
ZnS NPs/TiO_2 nanosphere@g-C_3N_4 nanosheets	Precipitation-hydrothermal	300 W Xe lamp ($\lambda > 400$ nm)	–	10 mg	10% TEOA	422 µmol h^{-1} g^{-1}	[5]
SnS_2 nanosheets/TiO_2 nanobelts	Hydrothermal	–	–	1.2 mg, 1 cm^2	1 M NaOH	η_{10} = 570 mV, 107 mV dec^{-1}	[166a]
SnS_2 nanosheets array/ TiO_2 nanotube arrays	Solvothermal	AM 1.5 filter solar simulator		0.875 cm^2	0.5 M Na_2SO_4	J_{ph} = 1.05 mA cm^{-2} (at 0.5 V vs SCE)	[166b]
SnS_2 nanosheets/ H-TiO_2 nanotube arrays	CVD	AM 1.5 filter solar simulator	–	50 mg	0.5 M Na_2SO_4	J_{ph} = 4.0 mA cm^{-2} (at 1.4 V vs RHE)	[166c]
Ag_2S QDs/TiO_2 nanobelts	Coprecipitation	300 W Xe lamp	–	50 mg	20 v% CH_3OH-H_2O	4.32 mmol h^{-1} g^{-1}	[175]
Graphene oxide/Ag/ Ag_2S NPs/TiO_2 nanorod arrays	SILAR	Visible light irradiation	–	1.5 cm^2	0.1 M KOH	J_{ph} = 6.77 mA cm^{-2} (at 0 V vs Ag/AgCl)	[176b]
Ag-Ag_2S NPs/TiO_2 NPs	In situ sulfidation of Ag	4 LEDs (3 W, 365 nm, 80.0 mW cm^{-2})	–	50 mg	10 v% CH_3OH-H_2O	2382.2 µmol h^{-1} g^{-1}	[176c]
Ag-Ag_2S QDs/TiO_2 nanorod arrays	Wet chemistry method	AM 1.5 filter solar simulator	–	–	0.25 M Na_2S + 0.35 M Na_2SO_3	0.082 mA cm^{-2}	[176d]
Ag_2S NPs/TiO_2 hierarchical spheres	Sequential ionic deposition	300 W Xe lamp (100 mW cm^{-2})	63.486 m^2 g^{-1}	2 mg	10 v% CH_3OH-H_2O	707.6 µmol h^{-1} g^{-1}	[173]
TiO_2 nanorod arrays@ β-In_2S_3 shell layer	Aerosol-assisted CVD	AM 1.5 filter solar simulator	–	8 × 7 mm	0.25 M Na_2S + 0.35 M Na_2SO_3	J_{ph} = 1.42 mA cm^{-2} (0.5 V vs Ag/AgCl)	[184a]
In_2S_3 NPs/Pt-TiO_2 NPs	Refluxing wet-chemical approach	300 W Xe lamp ($\lambda > 420$ nm)	–	300 mg	0.25 M Na_2S + 0.25 M Na_2SO_3	191 µmol g^{-1} h^{-1}	[184b]

[a] $\eta_{(10)}$: overpotential at 10 mA cm^{-2}; [b] J_0: exchange current density; [c] J_{ph}: photocurrent density.

the counterpart with a single layer of TiO_2 NPs showed a PCE of 2.94%. The enhanced efficiency was attributed to improved light harvesting by multiple light scattering in the trilayer TiO_2 photoanode combined with efficient electron transport with less recombination. Lee et al.[141] reported the preparation of a periodically arrayed 2D TiO_2 nanostructure using templating method to provide significantly increased contacts with subsequently deposited PbS QD layer and thus enhancing the optical absorption by regulating the light path through PbS QD layer. It led to an increase in the PCE of up to 70% (5.13%).

Considering the balance of hole diffusion length and loading quantity of QDs, Zhang et al.[142] studied the influence of length, diameter, and areal density of TiO_2 nanorods for the performance of PbS/TiO_2 QDSCs, and found that the short-length, high-density TiO_2 nanorod array and the compact PbS QD thin film based solar cell achieved a PCE of 4.10%, along with V_{oc} = 0.52 V, J_{sc} = 13.56 mA cm^{-2}, and fill factor (FF) of 0.58. The compact PbS QD thin film helped improve the electron injection efficiency from PbS to TiO_2 nanorods and prevent the direct contact of spiro-OMeTAD and TiO_2 nanorods.[143] Zhang et al.[144] reported that the PCE performance was optimized (PCE of 7.80%) by tuning the deposition of PbS, which was achieved by adjusting the concentration ratio of S and Pb sources onto the TiO_2 nanotube array support. Lv et al.[145]

© 2019 WILEY-VCH Verlag GmbH & Co. KGaA, Weinheim

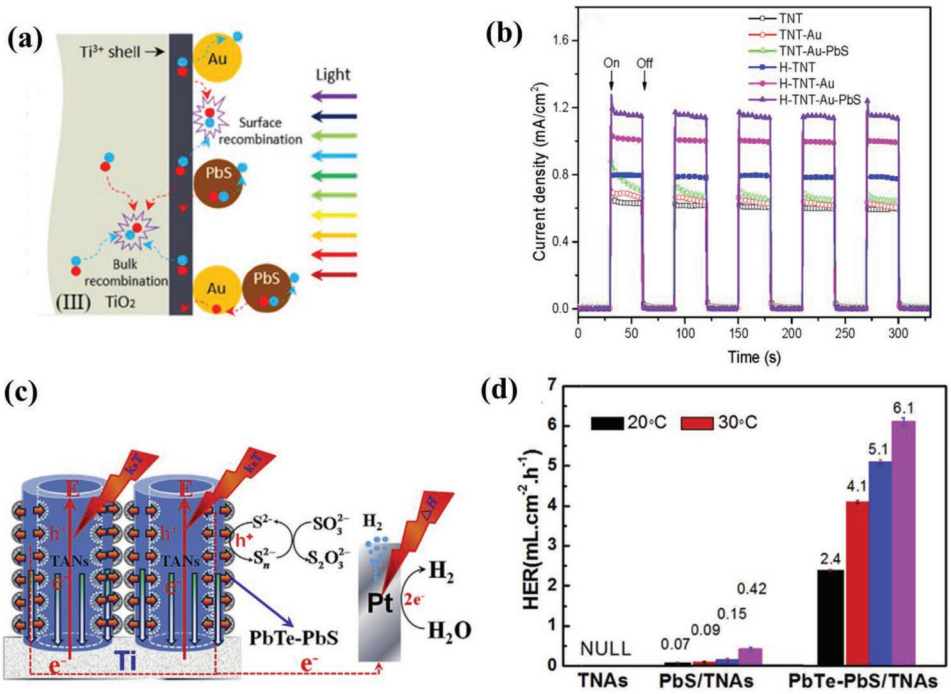

Figure 9. a) Photogenerated e-h pairs transfer and recombination diagram of PbS/Au/H-TiO_2, and b) transient photocurrent responses under visible light illumination at +1 V. Reproduced with permission.[149] Copyright 2017, Elsevier. c) Proposed schematic diagram of hydrogen production processes, and d) hydrogen generation rates of PbTe-PbS/TiO_2 samples at various temperatures. Reproduced with permission.[150] Copyright 2017, Elsevier.

investigated the size effect of PbS QDs and found that the smallest QD size (≈8.4 nm) resulted in the highest PCE (3.45%) when using PbICl as the Pb^{2+} source. Zhou et al.[146] prepared aligned TiO_2 nanorod arrays with 1.9 µm-thick sensitized with PbS QDs and obtained a significantly enhanced FF of 0.51 in contrast to a conventional TiO_2 NP-based device (FF ≈ 0.38). It can be attributed to the outstanding electron transport behavior from QD sensitizers to conducting substrate via the shortest pathway (i.e., through radial direction of nanorod arrays), thereby suppressing charge recombination in solar devices.

The contact state at the heterojunction interfaces greatly influences the interfacial kinetics of the photogenerated charge carriers. Liu et al.[147] revealed that a facile NaOH pretreatment can increase the PbS QDs crystallization degree, minimizing the crystal face mismatch and dangling bond density between PbS QDs and TiO_2. The first principle calculations demonstrated that the PbS QDs and TiO_2 nanotubes interfacial contact was strengthened, and the built-in electric field was induced from TiO_2 (101) towards PbS (111) planes, thus accelerating the charge carrier crossing and effectively reducing the charge recombination at the PbS/TiO_2 interface, and enhancing the overall PEC performance. The peak PCE after five and ten cycles of SILAR deposition demonstrated 19.96% and 29.93% increase than the unpretreated specimen.

5.3. PEC Performance

PbS QDs also endow great potential in enhancing the photo/electrochemical and photocatalytic performance of TiO_2 nanostructures. Kim et al.[148] prepared PbS/Mn-doped CdS QDs modified TiO_2 photoanode with superior light-harvesting capability arising from the improved QD loadings, leading to highly efficient photovoltaic and photocatalytic performances. An unprecedentedly high photocurrent density of 22.1 mA cm^{-2} (at 0.6 V vs RHE) was obtained under simulated solar light for hydrogen production, and the authors claimed that it was the highest value ever reported in QD studies. In order to further facilitate the charge separation efficiency, Du et al.[149] reported a PbS/Au/H-TiO_2 hybrid structure, in which Au NPs served as both light absorber and separation centers (**Figure 9**a,b). By directly interacting with electrolyte, Au NPs could play as main hole-accumulation centers for further reactions under positive potential. In addition, the holes generated on H-TiO_2 were easily transported to Au NPs and further achieved better charge separation. On the other hand, the PbS/Au/H-TiO_2 photoanode exhibited 77.86% enhancement on photocurrent density compared with the PbS/Au/TiO_2 counterpart due to the contribution of the black Ti^{3+} shell layer which exhibited strong visible light absorption. Liu et al.[150] reported a coupled thermoelectricity and electrocatalysis for H_2 production enabling by PbTe-PbS/TiO_2 heterojunction with a gradient p-n-n band configuration (Figure 9c,d). At 70 °C and 1.0 V bath voltage, the system registered 6.1 mL cm^{-2} h^{-1} rate of H_2 generation, consuming electric power of 26.2 kW h kg^{-1}, with an energy efficiency of 88.5% and a heat efficiency of 49.9%. The exchange current density was one order of magnitude higher than that of TiO_2 and PbS/TiO_2, with significantly reduced Tafel slope of 95 mV dec^{-1}, suggesting much better reversibility and higher electrode activity. This work demonstrated a novel pathway to produce chemical energy from low-quality waste heat, benefitting from thermoelectric and electrocatalytic coupling.

© 2019 WILEY-VCH Verlag GmbH & Co. KGaA, Weinheim

To mimicking photosynthesis, the quasi-artificial leaf concept is proposed to provide a platform for solar water splitting with a net positive energy balance.[151] Patra et al.[151c] developed a wireless photochemical cell at no applied potential comprising Au on porous TiO_2 electrode sensitized by PbS and CdS QDs, which demonstrated highly enhanced HER performance at 490 ± 25 μmol h^{-1}, and photocurrent density of 4.3 mA cm^{-2}. The Au NPs used as a plasmonic sensitizer were in physical proximity with TiO_2 along with chalcogenides QDs for better solar light harvesting. QDs that were placed spatially very close to the Au NPs enhanced the localized electric field surrounding the Au NPs and hence an increase in the photocurrent and solar hydrogen was observed by generating more e–h pairs in QDs.

5.4. Other Applications

PbS QDs are also considered to be good candidates in chemical sensors,[152] photocatalysts,[153] and light-emitting diodes.[154] Luo et al.[152b] prepared a photoelectrochemical sensor based on PbS NPs deposited onto TiO_2 nanotube arrays toward Pb ion (Pb^{2+}) detecting based on the generated photocurrents under visible light irradiation. The obtained sensor showed high selectivity against other metal ions, broad linear range from 10^{-8} to10^{-5} M, and low detection limit of 0.39×10^{-9} M (≈0.08 ppb), which was much lower than the standard of Pb^{2+} in drinking water formulated by World Health Organization (WHO).

5.5. Drawbacks of PbS/TiO_2

Despite the rapid developments in the past decades, the device performance of PbS QDSCs still lags the theoretical value. One of notable issues possibly lies in the unsatisfying charge collection and the severe charge recombination for PbS-based photovoltaic devices. The electron injection efficiency is greatly compromised owing to a much lower CB edge of PbS than that of TiO_2.

6. SnS_2/TiO_2 Heterostructures

6.1. General Properties

Tin sulfides, which have several binary compounds such as SnS, Sn_2S_3, Sn_3S_4, Sn_4S_5, and SnS_2, have attracted considerable interest because of their structural diversities.[155] Of these compounds, tin monosulfide (SnS) and tin disulfides (SnS_2) are the most important ones, and have attracted much attention for their interesting properties and potential applications. The n-type semiconductor SnS_2 crystallizes in a layered CdI_2-type structure with a hexagonal primitive unit cell where each layer of Sn atoms is sandwiched between two layers of hexagonally closed-packed S atoms, and the adjacent sulfur layers are connected by the weak van der Waals interactions.[156] The narrow bandgap of crystalline SnS_2 (≈2.1 eV) makes it a hot material with visible-light-responsive ability, promising for photoelectrical and photocatalytic applications.[157] While p-type semiconductor SnS with a smaller direct bandgap of ≈1.32 eV has a strongly distorted NaCl structure, and each Sn atom is coordinated to six S atoms in a highly distorted octahedron.[158] Both SnS_2 and SnS have good oxidative stability and thermal stability in normal temperature. They can also stably exist in acid and neutral environment. According to their electronic property and appropriate matching degree of band potentials with TiO_2, both SnS_2 and SnS could have high photocatalytic performance and are used as excellent materials to form the heterojunction structure with TiO_2.[159]

6.2. Photodegradation Performance

The SnS_2 has much better photostability than CdS. Meanwhile, in contrast to CdS, it favored photocatalytic reduction. The development of SnS_2/TiO_2 heterostructures is critical in large-scale Cr(VI) wastewater treatment by visible-light-driven reduction of aqueous Cr(VI) to less toxic Cr(III).[160] Wang et al.[160c] proposed a novel mesoporous yolk–shell SnS_2/TiO_2 photocatalyst (**Figure 10**a), which also exhibited enhanced photoactivity with excellent durability due to the strong photosensitizing effect of SnS_2 in uniform particles and enhanced light absorption via multiple reflections in yolk–shell chambers and the protection from SnS_2 leaching by TiO_2 shell.

For the photodegradation of organic dyes, in contrast to the traditional n-n SnS_2/TiO_2 heterojunction, Zhang et al.[161] reported a face-to-face n-p-n dual heterojunction comprising anatase TiO_2 nanosheets with coexposed (101) and (001) facets coupled with ultrathin SnS_2 nanosheets, which displayed 47% better in terms of photocatalytic activity than pristine TiO_2/SnS_2 composite. The electron transmission from SnS_2 to TiO_2 was weak, resulting in poor separation efficiency of photogenerated carriers. While in the novel n-p-n dual heterojunction, the photoinduced electrons in the CB of [001] facets would flow into the [101] facets of TiO_2. Therefore, the electrons in the CB of SnS_2 can flow into the [001] facets of TiO_2 to improve the separation efficiency of the photoinduced carriers (Figure 10b). In addition to the strong SnS_2–TiO_2 interaction, large surface area also plays a significant role by offering enhanced mass transfer and light capture, as well as electron transport ability.[162,163] Also, 1D TiO_2 nanostructures are still favored to load SnS_2 considering the vectorial channel for charge transfer.[164] Meanwhile, the photocatalytic performance of the composite can be further improved by forming TiO_2 homojunction with anatase-rutile mixed phase[164a] or adding RGO as cocatalyst.[165]

6.3. Water Splitting Performance

The superior PEC water splitting performance was reported based on SnS_2/TiO_2 heterojunctions (Table 5).[166] Mu et al.[166b] reported a trap-like SnS_2/TiO_2 heterojunction based photoanode demonstrating a photocurrent density of 1.05 mA cm^{-2} and optimal η of 0.73% at 0.5 V (vs SCE) under simulated light illumination, which were 4.6 and 3.8 times higher compared to the pure TiO_2 electrode (0.23 mA cm^{-2} and 0.19%), respectively (Figure 10c–e). The generation rates of H_2 and O_2 were 47.2 and 23.1 μmol cm^{-2} h^{-1}, corresponding to faradaic efficiencies

© 2019 WILEY-VCH Verlag GmbH & Co. KGaA, Weinheim

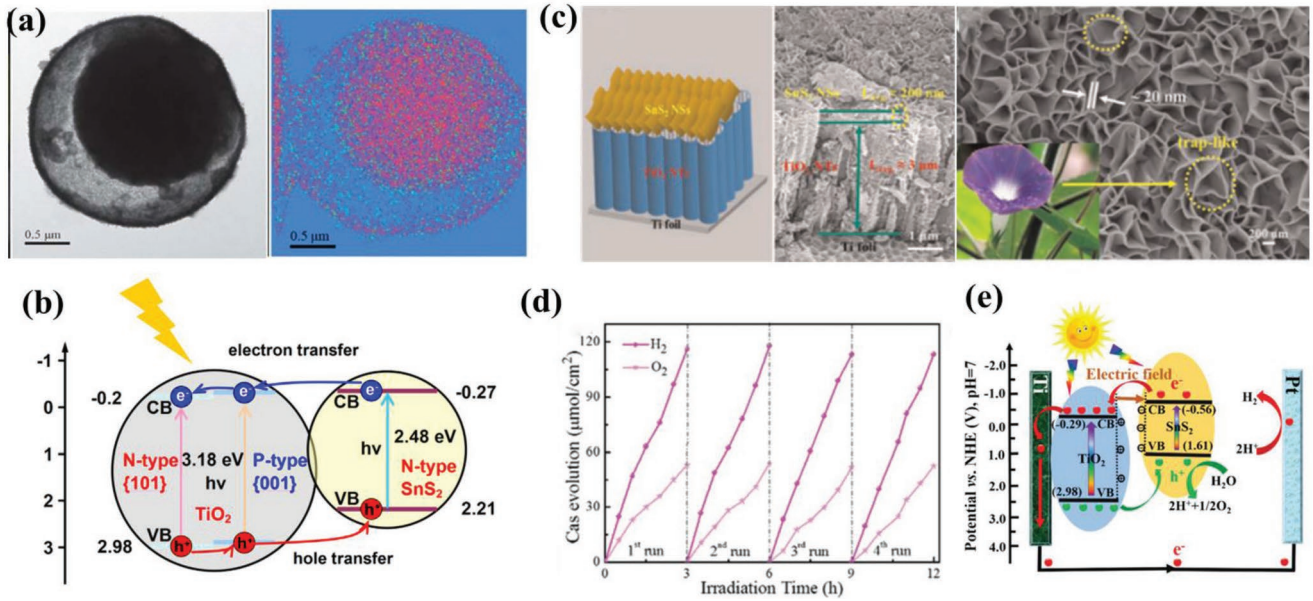

Figure 10. a) TEM images of mesoporous yolk–shell SnS_2/TiO_2 heterostructure. Red and green dots refer to Ti and Sn, respectively. Reproduced with permission.[160c] Copyright 2013, Royal Society of Chemistry. b) Diagram of carrier exchange of SnS_2/TiO_2 n-p-n dual heterojunctions. Reproduced with permission.[161,166a] Copyright 2017, Elsevier. c) SEM images, d) H_2 and O_2 evolution curves at 0.5 V under AM 1.5G for different cycles and e) the diagram of charge carrier separation and transportation of trap-like SnS_2/TiO_2 heterostructure. Reproduced with permission.[166b] Copyright 2018, Royal Society of Chemistry.

of around 80.1% and 78.3%, respectively. They ascribed this improvement to the enhanced light harvesting ability of the trap-like SnS_2 structure, accelerated carrier transportation properties of 1D TiO_2 nanotubes, and facilitated carrier separation of the type-II heterojunction. Lin et al.[166c] further improved the photocurrent density to a value of 4.0 mA cm^{-2} at 1.4 V versus RHE in Na_2SO_4 solution under simulated light illumination by using hydrogen-treated TiO_2 nanotubes (SnS_2/H-TiO_2) (**Figure 11**a,b). They claimed that the hydrogen defects in H-TiO_2 created delocalized electron carriers with Ti 3d character at the bottom of CB, which led to a small bandgap value of 3.18 eV and more negative CB edge (–4.22 eV) while the CB edge values for TiO_2 and SnS_2 were –4.18 and –4.07 eV, respectively. As a result, a transition from type I to type II band alignment at the TiO_2/SnS_2 interface was achieved, facilitating the e–h separation, as well as improving the conductivity (Figure 11c,d).

6.4. Other Applications

SnS_2 is also considered as a promising anode candidate for ion batteries due to its high theoretical capacity.[167] However, it always suffers from low electronic/ionic conductivity and large volume expansion, largely hindering its practical application. Wang et al.[167b] reported the construction of a 2D heterojunction composite electrode comprising ultrafine SnS_2 particles and TiO_2 NPs deposited on RGO nanosheets, which exhibited superior electrochemical lithium storage capability due to the synergetic effects of its respective components with rapid electron/ion transport, reduced particle aggregation/detachment, as well as boosted charge transfer at SnS_2/TiO_2 heterointerfaces driven by a built-in electric field. Wu et al.[167d] investigated polypyrrole-encapsulated SnS_2 nanosheets supported on defect-rich TiO_2 nanotubes as an anode material, and found that defect-rich TiO_2 provided more chemical adhesions to SnS_2 and discharge products, compared to defect-poor TiO_2, and then effectively stabilized the electrode structure, leading to an unprecedented good cycle stability.

6.5. Drawbacks of SnS_2/TiO_2

Only a few studies have reported the application of SnS_2 in PEC water splitting. The main bottlenecks are the serious charge recombination owing to the intrinsic low electrical conductivity, and sluggish surface oxygen evolution kinetics.

7. Other MS_x/TiO_2 Heterostructures

7.1. ZnS/TiO_2 Heterostructures

In contrast to the above narrow bandgap MS_x materials, ZnS is an important II–VI semiconductor with a wide bandgap, and is considered as a developing material star owing to good chemical and physical properties, including polar surfaces, a high optical transmittance toward visible light, good electron mobility, decent charge transport properties, and thermal stability.[168] It can also be associated to TiO_2 to increase the photocatalytic activity[169] because of its high potentials of conduction band e^- and valence band h^+ (–1.04 and +2.56 V vs NHE). Zhang et al.[5] prepared high-quality mesoporous ZnS@g-C_3N_4-TiO_2 nanospheres via a structure regulation strategy which exhibited

© 2019 WILEY-VCH Verlag GmbH & Co. KGaA, Weinheim

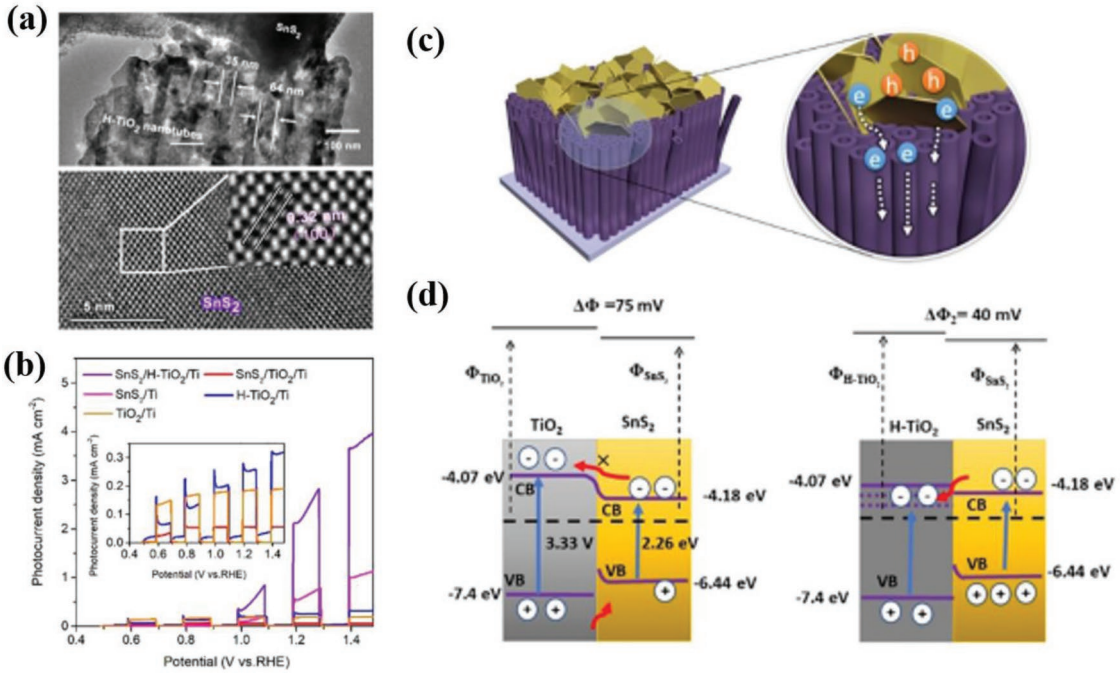

Figure 11. a) TEM images of SnS_2/H-TiO_2/Ti, and b) the Linear-sweep voltammograms of different electrodes under simulated 1 sun illumination. c) Illustration of the photogenerated charge transfer under visible-light irradiation and d) schematic energy-band diagram SnS_2/TiO_2 (left) and d) SnS_2/H-TiO_2 (right). Reproduced with permission.[166c] Copyright 2019, Wiley.

efficient photocatalytic H_2 production under visible-light irradiation due to the accelerated migration of photogenerated electrons from g-C_3N_4 to TiO_2 enabling by the introduction of ZnS.

Most reported studies based on ZnS/TiO_2 composites are focused on the applications in dye-sensitized solar cells[170] since the first report by Rao et al.[171] who fabricated a ZnS shell as a blocking layer on TiO_2 NPs in order to reduce the electron back-reaction, beneficial to enhance the electron injection and suppress the charge recombination. Deng et al.[170b] further incorporated ZnS inserting layer in TiO_2 inverse opal-based QDSCs and found that the "in-between" ZnS layer not only enhanced the light harvesting of QDs on its top but also lessened the charge-transfer resistances at the TiO_2/QD/electrolyte interfaces, leading to the enhanced cell efficiency.

7.2. Ag_2S/TiO_2 Heterostructures

As a direct and narrow bandgap semiconductor (≈0.92 eV), Ag_2S has gained intensive attention recently to be an ideal candidate for the photosensitization of TiO_2 owing to its high chemical stability, low toxicity, broad light absorption span (from UV to NIR region), and high absorption coefficient (≈10^4 m^{-1}). Usually, when the sizes of the Ag_2S QDs are close to its Bohr radius, the effective bandgap of the Ag_2S QDs increases and the corresponding absorption and fluorescence spectra are blueshifted to form a series of discrete energy levels (quantum size effect).[172] Ong et al.[173] fabricated Ag_2S NPs on TiO_2 hierarchical spheres demonstrating hydrogen production at 707.6 μmol h^{-1} g^{-1} and photodegradation of MO with pseudo-first order rate constant of 0.018 min^{-1}. Ghafoor et al.[174] used 1D TiO_2 nanofibers with more active sites and sensitized by ≈17 nm Ag_2S NPs (10 wt%) with the synergistic effect of enhanced Ti^{3+} chemical states and oxygen vacancies, which exhibited better simulated solar-light-driven photocatalytic activity by enhancing the rate constant to 0.030 min^{-1}. To utilize the full solar spectrum, Hu et al.[175] developed Ag_2S QDs/TiO_2 nanobelt heterostructures with UV–visible–NIR full spectrum photocatalytic property. Moreover, to inhibit the deterioration of Ag_2S, Liu et al.[176] introduced RGO nanosheets to effectively enhance the Ag_2S stability by suppressing the reduction of Ag^1 to Ag^0 (**Figure 12**a,b). Under NIR light illumination, only Ag_2S could be excited and generated electrons to transfer to the CB of TiO_2 and finally to the surface of RGO sheets. In this process, the electrons could absorb some surface molecules such as O_2 and convert to oxidative species (O^{2-}). Meanwhile, the photogenerated holes accumulated in the VB of Ag_2S would accelerate the decomposition of organic pollutants into nontoxic substance, rather than generating the stronger oxidative species (•OH), owing to the potential of •OH/H_2O (2.32 V vs NHE) is more positive than the VB of Ag_2S. In such a way, the photoinduced electrons and holes could be separated effectively, and thereby greatly enhancing photoactivity under NIR light irradiation.

Considering the energy level alignment, Ag-Ag_2S/TiO_2 nanohybrids have recently reported to exhibit tunable and enhanced photocatalytic and PEC properties. For instance, Yu et al.[177c] reported that the preparation of Ag-Ag_2S/TiO_2 by a two-step process including the simple photoinduced deposition of metallic Ag on the TiO_2 surface and the following in situ sulfidation of partial Ag into Ag_2S. The results indicated that Ag-Ag_2S/TiO_2 photocatalysts clearly exhibited a significantly higher UV-light photocatalytic H_2-evolution activity (119.11 μmol h^{-1})

© 2019 WILEY-VCH Verlag GmbH & Co. KGaA, Weinheim

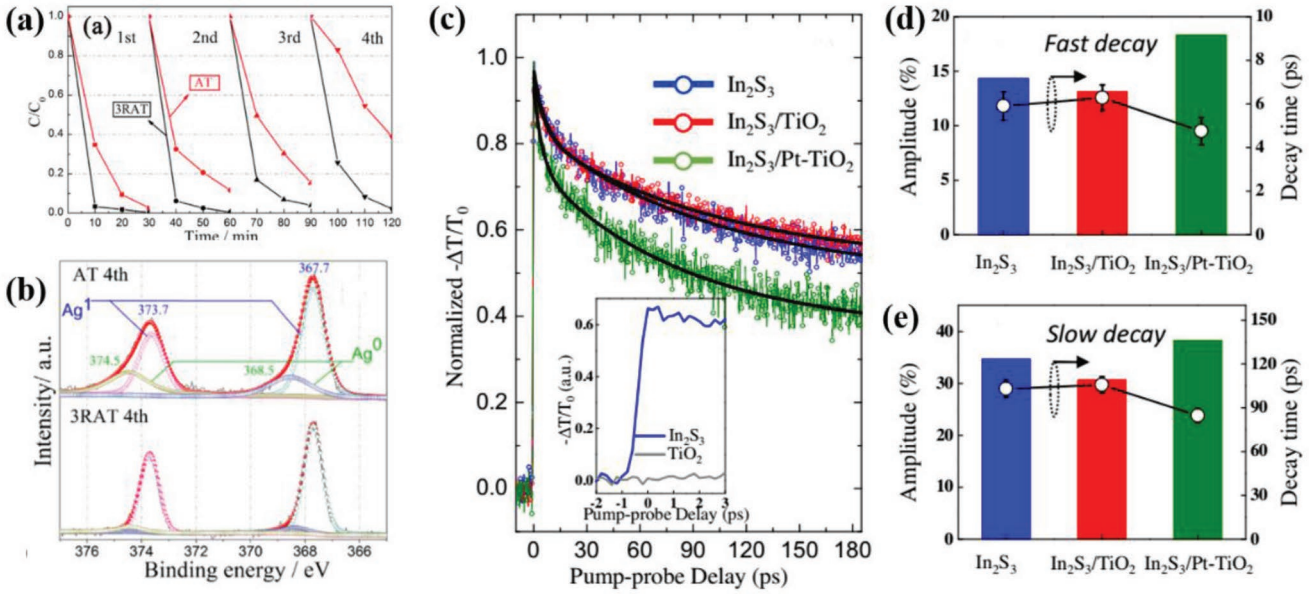

Figure 12. a) Repeated photocatalytic MO degradation under UV light irradiation (red line: AT nanoparticles; black line: 3RAT nanocomposite) and b) high-resolution XPS spectra of Ag 3d for AT and 3RAT nanocomposite after the fourth cycle experiments. Reproduced with permission.[176] Copyright 2017, Elsevier. c) Normalized THz photoconductivity signals for In_2S_3, In_2S_3/TiO_2, and In_2S_3/Pt-TiO_2 excited by a 400 nm pulse at room temperature, and the extracted amplitude (column) and decay times (circles) for the d) fast and e) slow decay components at a pump frequency of 500 μJ cm^{-2}. The inset shows the optical pump-terahertz (THz) probe (OPTP) signals. Reproduced with permission.[184b] Copyright 2016, Elsevier.

than TiO_2/Ag and TiO_2/Ag_2S photocatalysts by a factor of 3.9 and 3.6 times, respectively, which was due to the synergistic effect of dual electron-cocatalyst (metallic Ag and Ag_2S). The Ag-NP cocatalyst can steadily capture and transfer the photogenerated electrons from TiO_2 surface, while the Ag_2S cocatalyst acted as the interfacial active sites to promote the rapid H_2-evolution reaction.

Ag_2S/TiO_2 heterostructure is also explored for photoelectrochemical biosensing of proteins by incorporating a third material Bi_2S_3.[178] In addition, Ag_2S possesses good photoelectric and thermoelectric properties and it has been used in optoelectronic devices such as photovoltaic cells, infrared detectors, etc.[179]

7.3. Bi_2S_3/TiO_2 Heterostructures

Bismuth sulfide (Bi_2S_3) is a nontoxic and chemically stable semiconductor material with a narrow bandgap of ≈1.3–1.7 eV depending on the particle sizes. Its high absorption coefficient (10^4 cm^{-1}) in the visible light region and suitable energy band positions compatible with TiO_2 make it an ideal candidate to form Bi_2S_3/TiO_2 heterostructure for rapid electron transportation in solar photocatalytic degradation and water splitting.[180] Also, Bi_2S_3/TiO_2-based ternary composites are extensively explored in solar cells to further facilitate the carrier separation.[181]

7.4. In_2S_3/TiO_2 Heterostructures

Indium sulfide (In_2S_3) with a narrow bandgap of ≈2.0 eV respondent to visible light has been reported to be a promising visible light photocatalyst due to its high photosensitivity and photoconductivity, stable chemical and physical characteristics, and low toxicity.[182] The toxicity of In^{3+} ions is much lower than Cd^{2+}, making it a good candidate instead of toxic CdS, which endows less hazards of secondary pollution. In_2S_3 is known to crystallize in three polymorphic forms: α-In_2S_3 (defect cubic), β-In_2S_3 (defect spinel), and γ-In_2S_3 (layered structure). Of these, β-In_2S_3 has been widely investigated as an excellent sensitizer for TiO_2-based visible-light-driven photocatalysts.[183] Wang et al.[183c] developed a quasi-core-shell In_2S_3/anatase TiO_2@metallic $Ti_3C_2T_x$ hybrid consisting of well-designed type-II heterojunction and non-noble metal-based Schottky junction with favorable charge transfer channels, which originated from the synergistic effects among the visible-light absorption of In_2S_3, the upward band bending of TiO_2, and the favorable electrical conductivity of $Ti_3C_2T_x$. It exhibited superior photocatalytic performance toward pollutant degradation under visible light irradiation compared to In_2S_3/CNT, In_2S_3/RGO, In_2S_3/MoS_2, and In_2S_3/TiO_2 under the same conditions.

In addition, the In_2S_3/TiO_2 heterostructures are good candidates for HER applications[184] and solar cells.[185] Mumtaz et al.[184a] developed a bilayered nanostructured core–shell heterojunction V-TiO_2@β-In_2S_3 nanorod arrays and tested for their photocatalytic applications, which exhibited superior PEC performance: The photocurrent density of modified V-TiO_2@β-In_2S_3 was 1.42 mA cm^{-2} (AM 1.5 illumination, at 0.5 V vs Ag/AgCl), and was twofold that of TiO_2@β-In_2S_3 (0.78 mA cm^{-2}) and threefold that of pristine TiO_2. In addition, the presence of V^0 at the interface suppressed the photocorrosion. The increased photocatalytic activity and enhanced stability were initiated by the hole-quenching window and the

© 2019 WILEY-VCH Verlag GmbH & Co. KGaA, Weinheim

enhanced collection of electrons from the β-In_2S_3 to the V modified substrate as compared to TiO_2@β-In_2S_3 layered nanorod arrays. Wang et al.[184b] found that it was within 5 ps for the photoexcited electrons in the CB of In_2S_3 transferring to the CB of TiO_2 and subsequently into Pt NPs in the ternary composite In_2S_3/Pt-TiO_2 by using optical pump-terahertz probe spectroscopy (Figure 12c–e). Han et al.[185] developed In_2S_3 nanoflower films consisted of ultrathin nanoflakes with a thickness of 5 nm to be grown on the surface of TiO_2 nanorod arrays using polyethylene glycol as the morphology-directing agent and used in solar cells. The energy conversion efficiency of In_2S_3/TiO_2 photoelectrodes was enhanced three times (PCE of 1.82%) compared with that of bare TiO_2 counterpart.

7.5. Drawbacks of Other MS_x/TiO_2

The wide bandgaps of both ZnS and TiO_2 limit their light absorption harvesting within the UV range, which is the main drawback of ZnS/TiO_2 heterostructures in the PEC field. The strong tendency of Ag_2S NPs to agglomerate highly hinders the catalytic activity owing to the high surface energy. Donor-acceptor energetics of Bi_2S_3 QDs largely restricts power conversion efficiencies of QDSSCs.[173b] While the In^{3+} ions are somewhat toxic and have a harmful effect to the environment. In a word, despite the exciting progresses, photostability and catalytic performance of single metal sulfide photocatalysts are still far from satisfactory, mainly due to the easy photocorrosion, sluggish separation of e–h pairs, and low migration kinetics of charge carriers.

8. Conclusion and Perspective

The structure steering of MS_x/TiO_2 heterojunctions in photocatalytic degradation, heavy metal reduction, solar fuel production, and CO_2 conversion is mainly focused on the improved light harvesting ability and effective interfacial charge transfer as well as affordable active sites for surface chemical reactions. Many effective and promising strategies, such as defects engineering, morphology engineering, crystal facets tuning, electrical conductivity enhancement, crystal phase adjusting, the development of ternary composites and multicomponent metal sulfides, have been studied in the past few years. Except these interesting and meaningful methods mentioned before, other novel methods also exhibit great potential and can be considered to further improve the performance.

i) *Trapped structure*. Except the QDs structure, the trapped structure based on 2D nanosheets can also be used to further enhance the light harvesting ability. Compared with the intrinsic absorbance of narrow bandgap semiconductors, trapped structures can promote the internal reflection of light, achieving high light harvesting ability.
ii) *Photonic crystals*. Photonic crystals have been established as unique periodic structures to promote photon capture and control over light–matter interactions. Nanophotonic techniques are particularly promising for the purpose of light trapping, as they allow us to control the flow of light on the length scale of several 100 nm to a few micrometers that is required for thin film PEC devices. Thus, constructing photonic crystals from 0D and 1D nanostructure is also an effective method to further enhance the light harvesting ability.
iii) *Ternary composite*. To further increase the PEC performance of MS_x/TiO_2 heterostructure, the most commonly used strategy is to form a ternary composite by rationally designed band alignment engineering. Adding a secondary narrow bandgap semiconductor help further extend the absorption range to visible or even infrared light. The positive synergetic effect between the MS_x and a secondary material can help suppress charge recombination, facilitate interfacial charge transfer, and offer extra active sites.

For QDSCs, new types of QD sensitizers are still greatly needed with the characteristics of a suitable band edge position, wide absorption range, lower density of trap states, environmentally friendly nature, and low cost. Specifically, the construction of composite-structured I-III-VI group QDs through alloying or a core/shell strategy is a promising way.

iv) *Z-scheme structure*. Metal decoration could ameliorate the low conductivity of MS_x/TiO_2 heterojunction to boost the charge transfer efficiency. Under certain conditions, plasmonic metal nanostructures could act as electron transfer mediator in ternary composites by mimicking Z-scheme reactions in photosynthesis to enhance the interfacial charge transfer. Nanocarbon material is also an effective candidate to construct Z-scheme heterojunction.

Constructing metal sulfides/TiO_2 heterojunctions is a viable approach for wide photo/electrochemical applications including organic photodegradation, hydrogen fuel generation, CO_2 conversion, and QDSCs. Significant advances have been achieved in the material design and electrode construction in recent years. As a trend to develop green and low-cost catalysts, low-toxic and nontoxic metal sulfides are favored to sensitize TiO_2. Several heavy metal-free alternative materials like $CuInS_2$ or $AgGa_{1-x}In_xS_2$ have been proposed to replace Cd- or Pb-based QDs. Although the solar-to-fuel conversion efficiencies are still some way off commercialization, research on the related topics is expanding rapidly. This work will make up for the gap of efficient MS_x-metal oxide junction architectures with fast charge separation efficiency.

Acknowledgements

L.X.Z. and F.T. contributed equally to this work. The authors would like to acknowledge the support from the National Natural Science Foundation of China (Grant No. 51702287), the Natural Science Foundation of Ningbo (Grant No. 2017A610064), the Educational Commission of Zhejiang Province (Y201738057) and Science and Technology Commission of Shanghai Municipality (Grant Nos. 18520744600, 18520710800, and 17520742400).

Conflict of Interest

The authors declare no conflict of interest.

© 2019 WILEY-VCH Verlag GmbH & Co. KGaA, Weinheim

Keywords

CO_2 reduction, heterostructures, metal sulfides, photocatalysts, TiO_2, water splitting

Received: July 19, 2019
Revised: September 30, 2019
Published online: November 21, 2019

[1] A. Fujishima, K. Honda, *Nature* **1972**, *238*, 37.
[2] a) R. Asahi, T. Morikawa, T. Ohwaki, K. Aoki, Y. Taga, *Science* **2001**, *293*, 269; b) J. Bai, B. Zhou, *Chem. Rev.* **2014**, *114*, 10131; c) Y. Bai, I. Mora-Sero, F. De Angelis, J. Bisquert, P. Wang, *Chem. Rev.* **2014**, *114*, 10095; d) T. Rajh, N. M. Dimitrijevic, M. Bissonnette, T. Koritarov, V. Konda, *Chem. Rev.* **2014**, *114*, 10177; e) Y. Ma, X. Wang, Y. Jia, X. Chen, H. Han, C. Li, *Chem. Rev.* **2014**, *114*, 9987; f) W. X. Ouyang, F. Teng, X. S. Fang, *Adv. Funct. Mater.* **2018**, *28*, 1707178.
[3] a) D. J. Stacchiola, S. D. Senanayake, P. Liu, J. A. Rodriguez, *Chem. Rev.* **2013**, *113*, 4373; b) M. Dahl, Y. Liu, Y. Yin, *Chem. Rev.* **2014**, *114*, 9853; c) M. Wang, J. Ioccozia, L. Sun, C. Lin, Z. Lin, *Energy Environ. Sci.* **2014**, *7*, 2182; d) S. H. Shen, J. Chen, M. Wang, X. Sheng, X. Y. Chen, X. J. Feng, S. S. Mao, *Prog. Mater. Sci.* **2018**, *98*, 299; e) N. Gao, X. S. Fang, *Chem. Rev.* **2015**, *115*, 8294; f) Y. Yang, S. W. Niu, D. D. Han, T. Y. Liu, G. M. Wang, Y. Li, *Adv. Energy Mater.* **2017**, *7*, 1700555.
[4] a) J. Tian, Z. Zhao, A. Kumar, R. I. Boughton, H. Liu, *Chem. Soc. Rev.* **2014**, *43*, 6920; b) H. Li, Y. Wang, G. Chen, Y. Sang, H. Jiang, J. He, X. Li, H. Liu, *Nanoscale* **2016**, *8*, 6101; c) L. X. Zheng, K. Hu, F. Teng, X. S. Fang, *Small* **2017**, *13*, 1602448; d) W. X. Ouyang, F. Teng, J. H. He, X. S. Fang, *Adv. Funct. Mater.* **2019**, *29*, 1807672.
[5] C. Zhang, Y. Zhou, J. Bao, J. Fang, S. Zhao, Y. Zhang, X. Sheng, W. Chen, *Chem. Eng. J.* **2018**, *346*, 226.
[6] G. Hodes, *J. Mod. Opt.* **2008**, *112*, 191.
[7] a) Z. Pan, H. Rao, I. Mora-Sero, J. Bisquert, X. Zhong, *Chem. Soc. Rev.* **2018**, *47*, 7659; b) M. Kouhnavard, S. Ikeda, N. A. Ludin, N. B. Ahmad Khairudin, B. V. Ghaffari, M. A. Mat-Teridi, M. A. Ibrahim, S. Sepeai, K. Sopian, *Renewable Sustainable Energy Rev.* **2014**, *37*, 397.
[8] Y. J. Yuan, H. W. Lu, Z. T. Yu, Z. G. Zou, *ChemSusChem* **2015**, *8*, 4113.
[9] a) X. Huang, Z. Zeng, H. Zhang, *Chem. Soc. Rev.* **2013**, *42*, 1934; b) G. Zhang, H. Liu, J. Qu, J. Li, *Energy Environ. Sci.* **2016**, *9*, 1190; c) D. Kong, H. Wang, J. J. Cha, M. Pasta, K. J. Koski, J. Yao, Y. Cui, *Nano Lett.* **2013**, *13*, 1341.
[10] R. Coehoorn, C. Haas, R. A. de Groot, *Phys. Rev. B* **1987**, *35*, 6203.
[11] a) K. F. Mak, C. Lee, J. Hone, J. Shan, T. F. Heinz, *Phys. Rev. Lett.* **2010**, *105*, 136805; b) A. Splendiani, L. Sun, Y. B. Zhang, T. S. Li, J. Kim, C. Y. Chim, G. Galli, F. Wang, *Nano Lett.* **2010**, *10*, 1271.
[12] S. L. O. Eriksson, *Phys. Rev. B* **2009**, *79*, 5409.
[13] a) T. R. Thurston, J. P. Wilcoxon, *J. Phys. Chem. B* **1999**, *103*, 11; b) W. Ho, J. C. Yu, J. Lin, J. Yu, P. Li, *Langmuir* **2004**, *20*, 5865; c) L. Wang, C. Wang, W. Liu, Q. Chen, M. He, *Tetrahedron Lett.* **2016**, *57*, 1771; d) J. Tao, J. Chai, L. Guan, J. Pan, S. Wang, *Appl. Phys. Lett.* **2015**, *106*, 081602.
[14] A. Molina-Sánchez, D. Sangalli, K. Hummer, A. Marini, L. Wirtz, *Phys. Rev. B* **2013**, *88*, 2358.
[15] a) W. Zhou, Z. Yin, Y. Du, X. Huang, Z. Zeng, Z. Fan, H. Liu, J. Wang, H. Zhang, *Small* **2013**, *9*, 140; b) I. Tacchini, E. Terrado, A. Ansón, M. T. Martínez, *Micro Nano Lett.* **2011**, *6*, 932; c) D. Wang, Y. Xu, F. Sun, Q. Zhang, P. Wang, X. Wang, *Appl. Surf. Sci.* **2016**, *377*, 221.
[16] W. Zhang, X. Xiao, Y. Li, X. Zeng, L. Zheng, C. Wan, *RSC Adv.* **2016**, *6*, 33705.
[17] K. H. Hu, X. G. Hu, Y. F. Xu, J. D. Sun, *J. Mater. Sci.* **2010**, *45*, 2640.
[18] B. Pourabbas, B. Jamshidi, *Chem. Eng. J.* **2008**, *138*, 55.
[19] X. Chen, J. Zhang, X. Jiang, H. Wang, Z. Kong, J. Xi, Z. Ji, *Mater. Lett.* **2018**, *229*, 277.
[20] J. Wang, B. Wei, L. Xu, H. Gao, W. Sun, J. Che, *Mater. Lett.* **2016**, *179*, 42.
[21] L. Zeng, X. Li, S. Fan, Z. Yin, M. Zhang, J. Mu, M. Qin, T. Lian, M. Tadé, S. Liu, *Electrochim. Acta* **2019**, *295*, 810.
[22] X. Zhang, C. Shao, X. Li, F. Miao, K. Wang, N. Lu, Y. Liu, *J. Alloys Compd.* **2016**, *686*, 137.
[23] M. Kapilashrami, Y. Zhang, Y. S. Liu, A. Hagfeldt, J. Guo, *Chem. Rev.* **2014**, *114*, 9662.
[24] W. Teng, Y. Wang, H. Huang, X. Li, Y. Tang, *Appl. Surf. Sci.* **2017**, *425*, 507.
[25] S. C. Han, L. F. Hu, N. Gao, X. S. Fang, *Adv. Funct. Mater.* **2014**, *24*, 3725.
[26] W. Zhang, X. Xiao, Y. Li, X. Zeng, L. Zheng, C. Wan, *Appl. Surf. Sci.* **2016**, *389*, 496.
[27] N. Shao, J. Wang, D. Wang, P. Corvini, *Appl. Catal., B Environ.* **2017**, *203*, 964.
[28] a) S. A. Ansari, M. M. Khan, M. O. Ansari, M. H. Cho, *New J. Chem.* **2016**, *40*, 3000; b) R. Asahi, T. Morikawa, H. Irie, T. Ohwaki, *Chem. Rev.* **2014**, *114*, 9824.
[29] X. Tang, Z. Wang, W. Huang, Q. Jing, N. Liu, *Mater. Res. Bull.* **2018**, *105*, 126.
[30] X. Liu, Z. Xing, Y. Zhang, Z. Li, X. Wu, S. Tan, X. Yu, Q. Zhu, W. Zhou, *Appl. Catal., B Environ.* **2017**, *201*, 119.
[31] H. Fu, K. Yu, H. Li, J. Li, B. Guo, Y. Tan, C. Song, Z. Zhu, *Dalton Trans.* **2015**, *44*, 1664.
[32] a) S. Han, K. Liu, L. Hu, T. Feng, P. Yu, Y. Zhu, *Sci. Rep.* **2017**, *7*, 43599; b) S.-M. Paek, H. Jung, M. Park, J.-K. Lee, J.-H. Choy, *Chem. Mater.* **2005**, *17*, 3492; c) H. Liu, T. Lv, C. Zhu, X. Su, Z. Zhu, *J. Mol. Catal. A: Chem.* **2015**, *396*, 136.
[33] L. Zheng, S. Han, H. Liu, P. Yu, X. S. Fang, *Small* **2016**, *12*, 1527.
[34] Y. Yu, J. Wan, Z. Yang, Z. Hu, *J. Colloid Interface Sci.* **2017**, *502*, 100.
[35] W. Zhang, X. Xiao, L. Zheng, C. Wan, *Appl. Surf. Sci.* **2015**, *358*, 468.
[36] H. G. Yang, C. H. Sun, S. Z. Qiao, J. Zou, G. Liu, S. C. Smith, H. M. Cheng, G. Q. Lu, *Nature* **2008**, *453*, 638.
[37] J. Yu, G. Dai, Q. Xiang, M. Jaroniec, *J. Mater. Chem.* **2011**, *21*, 1049.
[38] L. Ye, J. Mao, J. Liu, Z. Jiang, T. Peng, L. Zan, *J. Mater. Chem. A* **2013**, *1*, 10532.
[39] L. Cao, R. Wang, D. Wang, L. Xu, X. Li, *Chem. Phys. Lett.* **2014**, *612*, 285.
[40] J. Zhang, L. Huang, Z. Lu, Z. Jin, X. Wang, G. Xu, E. Zhang, H. Wang, Z. Kong, J. Xi, Z. Ji, *J. Alloys Compd.* **2016**, *688*, 840.
[41] a) W. Gao, M. Wang, C. Ran, L. Li, *Chem. Commun.* **2015**, *51*, 1709; b) S. X. Liu, L. X. Zheng, P. P. Yu, S. C. Han, X. S. Fang, *Adv. Funct. Mater.* **2016**, *26*, 3331.
[42] W. Han, C. Zang, Z. Huang, H. Zhang, L. Ren, X. Qi, J. Zhong, *Int. J. Hydrogen Energy* **2014**, *39*, 19502.
[43] D. B. Nimbalkar, H.-H. Lo, P. V. R. K. Ramacharyulu, S.-C. Ke, *RSC Adv.* **2016**, *6*, 31661.
[44] S. Pei, H.-M. Cheng, *Carbon* **2012**, *50*, 3210.
[45] a) M. Murdoch, G. I. N. Waterhouse, M. A. Nadeem, J. B. Metson, M. A. Keane, R. F. Howe, J. Llorca, H. Idriss, *Nat. Chem.* **2011**, *3*, 489; b) J. Yu, J. Ran, *Energy Environ. Sci.* **2011**, *4*, 1364.
[46] a) C. Liu, L. Wang, Y. Tang, S. Luo, Y. Liu, S. Zhang, Y. Zeng, Y. Xu, *Appl. Catal., B Environ.* **2015**, *164*, 1; b) C. Meng, Z. Liu, T. Zhang, J. Zhai, *Green Chem.* **2015**, *17*, 2764; c) Y.-J. Yuan, Z.-J. Ye, H.-W. Lu, B. Hu, Y.-H. Li, D.-Q. Chen, J.-S. Zhong, Z.-T. Yu, Z.-G. Zou, *ACS*

 © 2019 WILEY-VCH Verlag GmbH & Co. KGaA, Weinheim

Catal. **2016**, *6*, 532; d) Y. Zhu, Q. Ling, Y. Liu, H. Wang, Y. Zhu, *Phys. Chem. Chem. Phys.* **2015**, *17*, 933.
[47] A. B. Laursen, S. Kegnæs, S. Dahl, I. Chorkendorff, *Energy Environ. Sci.* **2012**, *5*, 5577.
[48] a) K. Chang, Z. Mei, T. Wang, Q. Kang, S. Ouyang, J. Ye, *ACS Nano* **2014**, *8*, 7078; b) Y. Araki, K. Honna, H. Shimada, *J. Catal.* **2002**, *207*, 361.
[49] a) M. V. Bollinger, J. V. Lauritsen, K. W. Jacobsen, J. K. Norskov, S. Helveg, F. Besenbacher, *Phys. Rev. Lett.* **2001**, *87*, 196803; b) A. Bruix, H. G. Füchtbauer, A. K. Tuxen, A. S. Walton, M. Andersen, S. Porsgaard, F. Besenbacher, B. Hammer, J. V. Lauritsen, *ACS Nano* **2015**, *9*, 9322; c) Y. Aray, A. D. Barrios, *Phys. Chem. Chem. Phys.* **2018**, *20*, 20417.
[50] Q. Liu, Z. Pu, A. M. Asiri, A. H. Qusti, A. O. Al-Youbi, X. Sun, *J. Nanopart. Res.* **2013**, *15*, 2057.
[51] S. Kanda, T. Akita, M. Fujishima, H. Tada, *J. Colloid Interface Sci.* **2011**, *354*, 607.
[52] M. Shen, Z. Yan, L. Yang, P. Du, J. Zhang, B. Xiang, *Chem. Commun.* **2014**, *50*, 15447.
[53] a) K. K. Paul, N. Sreekanth, R. K. Biroju, A. J. Pattison, D. Escalera-López, A. Guha, T. N. Narayanan, N. V. Rees, W. Theis, P. K. Giri, *J. Mater. Chem. A* **2018**, *6*, 22681; b) Y. Dong, S. Y. Chen, Y. Lu, Y. X. Xiao, J. Hu, S. M. Wu, Z. Deng, G. Tian, G. G. Chang, J. Li, S. Lenaerts, C. Janiak, X. Y. Yang, B. L. Su, *Chem. - Asian J.* **2018**, *13*, 1609; c) X. Yang, H. Huang, M. Kubota, Z. He, N. Kobayashi, X. Zhou, B. Jin, J. Luo, *Mater. Res. Bull.* **2016**, *76*, 79.
[54] L. Zeng, X. Li, S. Fan, M. Zhang, Z. Yin, M. Tadé, S. Liu, *J. Power Sources* **2019**, *413*, 310.
[55] a) J. V. Lauritsen, J. Kibsgaard, S. Helveg, *Nat. Nanotechnol.* **2007**, *2*, 53; b) A. Y. Ana, L. Moshe, T. Reshef, P. B. Ronit, W. Marc, B. S. Maya, H. Lothar, A. N. Enyashin, S. Gotthard, F. Daniel, *Angew. Chem., Int. Ed.* **2015**, *123*, 1850.
[56] J. Xie, H. Zhang, S. Li, R. Wang, X. Sun, M. Zhou, J. Zhou, X. W. Lou, Y. Xie, *Adv. Mater.* **2013**, *25*, 5807.
[57] a) Z. Wu, B. Li, Y. Xue, J. Li, Y. Zhang, F. Gao, *J. Mater. Chem. A* **2015**, *3*, 19445; b) B. Chen, E. Liu, F. He, C. Shi, C. He, J. Li, N. Zhao, *Nano Energy* **2016**, *26*, 541; c) B. Chen, E. Liu, T. Cao, F. He, C. Shi, C. He, L. Ma, Q. Li, J. Li, N. Zhao, *Nano Energy* **2017**, *33*, 247; d) B. Chen, H. Lu, N. Zhao, C. Shi, E. Liu, C. He, L. Ma, *J. Power Sources* **2018**, *387*, 16.
[58] a) W. Zhou, H. Fu, *Inorg. Chem. Front.* **2018**, *5*, 1240; b) L. Guo, J. Deng, G. Wang, Y. Hao, K. Bi, X. Wang, Y. Yang, *Adv. Funct. Mater.* **2018**, *28*, 1804540.
[59] L. Guo, Z. Yang, K. Marcus, L. Zhao, B. Luo, Z. Le, X. Wang, Y. Du, Y. Yang, L. Guo, *Energy Environ. Sci.* **2017**, *11*, 106.
[60] a) L. Guo, C. Zhong, L. Shi, L. Ju, X. Wang, D. Yang, K. Bi, Y. Hao, Y. Yang, *Adv. Opt. Mater.* **2019**, *7*, 1801403; b) P. E. Evans, H. K. Jeong, Z. Hooshmand, D. Le, T. B. Rawal, S. N. Alvillar, L. Bartels, T. S. Rahman, P. A. Dowben, *J. Phys. Chem. C* **2018**, *122*, 10042.
[61] J. Xie, J. Zhang, S. Li, F. Grote, X. Zhang, H. Zhang, R. Wang, Y. Lei, B. Pan, Y. Xie, *J. Am. Chem. Soc.* **2013**, *135*, 17881.
[62] B. Zhao, L. L. Liu, G. D. Cheng, T. Li, N. Qi, Z. Q. Chen, Z. Tang, *Mater. Des.* **2017**, *113*, 1.
[63] L. P. L. Mawlong, K. K. Paul, P. K. Giri, *J. Phys. Chem. C* **2018**, *122*, 15017.
[64] a) L. Wang, X. Duan, G. Wang, C. Liu, S. Luo, S. Zhang, Y. Zeng, Y. Xu, Y. Liu, X. Duan, *Appl. Catal., B Environ.* **2016**, *186*, 88; b) J. Du, H. Wang, M. Yang, F. Zhang, H. Wu, X. Cheng, S. Yuan, B. Zhang, K. Li, Y. Wang, H. Lee, *Int. J. Hydrogen Energy* **2018**, *43*, 9307; c) Y. Li, Z. Yin, G. Ji, Z. Liang, Y. Xue, Y. Guo, J. Tian, X. Wang, H. Cui, *Appl. Catal., B Environ.* **2019**, *246*, 12.
[65] X.-Q. Gong, A. Selloni, *J. Phys. Chem. B* **2005**, *109*, 19560.
[66] Y. Sun, Q. Wu, G. Shi, *Energy Environ. Sci.* **2011**, *4*, 1113.
[67] Q. Xiang, J. Yu, M. Jaroniec, *J. Am. Chem. Soc.* **2012**, *134*, 6575.
[68] a) S. Li, T. Pu, J. Wang, X. Fang, Y. Liu, S. Kang, L. Cui, *Int. J. Hydrogen Energy* **2018**, *43*, 16534; b) J. Greeley, T. F. Jaramillo, J. Bonde, I. B. Chorkendorff, J. K. Nørskov, *Nat. Mater.* **2006**, *5*, 909.
[69] a) J. Tao, S. Chen, L. Guan, G. Chen, C. Yu, L. Chen, X. Cheng, H. Zhang, X. Xie, *Electrochim. Acta* **2018**, *283*, 419; b) T. Zhao, Z. Xing, Z. Xiu, Z. Li, P. Chen, Q. Zhu, W. Zhou, *J. Hazard. Mater.* **2019**, *364*, 117.
[70] C. Cheng, G. Liu, K. Du, G. Li, W. Zhang, S. Sanna, Y. Chen, N. Pryds, K. Wang, *Appl. Catal., B Environ.* **2018**, *237*, 416.
[71] Y. Pi, Z. Li, D. Xu, J. Liu, Y. Li, F. Zhang, G. Zhang, W. Peng, X. Fan, *ACS Sustainable Chem. Eng.* **2017**, *5*, 5175.
[72] a) Y. Liu, Y. Li, F. Peng, Y. Lin, S. Yang, S. Zhang, H. Wang, Y. Cao, H. Yu, *Appl. Catal., B Environ.* **2019**, *241*, 236; b) D. Voiry, H. Yamaguchi, J. Li, R. Silva, D. C. B. Alves, T. Fujita, M. Chen, T. Asefa, V. B. Shenoy, G. Eda, M. Chhowalla, *Nat. Mater.* **2013**, *12*, 850; c) D. Voiry, M. Salehi, R. Silva, T. Fujita, M. Chen, T. Asefa, V. B. Shenoy, G. Eda, M. Chhowalla, *Nano Lett.* **2013**, *13*, 6222; d) M. A. Lukowski, A. S. Daniel, F. Meng, A. Forticaux, L. Li, S. Jin, *J. Am. Chem. Soc.* **2013**, *135*, 10274; e) R. Raja, P. Sudhagar, A. Devadoss, C. Terashima, L. K. Shrestha, K. Nakata, R. Jayavel, K. Ariga, A. Fujishima, *Chem. Commun.* **2015**, *51*, 522.
[73] A. A. Sagade, R. Sharma, *Sensor Actuat. B Chem.* **2008**, *133*, 135.
[74] T. Inoue, A. Fujishima, S. Konishi, K. Honda, *Nature* **1979**, *277*, 637.
[75] a) P. Li, H. Hu, J. Xu, H. Jing, H. Peng, J. Lu, C. Wu, S. Ai, *Appl. Catal., B* **2014**, *147*, 912; b) H. Jung, K. M. Cho, K. H. Kim, H.-W. Yoo, A. Al-Saggaf, I. Gereige, H.-T. Jung, *ACS Sustainable Chem. Eng.* **2018**, *6*, 5718; c) F. Xu, B. Zhu, B. Cheng, J. Yu, J. Xu, *Adv. Opt. Mater.* **2018**, *6*, 1800911; d) L. Yu, Y. Xie, J. Zhou, Y. Li, Y. Yu, Z. Ren, *J. Mater. Chem. A* **2018**, *6*, 4706; e) W. Tu, Y. Li, L. Kuai, Y. Zhou, Q. Xu, H. Li, X. Wang, M. Xiao, Z. Zou, *Nanoscale* **2017**, *9*, 9065.
[76] S. C. Roy, O. K. Varghese, M. Paulose, C. A. Grimes, *ACS Nano* **2010**, *4*, 1259.
[77] M. Asadi, B. Kumar, A. Behranginia, B. A. Rosen, A. Baskin, N. Repnin, D. Pisasale, P. Phillips, W. Zhu, R. Haasch, *Nat. Commun.* **2014**, *5*, 4470.
[78] a) R. Dai, A. Zhang, Z. Pan, A. M. Al-Enizi, A. A. Elzatahry, L. Hu, G. Zheng, *Small* **2016**, *12*, 2792; b) H. Zhou, X. Xia, P. Lv, J. Zhang, X. Hou, M. Zhao, K. Ao, D. Wang, K. Lu, H. Qiao, M. Zimniewska, Q. Wei, *ChemSusChem* **2018**, *11*, 4060; c) B. Chen, Y. Meng, J. Sha, C. Zhong, W. Hu, N. Zhao, *Nanoscale* **2018**, *10*, 34.
[79] J. Zhou, M. Guo, L. Wang, Y. Ding, Z. Zhang, Y. Tang, C. Liu, S. Luo, *Chem. Eng. J.* **2019**, *366*, 163.
[80] Z. He, W. Que, Y. Xing, X. Liu, *J. Alloys Compd.* **2016**, *672*, 481.
[81] A. Kaur, A. Umar, W. A. Anderson, S. K. Kansal, *J. Photochem. Photobiol., A* **2018**, *360*, 34.
[82] Y. Xie, G. Ali, S. H. Yoo, S. O. Cho, *ACS Appl. Mater. Interfaces* **2010**, *2*, 2910.
[83] a) P. Zhou, Z. Le, Y. Xie, J. Fang, J. Xu, *J. Alloys Compd.* **2017**, *692*, 170; b) Y.-B. Du, L. Zhang, M. Ruan, C.-G. Niu, X.-J. Wen, C. Liang, X.-G. Zhang, G.-M. Zeng, *Mater. Chem. Phys.* **2018**, *212*, 69.
[84] a) H. Yang, Z. Liu, K. Wang, S. Pu, S. Yang, L. Yang, *Catal. Lett.* **2017**, *147*, 2581; b) A. D. Mani, C. Subrahmanyam, *Mater. Res. Bull.* **2016**, *73*, 377; c) Z. Hu, H. Quan, Z. Chen, Y. Shao, D. Li, *Photochem. Photobiol. Sci.* **2018**, *17*, 51.
[85] a) L. Wang, M. Wen, W. Wang, N. Momuinou, Z. Wang, S. Li, *J. Alloys Compd.* **2016**, *683*, 318; b) B. Pant, M. Park, H.-Y. Kim, S.-J. Park, *J. Alloys Compd.* **2017**, *699*, 73; c) H. Zangeneh, A. A. Zinatizadeh, S. Zinadini, M. Feyzi, E. Rafiee, D. W. Bahnemann, *J. Hazard. Mater.* **2019**, *369*, 384; d) U. A. Khan, J. Liu, J. Pan, H. Ma, S. Zuo, Y. Yu, A. Ahmad, S. Ullah, B. Li, *Ind. Eng. Chem. Res.* **2019**, *58*, 79.

© 2019 WILEY-VCH Verlag GmbH & Co. KGaA, Weinheim

[86] M. Sun, Y. Wang, Y. Fang, S. Sun, Z. Yu, *J. Alloys Compd.* **2016**, *684*, 335.
[87] a) L. Yu, D. Wang, D. Ye, *Sep. Purif. Technol.* **2015**, *156*, 708; b) X. Yang, Y. Wang, Z. Wang, X. Lv, H. Jia, J. Kong, M. Yu, *Ceram. Int.* **2016**, *42*, 7192; c) K. Xie, Q. Wu, Y. Wang, W. Guo, M. Wang, L. Sun, C. Lin, *Electrochem. Commun.* **2011**, *13*, 1469.
[88] F. Tian, D. Hou, F. Hu, K. Xie, X. Qiao, D. Li, *Appl. Surf. Sci.* **2017**, *391*, 295.
[89] a) J. Zhang, F.-X. Xiao, G. Xiao, B. Liu, *Appl. Catal., A* **2016**, *521*, 50; b) T. Zhao, Z. Xing, Z. Xiu, Z. Li, L. Shen, Y. Cao, M. Hu, S. Yang, W. Zhou, *Mater. Res. Bull.* **2018**, *103*, 114.
[90] J. Tao, Z. Gong, G. Yao, Y. Cheng, M. Zhang, J. Lv, S. Shi, G. He, X. Chen, Z. Sun, *Ceram. Int.* **2016**, *42*, 11716.
[91] D. Zhao, C.-F. Yang, *Renewable Sustainable Energy Rev.* **2016**, *54*, 1048.
[92] a) Y. Huang, J. Chen, W. Zou, L. Zhang, L. Hu, M. He, L. Gu, J. Deng, X. Xing, *Dalton Trans.* **2016**, *45*, 1160; b) J. Du, H. Wang, M. Yang, K. Li, L. Zhao, G. Zhao, S. Li, X. Gu, Y. Zhou, L. Wang, Y. Gao, W. Wang, D. J. Kang, *Electrochim. Acta* **2017**, *250*, 99; c) A. Meng, B. Zhu, B. Zhong, L. Zhang, B. Cheng, *Appl. Surf. Sci.* **2017**, *422*, 518; d) S. Han, Y.-C. Pu, L. Zheng, J. Z. Zhang, X. S. Fang, *J. Mater. Chem. A* **2015**, *3*, 22627; e) L. Liu, H. Hou, L. Wang, R. Xu, Y. Lei, S. Shen, D. Yang, W. Yang, *Nanoscale* **2017**, *9*, 15650; f) M. Guo, L. Wang, Y. Xia, W. Huang, Z. Li, *J. Alloys Compd.* **2016**, *684*, 616.
[93] a) H. Wang, Y. Bai, H. Zhang, Z. Zhang, J. Li, L. Guo, *J. Phys. Chem. C* **2010**, *114*, 16451; b) H. Zhang, D. Zhang, X. Qin, C. Cheng, *J. Phys. Chem. C* **2015**, *119*, 27875; c) J. R. Gonzalez-Moya, Y. Garcia-Basabe, M. L. Rocco, M. B. Pereira, J. L. Princival, L. C. Almeida, C. M. Araujo, D. G. David, A. F. da Silva, G. Machado, *Nanotechnology* **2016**, *27*, 285401.
[94] a) D. Ding, B. Zhou, S. Liu, G. Zhu, X. Meng, J. Yang, W. Fu, H. Yang, *RSC Adv.* **2017**, *7*, 36902; b) M. Krbal, J. Prikryl, R. Zazpe, H. Sopha, J. M. Macak, *Nanoscale* **2017**, *9*, 7755; c) C. Liu, Y. Yang, J. Li, S. Chen, *Nanotechnology* **2018**, *29*, 265401; d) P. S. Shinde, J. W. Park, M. A. Mahadik, J. Ryu, J. H. Park, Y.-J. Yi, J. S. Jang, *Int. J. Hydrogen Energy* **2016**, *41*, 21078; e) X. Zhang, M. Zeng, J. Zhang, A. Song, S. Lin, *RSC Adv.* **2016**, *6*, 8118; f) S. David, M. A. Mahadik, H. S. Chung, J. H. Ryu, J. S. Jang, *ACS Sustainable Chem. Eng.* **2017**, *5*, 7537.
[95] Y.-L. Chen, Y.-H. Chen, J.-W. Chen, F. Cao, L. Li, Z.-M. Luo, I.-C. Leu, Y.-C. Pu, *ACS Appl. Mater. Interfaces* **2019**, *11*, 8126.
[96] a) H. Zhao, M. Wu, J. Liu, Z. Deng, Y. Li, B.-L. Su, *Appl. Catal., B Environ.* **2016**, *184*, 182; b) J. Li, S. K. Cushing, P. Zheng, T. Senty, F. Meng, A. D. Bristow, A. Manivannan, N. Wu, *J. Am. Chem. Soc.* **2014**, *136*, 8438; c) H. Zhao, Z. Hu, J. Liu, Y. Li, M. Wu, G. Van Tendeloo, B.-L. Su, *Nano Energy* **2018**, *47*, 266; d) W. X. Ouyang, F. Teng, M. M. Jiang, X. S. Fang, *Small* **2017**, *13*, 1702177.
[97] a) V. M. Daskalaki, M. Antoniadou, G. L. Puma, D. I. Kondarides, P. Lianos, *Environ. Sci. Technol.* **2010**, *44*, 7200; b) J. S. Jang, S. H. Choi, H. G. Kim, J. S. Lee, *J. Phys. Chem. C* **2008**, *112*, 17200; c) H. Park, W. Choi, M. R. Hoffmann, *J. Mater. Chem.* **2008**, *18*, 2379; d) H. Park, Y. K. Kim, W. Choi, *J. Phys. Chem. C* **2011**, *115*, 6141.
[98] a) J. Low, B. Dai, T. Tong, C. Jiang, J. Yu, *Adv. Mater.* **2019**, *31*, 1802981; b) J. Zhang, D. Zhou, S. Dong, N. Ren, *J. Hazard. Mater.* **2019**, *366*, 311.
[99] a) H. Zhou, L. Ding, T. Fan, J. Ding, D. Zhang, Q. Guo, *Appl. Catal., B* **2014**, *147*, 221; b) L. Ding, H. Zhou, S. Lou, J. Ding, D. Zhang, H. Zhu, T. Fan, *Int. J. Hydrogen Energy* **2013**, *38*, 8244; c) H. Zhou, J. Pan, L. Ding, Y. Tang, J. Ding, Q. Guo, T. Fan, D. Zhang, *Int. J. Hydrogen Energy* **2014**, *39*, 16293.
[100] W. Zhao, J. Liu, Z. Deng, J. Zhang, Z. Ding, Y. Fang, *Int. J. Hydrogen Energy* **2018**, *43*, 18232.
[101] J. Wang, Z. Wang, P. Qu, Q. Xu, J. Zheng, S. Jia, J. Chen, Z. Zhu, *Int. J. Hydrogen Energy* **2018**, *43*, 7388.
[102] K. Ma, O. Yehezkeli, D. W. Domaille, H. H. Funke, J. N. Cha, *Angew. Chem., Int. Ed.* **2015**, *54*, 11490.
[103] a) Z. Wang, X. Li, C. K. Tan, C. Qian, A. C. Grimsdale, A. I. Y. Tok, *Appl. Surf. Sci.* **2019**, *470*, 800; b) C. Gao, Z. Zhang, X. Li, L. Chen, Y. Wang, Y. He, F. Teng, J. Zhou, W. Han, E. Xie, *Sol. Energy Mater. Sol. Cells* **2015**, *141*, 101; c) Q. Zhang, H. Xu, W. Yan, *Electrochim. Acta* **2012**, *61*, 64.
[104] L. Li, R. Chen, X. Zhu, Q. Liao, D. Ye, B. Zhang, X. He, L. Jiao, H. Feng, W. Zhang, *Renewable Energy* **2018**, *127*, 524.
[105] G. Zhao, M. Sun, X. Liu, J. Xuan, W. Kong, R. Zhang, Y. Sun, F. Jia, G. Yin, B. Liu, *Electrochim. Acta* **2019**, *304*, 334.
[106] a) Z. Ai, Y. Shao, B. Chang, B. Huang, Y. Wu, X. Hao, *Appl. Catal., B Environ.* **2019**, *242*, 202; b) N. Qin, J. Xiong, R. Liang, Y. Liu, S. Zhang, Y. Li, Z. Li, L. Wu, *Appl. Catal., B Environ.* **2017**, *202*, 374.
[107] N. Li, H. Huang, R. Bibi, Q. Shen, R. Ngulube, J. Zhou, M. Liu, *Appl. Surf. Sci.* **2019**, *476*, 378.
[108] L. Tang, Y. Deng, G. Zeng, W. Hu, J. Wang, Y. Zhou, J. Wang, J. Tang, W. Fang, *J. Alloys Compd.* **2016**, *662*, 516.
[109] a) T. Zhao, Z. Xing, Z. Xiu, Z. Li, S. Yang, Q. Zhu, W. Zhou, *Int. J. Hydrogen Energy* **2019**, *44*, 1586; b) Z. Jiang, K. Qian, C. Zhu, H. Sun, W. Wan, J. Xie, H. Li, P. K. Wong, S. Yuan, *Appl. Catal., B Environ.* **2017**, *210*, 194.
[110] K. Wu, P. Wu, J. Zhu, C. Liu, X. Dong, J. Wu, G. Meng, K. Xu, J. Hou, Z. Liu, X. Guo, *Chem. Eng. J.* **2019**, *360*, 221.
[111] a) N. D. Quang, T. T. Hien, N. D. Chinh, D. Kim, C. Kim, D. Kim, *Electrochim. Acta* **2019**, *295*, 710; b) J. Luo, L. Ma, T. He, C. F. Ng, S. Wang, H. Sun, H. J. Fan, *J. Phys. Chem. C* **2012**, *116*, 11956; c) Y.-L. Lee, C.-F. Chi, S.-Y. Liau, *Chem. Mater.* **2010**, *22*, 922.
[112] P. Pathak, L. H. Israel, E. J. Pereira, V. R. Subramanian, *ACS Appl. Mater. Interfaces* **2016**, *8*, 13400.
[113] L. Ma, X. Ai, X. Wu, *J. Alloys Compd.* **2017**, *691*, 399.
[114] S. Liu, Z. Luo, L. Li, H. Li, M. Chen, T. Wang, J. Gong, *Nano Energy* **2018**, *53*, 125.
[115] a) X. Li, H. Liu, D. Luo, J. Li, Y. Huang, H. Li, Y. Fang, Y. Xu, L. Zhu, *Chem. Eng. J.* **2012**, *180*, 151; b) Y. Wei, J. Jiao, Z. Zhao, J. Liu, J. Li, G. Jiang, Y. Wang, A. Duan, *Appl. Catal., B Environ.* **2015**, *179*, 422; c) R. Chen, X. Cheng, X. Zhu, Q. Liao, L. An, D. Ye, X. He, Z. Wang, *Chem. Eng. J.* **2017**, *316*, 911; d) M. Cheng, S. Yang, R. Chen, X. Zhu, Q. Liao, Y. Huang, *Mol. Catal.* **2018**, *448*, 185; e) F. Wang, J. Wang, *ECS J. Solid State Sci. Technol.* **2019**, *8*, Q1.
[116] a) A. Braga, S. Giménez, I. Concina, A. Vomiero, I. N. Mora-Seró, *J. Phys. Chem. Lett.* **2011**, *2*, 454; b) I. Hwang, M. Baek, K. Yong, *ACS Appl. Mater. Interfaces* **2015**, *7*, 27863; c) S. A. Pawar, D. S. Patil, H. R. Jung, J. Y. Park, S. S. Mali, C. K. Hong, J.-C. Shin, P. S. Patil, J.-H. Kim, *Electrochim. Acta* **2016**, *203*, 74; d) B. Zhang, J. Zheng, X. Li, Y. Fang, L. W. Wang, Y. Lin, F. Pan, *Chem. Commun.* **2016**, *52*, 5706.
[117] X. Chen, Z. Lan, S. Zhang, J. Wu, J. Zhang, *Opt. Commun.* **2017**, *395*, 111.
[118] W.-T. Sun, Y. Yu, H.-Y. Pan, X.-F. Gao, Q. Chen, L.-M. Peng, *J. Am. Chem. Soc.* **2008**, *130*, 1124.
[119] F. Ji, R. Zhou, H. Niu, L. Wan, H. Guo, X. Mao, W. Gan, J. Xu, *Ceram. Int.* **2016**, *42*, 12194.
[120] a) A. Dey, P. Karan, A. Sengupta, S. A. Moyez, P. Sarkar, S. B. Majumder, D. Pradhan, S. Roy, *Sol. Energy* **2017**, *158*, 83; b) Y.-S. Lee, C. V. V. M. Gopi, A. E. Reddy, C. Nagaraju, H.-J. Kim, *New J. Chem.* **2017**, *41*, 1914.
[121] a) J. Shan, P. Pulkkinen, U. Vainio, J. Maijala, J. Merta, H. Jiang, R. Serimaa, E. Kauppinen, H. Tenhu, *J. Mater. Chem.* **2008**, *18*, 3200; b) Z. Yixin, P. Hongcheng, L. Yongbing, Q. Xiaofeng, Z. Junjie, B. Clemens, *J. Am. Chem. Soc.* **2009**, *131*, 4253; c) C. Ratanatawanate, A. Bui, K. Vu, K. J. Balkus, Jr., *J. Phys. Chem. C* **2011**, *115*, 6175.

© 2019 WILEY-VCH Verlag GmbH & Co. KGaA, Weinheim

[122] a) Y. Wang, H. Li, Y. Zhang, Y. Peng, P. Zhang, J. Zhao, *Nano Res.* **2018**, *11*, 831; b) I. P. Liu, H. S. Teng, Y. L. Lee, *J. Mater. Chem. A* **2017**, *5*, 23146; c) L. Guo, Q. Sun, K. Marcus, Y. Hao, J. Deng, K. Bi, Y. Yang, *J. Mater. Chem. A* **2018**, *6*, 22005.
[123] a) Y. Y. Lu, Y. Y. Zhang, J. Zhang, Y. Shi, Z. Li, Z. C. Feng, C. Li, *Appl. Surf. Sci.* **2016**, *370*, 312; b) G. Hou, Z. Cheng, L. Kang, X. Xu, F. Zhang, H. Yang, *CrystEngComm* **2015**, *17*, 5496; c) S. Khanchandani, S. Kumar, A. K. Ganguli, *ACS Sustainable Chem. Eng.* **2016**, *4*, 1487; d) L. Gao, J. Du, T. Ma, *Ceram. Int.* **2017**, *43*, 9559.
[124] a) C. Ratanatawanate, Y. Tao, K. J. Balkus, Jr., *J. Phys. Chem. C* **2009**, *113*, 10755; b) C. Ratanatawanate, C. Xiong, K. J. Balkus, Jr., *ACS Nano* **2008**, *2*, 1682.
[125] L. Li, J. Ya, L. Xiang, Z. Liu, E. Lei, *Appl. Phys. A* **2017**, *123*.
[126] J. Ma, Q. Du, H. Ge, Q. Zhang, *J. Mater. Sci.* **2019**, *54*, 2928.
[127] a) M. Maleki, M. Haghighi, *J. Mol. Catal. A: Chem.* **2016**, *424*, 283; b) H. Y. He, *Microporous Mesoporous Mater.* **2016**, *227*, 31; c) C. Park, T. Ghosh, Z. Meng, U. Kefayat, N. Vikram, W. Oh, *Chin. J. Catal.* **2013**, *34*, 711.
[128] a) Q. Wang, N. An, Y. Bai, H. Hang, J. Li, X. Lu, Y. Liu, F. Wang, Z. Li, Z. Lei, *Int. J. Hydrogen Energy* **2013**, *38*, 10739; b) Y. Im, S. Kang, K. MinKim, T. Ju, G. B. Han, N.-K. Park, T. J. Lee, M. Kang, *Int. J. Photoenergy* **2013**, *203*; c) M. Chandra, K. Bhunia, D. Pradhan, *Inorg. Chem.* **2018**, *57*, 4524.
[129] Q. Wang, G. Yun, Y. Bai, N. An, Y. Chen, R. Wang, Z. Lei, W. Shangguan, *Int. J. Hydrogen Energy* **2014**, *39*, 13421.
[130] K. Manjunath, V. S. Souza, G. Nagaraju, J. M. L. Santos, J. Dupont, T. Ramakrishnappa, *New J. Chem.* **2016**, *40*, 10172.
[131] Y. Wang, L. Bai, Y. Wang, D. Qin, D. Shan, X. Lu, *Analyst* **2018**, *143*, 1699.
[132] a) Z. Lan, W. Wu, S. Zhang, L. Que, J. Wu, *Ceram. Int.* **2016**, *42*, 8058; b) X. Zhao, J. Huang, Y. Wang, C. Xiang, D. Sun, L. Wu, X. Tang, K. Sun, Z. Zang, L. Sun, *Electrochim. Acta* **2016**, *199*, 180.
[133] L. Quan, W. Li, L. Zhu, X. Chang, H. Liu, *RSC Adv.* **2014**, *4*, 32214.
[134] C. Ratanatawanate, C. Xiong, K. J. Balkus, *ACS Nano* **2008**, *2*, 1682.
[135] a) H. Su, Y. Xie, P. Gao, Y. Xiong, Y. Qian, *J. Mater. Chem.* **2001**, *11*, 684; b) O. Trejo, K. E. Roelofs, S. Xu, M. Logar, R. Sarangi, D. Nordlund, A. L. Dadlani, R. Kravec, N. P. Dasgupta, S. F. Bent, F. B. Prinz, *Nano Lett.* **2015**, *15*, 7829; c) Q. Dong, W. Liao, B. Wang, Z. Liu, *RSC Adv.* **2015**, *5*, 33869.
[136] S. Jiao, J. Wang, Q. Shen, Y. Li, X. Zhong, *J. Mater. Chem. A* **2016**, *4*, 7214.
[137] X. Zhang, Y. Lin, J. Wu, J. Jing, B. Fang, *Opt. Commun.* **2017**, *395*, 117.
[138] M. A. Basit, M. A. Abbas, E. S. Jung, J. H. Bang, T. J. Park, *Mater. Chem. Phys.* **2017**, *196*, 170.
[139] M. A. Basit, M. A. Abbas, E. S. Jung, Y. M. Park, J. H. Bang, T. J. Park, *Electrochim. Acta* **2016**, *211*, 644.
[140] M. A. K. L. Dissanayake, T. Jaseetharan, G. K. R. Senadeera, C. A. Thotawatthage, *Electrochim. Acta* **2018**, *269*, 172.
[141] W. Lee, I. Ryu, H. Lee, S. Yim, *Appl. Surf. Sci.* **2018**, *432*, 255.
[142] Z. Zhang, C. Shi, J. Chen, G. Xiao, L. Li, *Appl. Surf. Sci.* **2017**, *410*, 8.
[143] Z. Zhang, C. Shi, G. Xiao, K. Lv, C. Ma, J. Yue, *Ceram. Int.* **2017**, *43*, 10052.
[144] X. Zhang, B. Wang, Z. Liu, *J. Colloid Interface Sci.* **2016**, *484*, 213.
[145] K. Lv, C. Shi, Z. Zhang, C. Ma, Q. Wang, *Curr. Appl. Phys.* **2018**, *18*, 648.
[146] R. Zhou, Y. Huang, L. Wan, H. Niu, F. Ji, J. Xu, *J. Alloys Compd.* **2017**, *716*, 162.
[147] Z. Liu, B. Wang, J. Wu, Q. Dong, X. Zhang, H. Xu, *Electrochim. Acta* **2016**, *187*, 480.
[148] J.-Y. Kim, Y. J. Jang, J. Park, J. Kim, J. S. Kang, D. Y. Chung, Y.-E. Sung, C. Lee, J. S. Lee, M. J. Ko, *Appl. Catal., B Environ.* **2018**, *227*, 409.
[149] K. Du, G. Liu, X. Chen, K. Wang, *Electrochim. Acta* **2018**, *277*, 244.
[150] Z. Liu, X. Cao, B. Wang, M. Xia, S. Lin, Z. Guo, X. Zhang, S. Gao, *J. Power Sources* **2017**, *342*, 452.
[151] a) M. Riedel, J. Wersig, A. Ruff, W. Schuhmann, A. Zouni, F. Lisdat, *Angew. Chem., Int. Ed.* **2019**, *58*, 801; b) R. Trevisan, P. Rodenas, V. Gonzalez-Pedro, C. Sima, R. S. Sanchez, E. M. Barea, I. Mora-Sero, F. Fabregat-Santiago, S. Gimenez, *J. Phys. Chem. Lett.* **2013**, *4*, 141; c) K. K. Patra, B. D. Bhuskute, C. S. Gopinath, *Sci. Rep.* **2017**, *7*, 6515.
[152] a) Y. Liu, L. Wang, H. Wang, M. Xiong, T. Yang, G. S. Zakharova, *Sens. Actuators, B* **2016**, *236*, 529; b) Y. Luo, C. Dong, X. Li, Y. Tian, *J. Electroanal. Chem.* **2015**, *759*, 51.
[153] a) H. Xia, S. Wu, S. Zhang, *Chem. - Asian J.* **2017**, *12*, 2942; b) F. Mughal, M. Muhyuddin, M. Rashid, T. Ahmed, M. A. Akram, M. A. Basit, *Chem. Phys. Lett.* **2019**, *717*, 69.
[154] H. Zang, P. K. Routh, Q. Meng, M. Cotlet, *Nanoscale* **2017**, *9*, 14664.
[155] T. Jiang, G. A. Ozin, *J. Mater. Chem.* **1998**, *8*, 1099.
[156] D. L. Greenaway, R. Nitsche, *J. Phys. Chem. Solids* **1965**, *26*, 1445.
[157] J. Mu, H. Miao, E. Liu, L. Chen, J. Feng, T. Han, Y. Gao, J. Fan, X. Hu, *Ceram. Int.* **2017**, *43*, 4992.
[158] X.-L. Gou, J. Chen, P.-W. Shen, *Mater. Chem. Phys.* **2005**, *93*, 557.
[159] C. Yang, W. Wang, Z. Shan, F. Huang, *J. Solid State Chem.* **2009**, *182*, 807.
[160] a) Y. C. Zhang, J. Li, H. Y. Xu, *Appl. Catal., B Environ.* **2012**, *123-124*, 18; b) L. Deng, H. Liu, X. Gao, X. Su, Z. Zhu, *Ceram. Int.* **2016**, *42*, 3808; c) J. Wang, X. Li, X. Li, J. Zhu, H. Li, *Nanoscale* **2013**, *5*, 1876; d) J. Li, T. Wang, X. Du, *Sep. Purif. Technol.* **2012**, *101*, 11.
[161] J. Zhang, L. Zhang, Y. Shi, G. Xu, E. Zhang, H. Wang, Z. Kong, J. Xi, Z. Ji, *Appl. Surf. Sci.* **2017**, *420*, 839.
[162] G. Dai, H. Qin, H. Zhou, W. Wang, T. Luo, *Appl. Surf. Sci.* **2018**, *430*, 488.
[163] X. Yan, K. Ye, T. Zhang, C. Xue, D. Zhang, C. Ma, J. Wei, G. Yang, *New J. Chem.* **2017**, *41*, 8482.
[164] a) Z. Zhang, C. Shao, X. Li, Y. Sun, M. Zhang, J. Mu, P. Zhang, Z. Guo, Y. Liu, *Nanoscale* **2013**, *5*, 606; b) K. C. Christoforidis, A. Sengele, V. Keller, N. Keller, *ACS Appl. Mater. Interfaces* **2015**, *7*, 19324; c) Y. Wang, X. Yang, Z. Wang, X. Lv, H. Jia, J. Kong, M. Yu, *J. Photochem. Photobiol., A* **2016**, *325*, 55.
[165] W. Zhang, X. Xiao, X. Zeng, Y. Li, L. Zheng, C. Wan, *J. Alloys Compd.* **2016**, *685*, 774.
[166] a) M. Li, H. Liu, T. Lv, M. Ding, *J. Mater. Chem. A* **2018**, *6*, 3488; b) J. Mu, H. Miao, E. Liu, J. Feng, F. Teng, D. Zhang, Y. Kou, Y. Jin, J. Fan, X. Hu, *Nanoscale* **2018**, *10*, 11881; c) J. Lin, Y. Liu, Y. Liu, C. Huang, W. Liu, X. Mi, D. Fan, F. Fan, H. Lu, X. Chen, *ChemSusChem* **2019**, *12*, 961.
[167] a) X. Hu, Q. Peng, T. Zeng, B. Shang, X. Jiao, G. Xi, *Chem. Eng. J.* **2019**, *363*, 213; b) H.-E. Wang, X. Zhao, X. Li, Z. Wang, C. Liu, Z. Lu, W. Zhang, G. Cao, *J. Mater. Chem. A* **2017**, *5*, 25056; c) W. Ren, H. Zhang, C. Guan, C. Cheng, *Green Energy Environ.* **2018**, *3*, 42; d) L. Wu, J. Zheng, L. Wang, X. H. Xiong, Y. Y. Shao, G. Wang, J. H. Wang, S. K. Zhong, M. H. Wu, *Angew. Chem., Int. Ed.* **2019**, *58*, 811; e) X. C. Li, G. L. Guo, N. Qin, Z. Deng, Z. G. Lu, D. Shen, X. Zhao, Y. Li, B. L. Su, H. E. Wang, *Nanoscale* **2018**, *10*, 15505.
[168] a) X. S. Fang, L. M. Wu, L. F. Hu, *Adv. Mater.* **2011**, *23*, 585; b) X. Xu, S. Li, J. Chen, S. Cai, Z. Long, X. S. Fang, *Adv. Funct. Mater.* **2018**, *28*, 1802029.
[169] a) H. Labiadh, T. B. Chaabane, L. Balan, N. Becheik, S. Corbel, G. Medjahdi, R. Schneider, *Appl. Catal., B Environ.* **2014**, *144*, 29; b) K. S. Ranjith, T. Uyar, *ACS Sustainable Chem. Eng.* **2018**, *6*, 12980; c) X. S. Fang, T. Y. Zhai, U. K. Gautam, L. Li, L. M. Wu, Y. Bando, D. Golberg, *Prog. Mater. Sci.* **2011**, *56*, 175.
[170] a) H.-J. Kim, J.-H. Kim, I. K. Durga, D. Punnoose, N. Kundakarla, A. E. Reddy, S. S. Rao, *New J. Chem.* **2016**, *40*, 9176; b) F. Deng, X. Wan, X. Mei, R. Fan, X. Yan, L. Wan, D. Shi, Y. Xiong, *Opt. Commun.* **2016**, *371*, 150.

© 2019 WILEY-VCH Verlag GmbH & Co. KGaA, Weinheim

[171] S. S. Rao, D. Punnoose, C. V. Tulasivarma, C. H. P. Kumar, C. V. Gopi, S. K. Kim, H. J. Kim, *Dalton Trans.* **2015**, *44*, 2447.
[172] P. Borah, D. Siboh, P. K. Kalita, J. K. Sarma, N. M. Nath, *Phys. B* **2018**, *530*, 208.
[173] W. L. Ong, G. W. Ho, *Proc. Eng.* **2016**, *141*, 7.
[174] S. Ghafoor, S. Ata, N. Mahmood, S. N. Arshad, *Sci. Rep.* **2017**, *7*, 255.
[175] X. Hu, Y. Li, J. Tian, H. Yang, H. Cui, *J. Ind. Eng. Chem.* **2017**, *45*, 189.
[176] T. Liu, B. Liu, L. Yang, X. Ma, H. Li, S. Yin, T. Sato, T. Sekino, Y. Wang, *Appl. Catal., B Environ.* **2017**, *204*, 593.
[177] a) D. Zhang, G. Xu, F. Chen, *Appl. Surf. Sci.* **2015**, *351*, 962; b) S. Shuang, R. Lv, X. Cui, Z. Xie, J. Zheng, Z. Zhang, *RSC Adv.* **2018**, *8*, 5784; c) H. Yu, W. Liu, X. Wang, F. Wang, *Appl. Catal., B Environ.* **2018**, *225*, 415; d) Y. Zuo, J. Chen, H. Yang, M. Zhang, Y. Wang, G. He, Z. Sun, *J. Alloys Compd.* **2019**, *780*, 347.
[178] B. Wang, J. T. Cao, Y. X. Dong, F. R. Liu, X. L. Fu, S. W. Ren, S. H. Ma, Y. M. Liu, *Chem. Commun.* **2018**, *54*, 806.
[179] J. Xue, J. Liu, S. Mao, Y. Wang, W. Shen, W. Wang, L. Huang, H. Li, J. Tang, *Mater. Res. Bull.* **2018**, *106*, 113.
[180] a) S. Paul, S. Ghosh, D. Barman, S. K. De, *Appl. Catal., B Environ.* **2017**, *219*, 287; b) P. Mazierski, J. Nadolna, G. Nowaczyk, W. Lisowski, M. J. Winiarski, T. Klimczuk, M. P. Kobylański, S. Jurga, A. Zaleska-Medynska, *J. Phys. Chem. C* **2017**, *121*, 17215; c) S. Kumar, S. Sharma, S. Sood, A. Umar, S. K. Kansal, *Ceram. Int.* **2016**, *42*, 17551; d) J. Li, L. Jin, L. Fang, M. Zhang, Y. Wang, X. Jiang, J. Lv, G. He, Z. Sun, *Appl. Surf. Sci.* **2018**, *456*, 694.
[181] a) Q. Wang, Z. Liu, H. Feng, R. Jin, S. Zhang, S. Gao, *Ceram. Int.* **2019**, *45*, 3995; b) Y. Lu, J. Jia, C. Lu, J. Huang, X. Feng, *Mater. Lett.* **2019**, *243*, 176; c) W. Li, J. Yang, Q. Jiang, Y. Luo, Y. Hou, S. Zhou, Y. Xiao, L. Fu, Z. Zhou, *J. Power Sources* **2016**, *307*, 690.
[182] B. Chai, T. Peng, P. Zeng, J. Mao, *J. Mater. Chem.* **2011**, *21*, 14587.
[183] a) X. Zhang, X. Li, C. Shao, J. Li, M. Zhang, P. Zhang, K. Wang, N. Lu, Y. Liu, *J. Hazard. Mater.* **2013**, *260*, 892; b) H. Heng, Q. Gan, P. Meng, X. Liu, *J. Alloys Compd.* **2017**, *696*, 51; c) H. Wang, Y. Wu, T. Xiao, X. Yuan, G. Zeng, W. Tu, S. Wu, H. Y. Lee, Y. Z. Tan, J. W. Chew, *Appl. Catal., B Environ.* **2018**, *233*, 213.
[184] a) A. Mumtaz, N. M. Mohamed, M. Mazhar, M. A. Ehsan, M. S. M. Saheed, *ACS Appl. Mater. Interfaces* **2016**, *8*, 9037; b) F. Wang, Z. Jin, Y. Jiang, E. H. G. Backus, M. Bonn, S. N. Lou, D. Turchinovich, R. Amal, *Appl. Catal., B Environ.* **2016**, *198*, 25.
[185] M. Han, L. Yu, W. Chen, W. Wang, J. Jia, *Appl. Surf. Sci.* **2016**, *369*, 108.

© 2019 WILEY-VCH Verlag GmbH & Co. KGaA, Weinheim